Title
Kinetic and Thermodynamic Factors for Selective CO2 Reduction at a Metal Hydride

Author
Ceballos, Bianca Myriah

Publication Date
2019

UNIVERSITY OF CALIFORNIA,
IRVINE

Kinetic and Thermodynamic Factors for Selective CO_2 Reduction at a Metal Hydride

DISSERTATION

submitted in partial satisfaction of the requirements
for the degree of

DOCTOR OF PHILOSOPHY

in Chemistry

by

Bianca Myriah Ceballos

Dissertation Committee:
Associate Professor Jenny Y. Yang, Chair
Professor A.S. Borovik
Professor Alan F. Heyduk

2019

DEDICATION

Para Virginia & Angela.
mi abuelas.
quien soñaban con una vida mejor
un sol naciente

For Olivia & Martin.
my parents.
who lit a light of curiosity within me
a warm fire

For Justine.
my sister.
my hero.
a sunrise summit

For Erick.
my brother.
a bubbling brook overflowing

For Sean.
my youngest brother.
a bird's song

For Zach.
my cheerleader.
falling snow

For Rocky.
my warm hug.
an earthbound star

TABLE OF CONTENTS

LIST OF FIGURES

LIST OF TABLES

LIST OF SCHEMES

LIST OF CHARTS

ACKNOWLEDGMENTS

Graduate school has taught me so many lessons that I will carry with me as I leave. I have so many people to thank for being a part of this process of learning and growth.

I am very grateful for my PI Professor Jenny Y. Yang. Thank you for making me feel limitless in my potential. You were always willing to help me reach for the next thing I had my eye on even when chances of success seemed slim. I will always be grateful for the guidance and support you shared with me during my time in your group. Few people have inspired me in the way that you have. Thank you for allowing me to learn and grow in your group.

Thank you to my committee members Professor Andy S. Borovik and Professor Alan F. Heyduk. Thank you for taking the time to answer my questions and for all of our helpful discussions. You have challenged me to grow and I am very happy to have received your guidance and support.

Thank you to my group members. I feel lucky to have met such wonderful people that I call my colleagues and friends. Thank you to past members Dr. Charlene Tsay, Dr. Juliet Khosrowabadi, Dr. Annie Chantarojsiri, Dr. Zach Thammavongsy, Dr. Brian Lydon, Dr. Alex H. Reath and present members Future Dr. Caitlin Hanna, Dr. Nadia Leonard, Drew Cunningham, Jeff Barlow, Sarah Wang, Tyler Kerr, Allie Zito, Ian Mercer, and all of the undergrads. You all made grad school a little easier and it was a pleasure to come to work every morning to learn and laugh with you all.

I would especially like to thank my lab ladies Charlene, Juliet, Annie and Caitlin. I will always be so grateful to have met such amazing women in graduate school. I could not have gotten through this without the perspective, guidance, and friendship that you each shared with me. Thank you for everything.

Thank you to my dearest friends Hanna and Nicole. We have grown so much together and I am happy to have had your love and support through this journey. Your friendship has been a gift that I treasure.

Thank you to Diana. Always ready to meet for a meal and pull me out of my grad school bubble. I am grateful for your love and support.

To my grad school friends Kelsey, Kellen, Megan, Kyle, Ace and many more thank you for all of the late night study sessions, the meals that we shared, and all of the memories that we made together. You have made this experience so much fun and I am grateful for the time that we spent together.

Thank you to my parents Olivia and Martin. I am grateful for all of the sacrifices that you made for me and my siblings. I may never be able to give you back what you gave to me. Just know that I appreciate everything that you have done for me. I am so grateful to have received your love and support throughout my life.

To my siblings Justine, Erick, and Sean thank you for all of the laughs, fun, and comfort over the years. It's been a blast to grow up and learn from you. Thank you for building me up when I needed it and for keeping me grounded always.

Thank you Zach for constantly reminding me that there are more important things in life then graduate school. I am grateful for all of the adventures that we have shared together and I look forward to the new ones ahead.

Special thanks to Rocky. You are the best buddy. Thank you for waking me up with a smile and making sure I appreciate the outdoors. I will always be grateful for your magic.

CURRICULUM VITAE

Bianca M. Ceballos

Education

University of California Irvine, Irvine, CA 2014 – 2019
Ph.D. in Chemistry: Expected Fall 2019

University of California Santa Barbara, Santa Barbara, CA 2009 – 2013
B.S. in Chemistry: June 2013

Awards

2019	International Solar Fuels Conference; *Best Poster Award*
2019	University of California Irvine; *School of Physical Sciences Faculty Endowed Fellowship*
2018	National Science Foundation; *Graduate Research Opportunities Worldwide*
2018	University of California Irvine; *School of Physical Sciences Latino Excellence Leadership Award*
2017	University of California Irvine; *Associated Graduate Student Travel Grant*
2015	National Science Foundation; *Graduate Research Fellowship Program*
2014	University of California Irvine; *Graduate Opportunity Fellowship*
2014	University of California Irvine; *Chemistry at the Space Time Limit Diversity Fellowship*

Publications

1. Bianca M. Ceballos and Jenny Yang, Highly Selective CO_2 Reduction by $[Pt(dmpe)_2]^{2+}$ through Kinetic and Thermodynamic Control, *Organometallics, 2019, accepted.*

2. Bianca M. Ceballos and Jenny Yang, Directing the Reactivity of Metal Hydrides for Selective CO_2 Reduction, *Proc Natl Acad Sci USA,* **2018**, *115* (50), 12686 - 12691.

3. Charlene Tsay, Bianca M. Ceballos, and Jenny Y. Yang, pH-Dependent Reactivity of a Water-Soluble Nickel Complex: Hydrogen Evolution vs. Selective electrochemical Hydride Generation, *Organometallics*, **2018**, *38* (6), 1286 - 1291.

4. Bianca M. Ceballos, Charlene Tsay, and Jenny Y. Yang, CO_2 reduction or HCO_2^- oxidation? Solvent-dependent thermochemistry of a nickel hydride complex, *Chem. Commun.*, **2017**, *53*, 7405 - 7408.

Research Experience

University of California Irvine, *Graduate Researcher*
Irvine, CA 2014 – 2019
Electrochemical Catalysis, Mechanistic Studies, Electrochemical Kinetics, and Chemical Synthesis
Research Project: Thermodynamic and Mechanistic Investigation of Transition metal Catalysts for Selective Catalytic Reduction of CO_2 in Water and Organic solvents
Advisor: Dr. Jenny Y. Yang, *Department of Chemistry*
Techniques: electrochemical kinetics, cyclic voltammetry, controlled potential electrolysis, IR-spectroelectrochemistry, NMR, UV-Vis, and inorganic synthesis

Paris Diderot University, *Visiting Graduate Researcher*
Paris, France 01/2019 – 03/2019
Electrochemical Catalysis and Mechanistic Studies
Research Project: The effect of Al(+3) on CO_2 reduction activity and mechanism with Fe porphyrin complexes

Advisor: Dr. Marc Robert, *Laboratory of Molecular Electrochemistry*
Techniques: cyclic voltammetry, controlled potential electrolysis

University of California Santa Barbara, *Post Undergraduate Researcher*
Santa Barbara, CA 7/2013 – 9/2013
Synthesis and Surface Modification
Research Project: Investigation of a Biocompatible Microfluidic System Polymer and Alkylsilane Molecules Surface Modification of Glass Microchannels for the Detection and Separation of Proteins
Advisor: Dr. Sumita Pennathur, *Department of Mechanical Engineering*
Techniques: organic synthesis, surface modification, contact angle, NMR spectroscopy

Related Professional Experience

University of California Irvine, *Associated Graduate Student Council Representative*, Irvine, CA
Physical Science Representative 2017 – 2018
Attend graduate student council meetings and vote on initiatives that affect graduate student economic issues (i.e. housing costs), professional development opportunities, and wellness.

University of California Irvine, *Science Policy Group*, Irvine, CA
Legislative Director 2017 – 2018
Lead group efforts to understand the effects of proposed legislation related to general science funding energy technology, or environment.

University of California Irvine, *Iota Sigma Pi Women in Chemistry Honors Society*, Irvine, CA
Co-Vice President 2015 – 2017
Organize outreach opportunities, professional development events, and seminars to help women in the chemistry interact with the community and encourage women to develop crucial professional skills necessary for pursuing career interests in academia and beyond.

University of California Irvine, *Iota Sigma Pi Women in Chemistry Honors Society*, Irvine, CA
Co-Outreach Coordinator 2014 – 2015
Organize outreach events in the graduate Chemistry Division including charity drives, volunteer program with Boys & Girls Club after school Science Program, and ACS National Chemistry week.

University of California Irvine, *Graduate Teaching Assistant*, Irvine, CA 2014, 2015, 2018, 2019
General Chemistry Discussion (Chem 1A, Chem 1LC, Chem 1LD)
Inorganic Chemistry Laboratory (Chem 107L)
Inorganic Chemistry Discussion (Chem 107)

Professional Development

University of California Irvine, Activate to Captivate, Irvine, CA
Participant 2018
Activate to Captivate is an 8 week communication certificate program for graduate students and Post Docs. Students learn important tools for effective public speaking and presentation strategies to engage different types of audiences.

University of California Irvine, Round Table: Letting Evidence Lead the Way, Irvine, CA
Organizer 2017
The UC Irvine Science Policy Group was awarded a small grant by the Union of Concerned Scientists that sponsored our roundtable discussion on evidence-based policy making. We invited scientists, local policy makers, and the community to join our event where we discussed renewable energy, climate change, innovation in STEM education, and public health. We aimed to connect scientists and policy makers to community members and foster discussion on important science topics.

University of California Irvine, COACH Career Building Workshop: Effective Negotiation, Irvine, CA
Organizer/Participant 2017

The COACH workshop offered sessions for graduate students and post docs as well as faculty sponsored by funds that we raised within Iota Sigma Pi (ISP) Women in Chemistry Honors Society in addition to donations from faculty and UC Irvine departments. We aimed to offer a professional development session geared toward issues that predominately face women, but that was inclusive to our department in physical sciences.

University of California Irvine, Science Communication Skills (Phy Sci 220), Irvine, CA
Participant 2017
A 10-week course for graduate students and Post Docs that focuses on developing writing and public speaking skills for clear and concise communication of science topics to a general audience. Students develop an elevator pitch and prepare a TED-style talk about their research.

Mentorship & Outreach

University of California Irvine, Graduate Division Summer Research Program Mentor, Irvine, CA
Graduate Student Mentor 2018
Mentored four undergraduate female research students visiting from different schools across the country and assisted students in preparing graduate student applications. We engaged in peer editing sessions and discussed their backgrounds, ongoing studies, and current research.

University of California Irvine, Project Scientist Academy Camp for girls, Irvine, CA
Graduate Student Speaker 2017
Project Scientist Academy Camp is a STEM camp for young girls ages 4-12. As a part of Iota Sigma Pi (ISP) Women in Chemistry Honors Society, we were invited to speak to the campers about our research and teach a science topic of our choice using a demonstration.

University of California Irvine, ACS National Chemistry Week at the Zoo, Santa Ana, CA
Organizer & Volunteer 2015 – 2017
Iota Sigma Pi (ISP) Women in Chemistry Honors Society participates in annual ACS National Chemistry week event at the Santa Zoo. Where each year we prepare a chemistry demonstration for families visiting the zoo that aims to be fun, interactive, educational, and stimulate interest in chemistry.

University of California Irvine, Laboratory Experiments and Activities in the Physical Sciences (LEAPS), Irvine, CA
Volunteer 2015 – 2018
LEAPS is an outreach program organized by UC Irvine Physical Sciences Department in which middle school students from underserved schools in nearby communities are given the opportunity to come to a large university to participate in science demonstration with the hopes of inspiring students to pursue a higher level education especially in the STEM fields.

University of California Irvine, Know-How Sessions: Why Graduate School?, Irvine, CA
Graduate Student Speaker 2014
The session was a part of a 5 part series sponsored by UC Irvine Graduate Division and aimed to prepare first-generation UC Irvine undergraduate students from underrepresented groups to successfully apply to graduate programs. I participated on a graduate student panel that included fellow first-generation graduate school students from different fields to speak about our graduate experience, why we chose to go to graduate school, and the challenges that we have faced.

University of California Irvine, National Science Foundation (NSF) Writing Workshop, Irvine, CA
Graduate Student Peer Editor 2015, 2016
Participated in peer editing sessions of NSF application materials for first and second year graduate students applying for the NSF Graduate Research Program Fellowship.

University of California Irvine, Boys & Girls Club After School Science Program, Santa Ana, CA
Volunteer 2015, 2016
The after school science program is organized by the Center for Chemistry at the Space-Time Limit (CaSTL), an NSF funded organization that depends on volunteers to help teach science concepts to

underprivileged youth in low income and primarily minority community of Santa Ana. We use interactive demonstrations, games, and discussion to stimulate interest in STEM topics.

University of California Irvine, Casa Teresa Women Shelter Holiday Gift Drive, Orange, CA
Organizer 2015
Casa Teresa is a non-profit women's shelter that offers temporary housing and support for pregnant women who are often alone. As a part of Iota Sigma Pi (ISP) Women in Chemistry Honors Society, we chose this organization for our department holiday gift drive where we donated items including toys, books, and diapers during the holiday season.

University of California Santa Barbara, Global Water Brigade, Santa Barbara, CA
Volunteer 2012 – 2013
Worked with Honduran community leaders, engineers, technicians and volunteers to implement a clean water filtration system for the rural community. Prepared and lead a presentation, in Spanish, highlighting sanitation rules to promote public health initiatives and clean water management for healthy living to community adults and children.

University of California Santa Barbara, Hospice Patient Care, Santa Barbara, CA
Volunteer 2012 – 2013
Participated in the Raggedy Ann and Andy Patient Care program for hospice care patients for 4 hours once a week for 6 months. Trained to use the Therapeutic Listening Care method of communication and basic tools necessary to work in a health care setting.

University of California Santa Barbara, Chemistry Outreach Leader, Santa Barbara, CA
Volunteer 2012 – 2013
Worked as a part of a team to communicate basic chemistry principles and topics to elementary students using fun and interactive demonstrations in a teaching laboratory.

Presentations

1. "Investigating Kinetic and Thermodynamic Factors for Selective CO_2 Reduction at a Metal Hydride", *International Solar Fuels Conference*; Hiroshima, Japan, November 2019, Poster

2. "Targeted Design of Molecular Electrocatalysts for Aqueous Hydrogen Evolution, Selective CO_2 Reduction, and Water Oxidation", *National Academy of Sciences - A.M. Sackler Colloquia: Status and Challenges in Science for Decarbonizing our Energy Landscape*, October 2018, Poster

3. "Over the Hill: Thermochemical exploration of Selective Hydride Transfer Using Metal Hydricity Activity Descriptors for H^+ and CO_2 Reduction Catalysis", *Gordon Research Seminar: Solar Fuels*, Ventura, CA, January 2018, Talk and Poster

4. "Over the Hill: Thermochemical exploration of Selective Hydride Transfer Using Metal Hydricity Activity Descriptors for H^+ and CO_2 Reduction Catalysis", *Inorganic Chemistry Student Seminar*, University of California Irvine , CA, January 2018, Talk

5. "A thermochemical exploration of Selective Hydride Transfer Using Metal Hydricity Activity Descriptors for H^+ and CO_2 Reduction Catalysis", *Southern California Bioinorganic Conference*, University of California Irvine, CA, December 2018, Flash talk and poster

6. "Tailoring Hydrogen Evolution Reaction (HER) Catalysts for Operation at Specific pH Values", *Department of Energy 2017 Annual Merit Review and Peer Evaluation Meeting for the Hydrogen and Fuel Cells Program and the Vehicle Technologies Office*, Washington D.C., June 2017, Talk and Poster

7. “Garbage to Gas: A New Look at Sustainable Chemistry”, *Brews and Brains: Science Communication Symposium*, University of California Irvine, CA, March 2017, Talk

7. “Thermodynamic Studies and pH Dependence of a Water Stable Nickel Hydride Complex”, *Southern California Organometallic Conference*, University of California Los Angeles, CA, December 2016, Talk

8. “Solvent Effects: Changes in Thermodynamic Driving Force of a $[Ni(diphosphine)_2]^{2+}$ for CO_2 Reduction”, *Southern California Organometallic Conference*, University of California Irvine, CA, April 2016, Poster

9. “Thermodynamic and Electrochemical Studies of a $[Ni(diphosphine)_2]^{2+}$ Complex in Water and Organic Solvents”, *American Chemical Society National Meeting and Exposition*, San Diego, CA, March 2016, Talk

10. “Thermodynamic and Electrochemical Studies of a $[Ni(diphosphine)_2]^{2+}$ Complex in Water and Organic Solvents”, *Southern California Organometallic Conference*, University of California Riverside, CA, December 2015, Poster

11. “Thermodynamic and Electrochemical Studies of a $[Ni(diphosphine)_2]^{2+}$ Complex in Water and Organic Solvents”, *American Chemical Society Western Regional Meeting*, California State University San Marcos, CA, November 2015, Poster

12. “Synthesis of Conjugated Oligoelectrolytes and Surface Modification for Nanofluidic Technologies”, *Summer Undergraduate Research Symposium*, University of California Santa Barbara, CA, June 2013, Poster

ABSTRACT OF THE DISSERTATION

Kinetic and Thermodynamic Factors for Selective CO_2 Reduction at a Metal Hydride

By

Bianca Myraih Ceballos

Doctor of Philosophy in Chemistry

University of California, Irvine, 2019

Associate Professor Jenny Y. Yang, Chair

The investigation of energy-storage strategies for renewable technologies is one of the most important modern-day challenges facing the future energy landscape. Inspired by the process of photosynthesis, where light energy is stored in the energy dense bonds of sugars, this work investigates the fundamental thermodynamic and kinetic forces directing the reactivity of homogenous catalysts for the electrochemical reduction of protons to H_2 or CO_2 to formate.

The selective catalytic reduction of CO_2 to formate is of interest because it is a carbon neutral process for storing energy in chemical bonds. Currently, CO_2 reduction pathways to target fuels are often limited by the off-cycle hydrogen evolution reaction (HER) which lowers faradaic efficiency and product selectivity. A catalyst design strategy is described which utilizes thermodynamic properties and hydricity-pK_a relationships to target reaction conditions for selective hydride transfer to specific substrates like protons or CO_2 in both water and organic solvents.

A detailed study of the electrocatalytic activity and selectivity of Ni and Pt diphosphine complexes for H_2 evolution and CO_2 reduction in water or the presence of acid in organic solvent is described. Experimental evidence demonstrates that the competing H_2 evolution pathway can

be disfavored with changes in proton activity. These results demonstrates that metal hydricity can be a quantitative activity descriptor for optimizing catalyst conditions for selective CO_2 reduction.

An investigation of the role of kinetic and thermodynamic factors that direct reactivity of a Pt diphosphine catalyst with protons or CO_2 to achieve high selectivity for formate is also described. An energy landscape plot was constructed from experimental studies comparing observed rates for electron transfer, protonation, and CO_2 binding. Our findings indicate that overall catalysis is limited by the rate of C-H bond formation by the reactive metal hydride. This information guides future compound modifications to improve catalytic activity.

The completed work gives new fundamental insights into a thermodynamic and kinetic based methodology for homogeneous catalyst design.

Introduction

Metal Hydricity as a Catalyst Activity Descriptor for Fuel Forming Reactions

0.1 Energy Storage in Chemical Bonds

One challenge facing the widespread use of renewable technologies is the question of energy storage: how can we store the electrical energy produced by renewable resources?

Batteries are one solution, where electrical energy is stored as chemical energy within an electrochemical cell. The energy storage potential of a battery is limited by the specific energy (energy per unit weight) and energy density (energy per unit volume) defined by the anode-cathode materials.[1-2] Despite recent leaps in Li-ion battery technology, the restraints set by energy density by mass and volume (100-200 Wh kg^{-1}) as well as energy cycling efficiencies constrain applications of this technology to portable electronics or electric vehicles that require multiple charging cycles to travel long distances.[3]

In contrast, the energy density of chemical fuels like gasoline (13,000 Wh kg^{-1}) or H_2 (33,000-39,000 Wh kg^{-1}) far exceed those of state of the art Li–ion battery technology (Figure 0.1)[3-4] As a result, energy storage in the form of chemical fuels is better suited for long-range

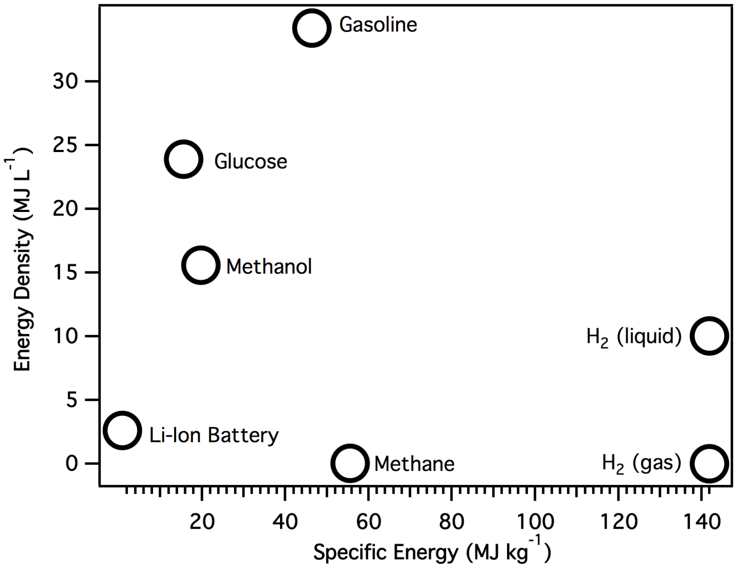

Figure 0.1 Plot of energy density by mass and volume for Li-ion batteries and chemical fuels.

applications like powering airplanes. Our current energy economy is centered on the use of liquid fossil fuels due in part to their high energy density and ease of transport. However, the use of fossil fuels produce harmful greenhouse gases like CO_2 that are intensifying the effects of global climate change.[5-6] Thus, there is an urgency to investigate alternative fuel sources to reduce the dependency on fossil fuels, while capitalizing on the advantages of high energy density chemical fuels.[7-11]

Carbon neutral energy storage strategies that rely on the conversion of CO_2 to high value chemicals are of particular interest. Current approaches for utilizing CO_2 as a feedstock chemical are electrochemical[10, 12-16] or hydrogenation[17-24] reactions that generate useful products such as formate (HCO_2) or methanol (CH_3OH) rely on catalysts. Both formate and methanol are appealing alternative fuel candidates because of their potential in direct fuel utilization devices like fuel cells.[25] Limitations on the use of these fuels are due in part to slow reaction rates and competitive byproduct reactions. Improvements on catalyst performance and selectivity are necessary to making progress towards utilization of alternative fuels.

0.2 Electrochemical CO_2 Reduction Strategies

The single electron reduction pathway of CO_2 to $CO_2^{\bullet -}$ requires a high standard reduction potential of –1.9 V vs SHE. The unfavourability of this pathway is a consequence of a high reorganization energy due to geometric rearrangement of CO_2 from linear to bent whereas reduction pathways that require multi-electrons and protons occur at lower thermodynamic reduction potentials (Table 0.1).[26-27] Despite lower thermodynamic potential requirements, electrochemical activation of CO_2 to higher value products like formate (HCO_2^-) is complicated by slow reaction kinetics and product selectivity. Thus, current catalysts used for these conversions often suffer from high overpotentials and low faradaic efficiencies from competitive

Table 0.1 CO_2 Reduction Potentials

reaction		$E^{o'}$ (V) vs. SHE
$CO_2 + 2H^+ + 2e^-$	HCO_2^-	−0.43
$CO_2 + 2H^+ + 2e^-$	$CO + H_2O$	−0.52
$CO_2 + 6H^+ + 6e^-$	$CH_3OH + H_2O$	-0.38
$CO_2 + 8H^+ + 8e^-$	$CH_4 + 2H_2O$	-0.24

side reactions like H_2 production.[28-30] Proposed reaction pathways for competing CO_2 reduction products to formate or CO are is depicted in Scheme 0.1.

Formate is a desirable 1 H^+ and 2 e^- CO_2 reduction product that can be used in direct formate fuel cells to generate energy[25, 31] or as a precursor to further reduced products like methanol

Scheme 0.1 Possible reduction pathways at reduced metal intermediate $[ML_2]^n$ in the presence of CO_2 and H^+.

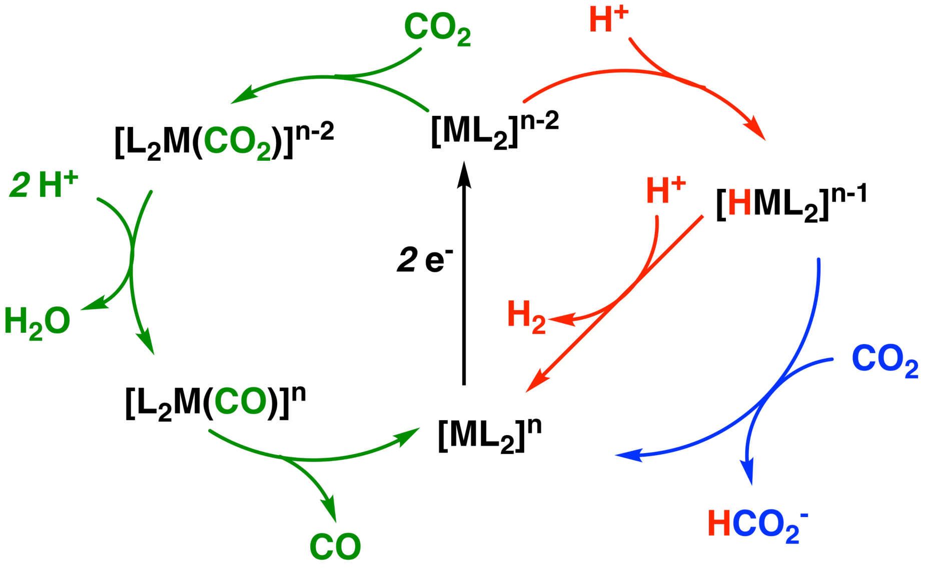

(CH_3OH).[17, 22, 32-34] Many approaches for CO_2 reduction to formate have been explored including hydrogenation,[24, 35] and electrochemical reduction.[29, 36] CO_2 hydrogenation requires high temperature and pressures compared to electrocatalytic systems.[23-24, 37] However, electrochemical catalysts are limited by low selectivity and high overpotentials.

A few notable examples of electrocatalysts with high selectively for formate (>90%) are shown in Table 0.2. Meyer and Brookhart generated a water soluble Ir POCOP complex that shows 93% faradaic efficiency for CO_2 reduction to formate at pH 7 with minimal background H_2 production. Hazari and Palmore et al.[38] report a trihydride Ir pincer compound that is proposed to rely secondary coordination H-bonding interactions with the ligand backbone to promote catalysis. Similarly, Artero et al.[39] described a highly active cobalt catalyst that incorporates electron donating phosphine ligands with two pendant amines, $P^{R}{}_2N^{R'}{}_2$. This cobalt catalyst utilizes secondary ligand stabilization effects of key intermediates for catalysis, where the most basic amine ligand exhibits the highest activity. Another particularly interesting

Table 0.2 Selective catalysts for CO_2 reduction to formate (HCO_2^{-}).

Catalyst	Potential (V) vs SCE Solvent H^+ source	HCO_2^- (%)	Ref
$(POCOP)Ir(NCCH_3)H_2$	-1.65 H_2O pH 7	93	Meyer and Brookhart (2014)
$(PNP)IrH_3$	−1.05 MeCN H_2O	97	Hazari and Palmore (2015)
$[CpCo(P^{Cy}{}_2N^{Bn}{}_2)]$	-1.75 MeCN H_2O	98	Artero (2017)
$[FeN(CO)_{12}]^-$	− 1.2 MeCN H_2O	94	Taheri and Berben (2015)

example is the $[Fe_4N(CO)_{12}]^-$ cluster investigated by Berben et al.[40] The driving force for hydride transfer from $[HFe_4N(CO)_{12}]^-$ to CO_2 was measured to be +5 kcal/mol in MeCN (uphill) and −8.5 kcal/mol in water (downhill). This switch in driving force for C-H bond formation suggests that secondary solvent effects are important considerations for catalysis.

In the proposed electrochemical process shown in Scheme 0.1, a metal complex undergoes electron transfer followed by a chemical step with CO_2 or H^+. The reduced metal species can (A) react with CO_2 to form a metal carboxylate intermediate or (B) protonate to generate a metal hydride. Reactivity at this branch point in the mechanism is important for determining reaction pathways for formate or CO production.

Reactivity at the reduced metal to favor protonation to form a metal hydride is one way to favor selectivity to formate. The metal hydride intermediate must be (1) sufficiently hydridic for CO_2 insertion to generate formate and (2) resist reactivity with the proton source to generate H_2. Few catalysts that meet these challenges have been reported.[38-41] As a result, better understanding of metal hydride reactivity is needed to guide catalyst design as well as to achieve further reduced products.

Fundamental mechanistic studies including the investigation of metal hydrides are necessary for catalyst selectivity. Molecular catalysts offer the advantage of synthetic control to tune redox potential and lower required overpotential costs.

0.3 Metal Hydricity in Catalysis

Metal hydrides are key intermediates in organometallic catalysis for important energy storage reactions including the evolution of H_2[42-44] and reduction of CO_2 to formate.[9, 45-47] The reactivity of metal hydrides can be described using a thermodynamic hydricity value (ΔG_{H^-}). Metal hydricity, or hydride donor ability (ΔG_{H^-}), is an experimentally determined parameter that describes the free energy associated with the heterolytic cleavage of a M-H bond to release a hydride (eq 1).

$$[\mathrm{HML}]^{+} \rightleftharpoons [\mathrm{ML}]^{2+} + \mathrm{H}^{-} \qquad \Delta G_{\mathrm{H}^-} \qquad (1)$$

Transition metal hydricity values can be determined using established thermodynamic schemes[47-50] and parameters such as reduction potential and pK_a.[51] Metal hydricity values for a series of metal hydrides[52] and organic compounds[53] have been measured. The hydricity of a metal complex can be modified by tuning the ligand electronic structure, changing the transition metal, or leveraging solvent effects.[52, 54-56]

Hydricity values have been shown to have a linear correlation with redox potential.[54] Thus redox potential offers an easily accessible experimental handle for estimating hydricity values, although there are some exceptions.[57-58] This hydricity-potential relationship highlights the sensitivity of hydricity due to changes in electronic structure of the metal complex. In contrast, the homolytic metal hydride BDFE values exhibit small changes with changes in ligand electronic structure and can be approximated to be ~ 60 kcal/mol.[54]

Using thermodynamic schemes (Scheme 0.2 and Scheme 0.3), hydricity values can be used to predict catalyst reactivity towards substrates in solution such as H^+ or CO_2. For example, H_2 evolution at a metal hydride (eq 4) is dependent on the hydricity of H_2 (ΔG_{H2}; eq 3) and the metal complex ($\Delta G_{H–}$; eq 1), as well as acid pK_a (eq 2). When these thermodynamic requirements are met, (ΔG_{HER}) < 0 (downhill) and H_2 is generated. Since H_2 production is a competitive pathway for selective hydride transfer to other substrates, like CO_2, gaining a thermodynamic understanding of H_2 production at metal hydride is crucial.

Scheme 0.2 Thermochemical Scheme for Heterolytic H_2 bond Formation at a Metal Hydride

Heterolytic H_2 Bond Formation

$$\begin{array}{llll}
\textbf{(1)} & [HML]^{+} & \rightleftharpoons [ML]^{2+} + H^{-} & \Delta G_{H^-} \\
\textbf{(2)} & HB & \rightleftharpoons H^{+} + B^{-} & \mathbf{1.37^{*}p\mathit{K}_a} \\
\textbf{(3)} & H^{+} + H^{-} & \rightleftharpoons H_2 & \mathbf{-\ 77\ kcal/mol} \\
\hline
\textbf{(4)} & [HML]^{+} + HB & \rightleftharpoons [ML]^{2+} + H_2 & \Delta G_{H2}
\end{array}$$

$$\Delta G_{H_2} = \Delta G_{H^-} + 1.37^{*}pK_a - 77\ \text{kcal/mol}$$

Scheme 0.3 Thermochemical Scheme for Hydride Transfer to CO_2

Free Energy of CO_2 Reduction to HCO_2^- Through H^- Transfer

$$\begin{array}{llll}
\textbf{(1)} & [HML]^{+} & \rightleftharpoons [ML]^{2+} + H^{-} & \Delta G_{H^-} \\
\textbf{(5)} & H^{-} + CO_2 & \rightleftharpoons HCO_2^{-} & \mathbf{44\ kcal/mol} \\
\hline
\textbf{(6)} & [HML]^{+} + CO_2 & \rightleftharpoons [ML]^{2+} + HCO_2^{-} &
\end{array}$$

$$\Delta G_{HCO2-} = (\Delta G_{H^-}) - 44\ \text{kcal/mol}$$

0.4 Research Goals

The research described in this dissertation is focused on understanding the thermodynamic and kinetic factors controlling reactivity of metal hydride complexes for electrochemical reduction reactions. This investigation focuses on understanding the H_2 evolution reaction (HER) pathway at metal hydride intermediates as a strategy for selective CO_2 reduction in water and organic solvents. To achieve this aim, a thermochemical approach is coupled to electrochemical mechanistic studies of Ni and Pt diphosphine complexes (Chart 0.1).

The Ni and Pt complexes used in this study have a bidentate bis(diphosphine)ethane ligand backbone.[59] The synthesis and characterization of the water soluble ligands tmepe (tmepe

= 1,2-bis[di(methoxyethyl)phosphino]ethane))[60-61] and dhmpe (dhmpe = 1,2-bis(di-(hydroxymethyl)phosphino)ethane)[55, 62] have been previously reported, while dmpe (dmpe = 1,2-bis(dimethylphosphino)ethane) is commercially available. Phosphine ligands were used because of the tunability of the phosphine donor strength and solubility properties. In addition, the phosphine donor atom offers an advantageous spectroscopic handle via ^{31}P NMR spectroscopy to track intermediates in mechanistic studies. Nickel and platinum metals were chosen for this work because they allow for further control over electronic structure. Both Ni and Pt favor formation 5-coordinate 18 e-, d^8 metal hydrides and 4-coordinate 16 e-, d^8 metal complexes following hydride transfer. These coordination changes maintain the desired diamagnetic properties of the metal complexes.

Thermodynamic studies of these complexes included measuring metal hydride hydricity ($\Delta G_{\mathrm{H}-}$) and pK_a values to benchmark reactivity. Metal hydricity is an important descriptor of metal hydride reactivity with H^+ or CO_2 substrates.[52, 54, 63-65] The heterogeneous catalysis community has found success using calculated thermodynamic activity descriptors, like substrate adsorption free energy, that describe critical bond making and breaking steps necessary for catalysis. These calculated thermodynamic descriptors and experimental catalytic activity are

Chart 0.1 Transition Metal Hydrides with diphosphine ligand frameworks

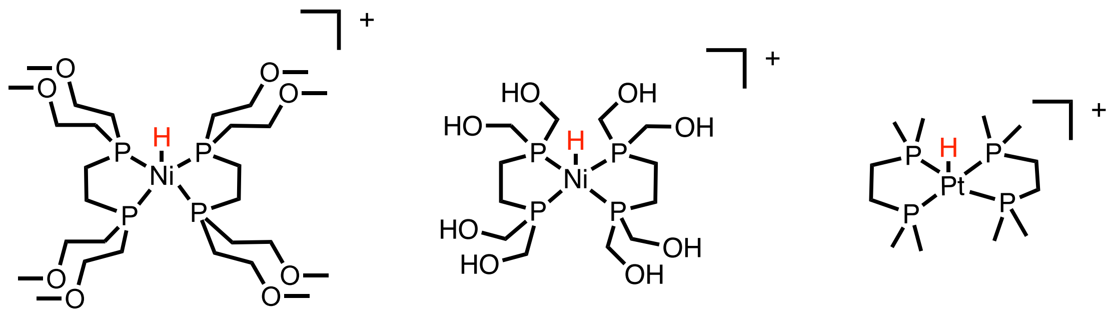

[HNi(tmpe)$_2$]$^+$ **[HNi(dhmpe)$_2$]$^+$** **[HPt(dmpe)$_2$]$^+$**

used to construct volcano plots that are used for catalyst development .[30] This work aims to investigate thermodynamic metal hydricity as a similar activity descriptor for homogeneous catalysts where making or breaking metal hydride bonds are critical steps.

Understanding and quantifying changes in metal hydricity across solvents, metals, and ligand frameworks allows for rational catalyst design. Herein, the metal hydricity (ΔG_{H^-}) of $[Ni(tmepe)_2]^{2+}$ was measured to describe hydride donor strength in water and organic solvents.[56] The hydricity values of $[Ni(dhmpe)_2]^{2+}$ and $[Pt(dmpe)_2]^{2+}$ have been previously reported by Tsay et al.[55] and Dubois et al.[49] respectively.

Coupling this fundamental thermodynamic approach with detailed mechanistic and electrochemical studies is crucial to better understand reaction mechanism during catalysis. Catalytic activity and mechanistic studies of HER and CO_2 reduction were conducted using the $[Pt(dmpe)_2]^{2+}$ complex using spectroscopic and electrochemical techniques.[66] Kinetic rates of metal hydride formation and competitive pathways were investigated using cyclic voltammetry. The synthesis and characterization of $[Ni(dhmpe)_2]^{2+}$ and $[Pt(dmpe)_2]^{2+}$ have been previously reported.[48, 55] Characterization of $[Ni(tmepe)_2]^{2+}$ was carried out using NMR spectroscopy, mass spectrometry and X-ray diffraction.[56]

0.5 References

1. Tarascon, J. M.; Armand, M., Issues and challenges facing rechargeable lithium batteries. *Nature* **2001,** *414* (6861), 359-367.

2. Abraham, K. M., Prospects and Limits of Energy Storage in Batteries. *The Journal of Physical Chemistry Letters* **2015,** *6* (5), 830-844.

3. Girishkumar, G.; McCloskey, B.; Luntz, A. C.; Swanson, S.; Wilcke, W., Lithium−Air Battery: Promise and Challenges. *The Journal of Physical Chemistry Letters* **2010,** *1* (14), 2193-2203.

4. Durbin, D. J.; Malardier-Jugroot, C., Review of hydrogen storage techniques for on board vehicle applications. *Int. J. Hydrogen Energy* **2013,** *38* (34), 14595-14617.

5. Birol, F. *World Energy Outlook Special Report 2016: Energy and Air Pollution*; International Energy Agency: 2016.

6. (IPCC), I. P. o. C. C. *Global Warming of 1.5°C.An IPCC Special Report on the impacts of global warming of 1.5°C above pre-industrial levels and related global greenhouse gas emission pathways, in the context of strengthening the global response to the threat of climate change,sustainable development, and efforts to eradicate poverty*; 2018.

7. Arakawa, H.; Aresta, M.; Armor, J. N.; Barteau, M. A.; Beckman, E. J.; Bell, A. T.; Bercaw, J. E.; Creutz, C.; Dinjus, E.; Dixon, D. A.; Domen, K.; DuBois, D. L.; Eckert, J.; Fujita, E.; Gibson, D. H.; Goddard, W. A.; Goodman, D. W.; Keller, J.; Kubas, G. J.; Kung, H. H.; Lyons, J. E.; Manzer, L. E.; Marks, T. J.; Morokuma, K.; Nicholas, K. M.; Periana, R.; Que, L.; Rostrup-Nielson, J.; Sachtler, W. M. H.; Schmidt, L. D.; Sen, A.; Somorjai, G. A.; Stair, P. C.; Stults, B. R.; Tumas, W., Catalysis Research of Relevance to Carbon Management: Progress, Challenges, and Opportunities. *Chem. Rev.* **2001,** *101* (4), 953-996.

8. Inglis, J. L.; MacLean, B. J.; Pryce, M. T.; Vos, J. G., Electrocatalytic pathways towards sustainable fuel production from water and CO_2. *Coord. Chem. Rev.* **2012,** *256* (21), 2571-2600.

9. Appel, A. M.; Bercaw, J. E.; Bocarsly, A. B.; Dobbek, H.; DuBois, D. L.; Dupuis, M.; Ferry, J. G.; Fujita, E.; Hille, R.; Kenis, P. J. A.; Kerfeld, C. A.; Morris, R. H.; Peden, C. H. F.; Portis, A. R.; Ragsdale, S. W.; Rauchfuss, T. B.; Reek, J. N. H.; Seefeldt, L. C.; Thauer, R. K.; Waldrop, G. L., Frontiers, Opportunities, and Challenges in Biochemical and Chemical Catalysis of CO_2 Fixation. *Chem. Rev.* **2013,** *113* (8), 6621-6658.

10. Kang, P.; Chen, Z.; Brookhart, M.; Meyer, T. J., Electrocatalytic Reduction of Carbon Dioxide: Let the Molecules Do the Work. *Topics in Catalysis* **2015,** *58* (1), 30-45.

11. Klankermayer, J.; Wesselbaum, S.; Beydoun, K.; Leitner, W., Selective Catalytic Synthesis Using the Combination of Carbon Dioxide and Hydrogen: Catalytic Chess at the Interface of Energy and Chemistry. *Angew. Chem. Int. Ed. (English)* **2016,** *55* (26), 7296-7343.

12. Elgrishi, N.; Chambers, M. B.; Wang, X.; Fontecave, M., Molecular polypyridine-based metal complexes as catalysts for the reduction of CO_2. *Chem. Soc. Rev.* **2017,** *46* (3), 761-796.

13. Savéant, J.-M., Molecular Catalysis of Electrochemical Reactions. Mechanistic Aspects. *Chem. Rev.* **2008,** *108* (7), 2348-2378.

14. Appel, A. M.; Newell, R.; DuBois, D. L.; Rakowski DuBois, M., Concentration of Carbon Dioxide by Electrochemically Modulated Complexation with a Binuclear Copper Complex. *Inorg. Chem.* **2005,** *44* (9), 3046-3056.

15. Costentin, C.; Drouet, S.; Robert, M.; Savéant, J.-M., Turnover Numbers, Turnover Frequencies, and Overpotential in Molecular Catalysis of Electrochemical Reactions. Cyclic Voltammetry and Preparative-Scale Electrolysis. *J. Am. Chem. Soc.* **2012,** *134* (27), 11235-11242.

16. Loewen, N. D.; Neelakantan, T. V.; Berben, L. A., Renewable Formate from C–H Bond Formation with CO_2: Using Iron Carbonyl Clusters as Electrocatalysts. *Acc. Chem. Res.* **2017,** *50* (9), 2362-2370.

17. Chu, W.-Y.; Culakova, Z.; Wang, B. T.; Goldberg, K. I., Acid-Assisted Hydrogenation of CO_2 to Methanol in a Homogeneous Catalytic Cascade System. *ACS Catal.* **2019,** *9* (10), 9317-9326.

18. Ye, J.; Cammarota, R. C.; Xie, J.; Vollmer, M. V.; Truhlar, D. G.; Cramer, C. J.; Lu, C. C.; Gagliardi, L., Rationalizing the Reactivity of Bimetallic Molecular Catalysts for CO_2 Hydrogenation. *ACS Catal.* **2018,** *8* (6), 4955-4968.

19. Zall, C. M.; Linehan, J. C.; Appel, A. M., A Molecular Copper Catalyst for Hydrogenation of CO_2 to Formate. *ACS Catal.* **2015,** *5* (9), 5301-5305.

20. Burgess, S. A.; Kendall, A. J.; Tyler, D. R.; Linehan, J. C.; Appel, A. M., Hydrogenation of CO_2 in Water Using a Bis(diphosphine) Ni–H Complex. *ACS Catal.* **2017,** *7* (4), 3089-3096.

21. Jeletic, M. S.; Mock, M. T.; Appel, A. M.; Linehan, J. C., A Cobalt-Based Catalyst for the Hydrogenation of CO_2 under Ambient Conditions. *J. Am. Chem. Soc.* **2013,** *135* (31), 11533-11536.

22. Bernskoetter, W. H.; Hazari, N., Reversible Hydrogenation of Carbon Dioxide to Formic Acid and Methanol: Lewis Acid Enhancement of Base Metal Catalysts. *Acc Chem Res* **2017,** *50* (4), 1049-1058.

23. Federsel, C.; Jackstell, R.; Beller, M., State-of-the-Art Catalysts for Hydrogenation of Carbon Dioxide. *Angew. Chem. Int. Ed. (English)* **2010,** *49* (36), 6254-6257.

24. Jessop, P. G.; Joó, F.; Tai, C.-C., Recent advances in the homogeneous hydrogenation of carbon dioxide. *Coord. Chem. Rev.* **2004,** *248* (21–24), 2425-2442.

25. An, L.; Chen, R., Direct formate fuel cells: A review. *J. Power Sources* **2016,** *320*, 127-139.

26. Morris, A. J.; Meyer, G. J.; Fujita, E., Molecular Approaches to the Photocatalytic Reduction of Carbon Dioxide for Solar Fuels. *Acc. Chem. Res.* **2009,** *42* (12), 1983-1994.

27. Sutin, N.; Creutz, C.; Fujita, E., Photo-Induced Generation of Dihydrogen and Reduction of Carbon Dioxide Using Transition Metal Complexes. *Comments Inorg. Chem.* **1997,** *19* (2), 67-92.

28. Taheri, A.; Berben, L. A., Making C-H bonds with CO_2: production of formate by molecular electrocatalysts. *Chem. Commun.* **2016,** *52* (9), 1768-1777.

29. Zhang, W.; Hu, Y.; Ma, L.; Zhu, G.; Wang, Y.; Xue, X.; Chen, R.; Yang, S.; Jin, Z., Progress and Perspective of Electrocatalytic CO_2 Reduction for Renewable Carbonaceous Fuels and Chemicals. *Advanced Science* **2018,** *5* (1), 1700275.

30. Seh, Z. W.; Kibsgaard, J.; Dickens, C. F.; Chorkendorff, I.; Nørskov, J. K.; Jaramillo, T. F., Combining theory and experiment in electrocatalysis: Insights into materials design. *Science* **2017,** *355* (6321).

31. Li, Y.; Feng, Y.; Sun, X.; He, Y., A Sodium-Ion-Conducting Direct Formate Fuel Cell: Generating Electricity and Producing Base. *Angew. Chem. Int. Ed. (English)* **2017**.

32. Huff, C. A.; Sanford, M. S., Cascade Catalysis for the Homogeneous Hydrogenation of CO_2 to Methanol. *J. Am. Chem. Soc.* **2011,** *133* (45), 18122-18125.

33. Schneidewind, J.; Adam, R.; Baumann, W.; Jackstell, R.; Beller, M., Low-Temperature Hydrogenation of Carbon Dioxide to Methanol with a Homogeneous Cobalt Catalyst. *Angew. Chem. Int. Ed. (English)* **2017,** *56* (7), 1890-1893.

34. Wesselbaum, S.; Moha, V.; Meuresch, M.; Brosinski, S.; Thenert, K. M.; Kothe, J.; Stein, T. v.; Englert, U.; Hölscher, M.; Klankermayer, J.; Leitner, W., Hydrogenation of carbon dioxide to methanol using a homogeneous ruthenium–Triphos catalyst: from mechanistic investigations to multiphase catalysis. *Chem. Sci.* **2015,** *6* (1), 693-704.

35. Jeletic, M. S.; Hulley, E. B.; Helm, M. L.; Mock, M. T.; Appel, A. M.; Wiedner, E. S.; Linehan, J. C., Understanding the Relationship Between Kinetics and Thermodynamics in CO_2 Hydrogenation Catalysis. *ACS Catal.* **2017,** *7* (9), 6008-6017.

36. Taheri, A.; Carr, C. R.; Berben, L. A., Electrochemical Methods for Assessing Kinetic Factors in the Reduction of CO_2 to Formate: Implications for Improving Electrocatalyst Design. *ACS Catal.* **2018,** *8* (7), 5787-5793.

37. Langer, R.; Diskin-Posner, Y.; Leitus, G.; Shimon, L. J. W.; Ben-David, Y.; Milstein, D., Low-Pressure Hydrogenation of Carbon Dioxide Catalyzed by an Iron Pincer Complex Exhibiting Noble Metal Activity. *Angew. Chem. Int. Ed. (English)* **2011,** *50* (42), 9948-9952.

38. Ahn, S. T.; Bielinski, E. A.; Lane, E. M.; Chen, Y.; Bernskoetter, W. H.; Hazari, N.; Palmore, G. T. R., Enhanced CO_2 electroreduction efficiency through secondary coordination effects on a pincer iridium catalyst. *Chem. Commun.* **2015,** *51* (27), 5947-5950.

39. Roy, S.; Sharma, B.; Pecaut, J.; Simon, P.; Fontecave, M.; Tran, P. D.; Derat, E.; Artero, V., Molecular Cobalt Complexes with Pendant Amines for Selective Electrocatalytic Reduction of Carbon Dioxide to Formic Acid. *J. Am. Chem. Soc.* **2017,** *139* (10), 3685-3696.

40. Taheri, A.; Thompson, E. J.; Fettinger, J. C.; Berben, L. A., An Iron Electrocatalyst for Selective Reduction of CO_2 to Formate in Water: Including Thermochemical Insights. *ACS Catal.* **2015,** *5* (12), 7140-7151.

41. Kang, P.; Meyer, T. J.; Brookhart, M., Selective electrocatalytic reduction of carbon dioxide to formate by a water-soluble iridium pincer catalyst. *Chem. Sci.* **2013,** *4* (9), 3497-3502.

42. Bullock, R. M.; Appel, A. M.; Helm, M. L., Production of hydrogen by electrocatalysis: making the H-H bond by combining protons and hydrides. *Chem Commun (Camb)* **2014,** *50* (24), 3125-43.

43. Rakowski Dubois, M.; Dubois, D. L., Development of Molecular Electrocatalysts for CO_2 Reduction and H_2 Production/Oxidation. *Acc. Chem. Res.* **2009,** *42* (12), 1974-1982.

44. Thoi, V. S.; Sun, Y.; Long, J. R.; Chang, C. J., Complexes of earth-abundant metals for catalytic electrochemical hydrogen generation under aqueous conditions. *Chem. Soc. Rev.* **2013,** *42* (6), 2388-2400.

45. Leitner, W., Carbon Dioxide as a Raw Material: The Synthesis of Formic Acid and Its Derivatives from CO_2. *Angewandte Chemie International Edition in English* **1995,** *34* (20), 2207-2221.

46. Fujita, E., Photochemical carbon dioxide reduction with metal complexes. *Coord. Chem. Rev.* **1999,** *185–186*, 373-384.

47. DuBois, D. L.; Berning, D. E., Hydricity of transition-metal hydrides and its role in CO_2 reduction. *Appl. Organomet. Chem.* **2000,** *14* (12), 860-862.

48. A. Miedaner, D. L. D., and C. J. Curtis, Generation of Metal Formyl Complexes Using Nickel and Platinum Hydrides as Reducing Agents. *Organometallics* **1993,** *12*, 299-303.

49. Berning, D. E.; Noll, B. C.; DuBois, D. L., Relative Hydride, Proton, and Hydrogen Atom Transfer Abilities of $[HM(diphosphine)_2]PF_6$ Complexes (M = Pt, Ni). *J. Am. Chem. Soc.* **1999,** *121* (49), 11432-11447.

50. D. E. Berning, A. M., C. J. Curtis, B. C. Noll, M. C. Rakowski DuBois, and D. L. DuBois, Free-Energy Relationships between the Proton and Hydride Donor Abilities of $[HNi(diphosphine)_2]^+$ Complexes and the Half-Wave Potentials of Their Conjugate Bases. *Organometallics* **2001,** *20*, 1832-1839.

51. C. J. Curtis, A. M., W. W. Ellis, and D. L. DuBois, Measurement of the Hydride Donor Abilities of $[HM(diphosphine)_2]^+$ Complexes (M= Ni, Pt) by Heterolytic Activation of Hydrogen. *J. Am. Chem. Soc.* **2002,** *124* (9), 1918-1925.

52. Wiedner, E. S.; Chambers, M. B.; Pitman, C. L.; Bullock, R. M.; Miller, A. J. M.; Appel, A. M., Thermodynamic Hydricity of Transition Metal Hydrides. *Chem. Rev.* **2016,** *116* (15), 8655-8692.

53. Ilic, S.; Pandey Kadel, U.; Basdogan, Y.; Keith, J. A.; Glusac, K. D., Thermodynamic Hydricities of Biomimetic Organic Hydride Donors. *J. Am. Chem. Soc.* **2018,** *140* (13), 4569-4579.

54. Waldie, K. M.; Ostericher, A. L.; Reineke, M. H.; Sasayama, A. F.; Kubiak, C. P., Hydricity of Transition-Metal Hydrides: Thermodynamic Considerations for CO_2 Reduction. *ACS Catal.* **2018,** *8* (2), 1313-1324.

55. Tsay, C.; Livesay, B. N.; Ruelas, S.; Yang, J. Y., Solvation Effects on Transition Metal Hydricity. *J. Am. Chem. Soc.* **2015,** *137* (44), 14114-14121.

56. Ceballos, B. M.; Tsay, C.; Yang, J. Y., CO_2 reduction or HCO_2- oxidation? Solvent-dependent thermochemistry of a nickel hydride complex. *Chem. Commun.* **2017,** *53* (53), 7405-7408.

57. Raebiger, J. W.; DuBois, D. L., Thermodynamic Studies of HRh(depx)$_2$ and [(H)$_2$Rh(depx)$_2$](CF$_3$SO$_3$): Relationships between Five-Coordinate Monohydrides and Six-Coordinate Dihydrides. *Organometallics* **2005,** *24* (1), 110-118.

58. A. Miedaner, J. W. R., C. J. Curtis, S. M. Miller, and D. L. DuBois,, Thermodynamic Studies of [HPt(EtXantphos)$_2$]$^+$ and [(H)$_2$Pt(EtXantphos)$_2$]$^{2+}$. *Organometallics* **2004,** *23*, 2670-2679.

59. J. W. Raebiger, A. M., C. J. Curtis, S. M. Miller, O. P. Anderson, and D. L. DuBois, Using Ligand Bite Angles to Control the Hydricity of Palladium Diphosphine Complexes. *J. Am. Chem. Soc.* **2004,** *126*, 5502-5514.

60. K. Ospay, J. D., K. M. Nsunda, E. Roli, R. Houriet, and L. Hevesi, Experimental and Theoretical Studies of the Gas-Phase Protonation of Vinyl Ethers, Vinyl Sulfide, and Vinyl Selenides. *J. Am. Chem. Soc.* **1989,** *111* (14), 5028-5036.

61. Deutsch, A. H. a. E. A., 1,2-Bis[bis(methoxyethyl)phosphino]ethane, 1,2-bis[bis(methoxypropyl)ohosphino]ethane and their quarternary salts. Unexpected hydroltyic susceptibility of the ethanediylbis[bis(methoxyethyl)phosphonium]-PH,P' H' cation. *J. Organomet. Chem.* **1993,** *460*, 19-23.

62. Nieckarz, G. F.; Weakley, T. J. R.; Miller, W. K.; Miller, B. E.; Lyon, D. K.; Tyler, D. R., Generation of 19-Electron Adducts in Aqueous Solution Using the Water-Soluble (HOCH$_2$)$_2$PCH$_2$CH$_2$P(CH$_2$OH)$_2$ Ligand. *Inorg. Chem.* **1996,** *35* (6), 1721-1724.

63. Barlow, J. M.; Yang, J. Y., Thermodynamic Considerations for Optimizing Selective CO$_2$ Reduction by Molecular Catalysts. *ACS Central Science* **2019,** *5* (4), 580-588.

64. Matsubara, Y.; Fujita, E.; Doherty, M. D.; Muckerman, J. T.; Creutz, C., Thermodynamic and Kinetic Hydricity of Ruthenium(II) Hydride Complexes. *J. Am. Chem. Soc.* **2012,** *134* (38), 15743-15757.

65. C. J. Curtis, A. M., J. W. Raebiger, and D. L. DuBois, Periodic Trends in Metal Hydride Donor Thermodynamics: Measurement and Comparison of the Hydride Donor Abilities of the Series $HM(PNP)_2^+$ (M= Ni, Pd, Pt; PNP= $Et_2PCH_2N(Me)$ CH_2PEt_2). *Organometallics* **2004,** *23*, 511-516.

66. Ceballos, B. M.; Yang, J. Y., Directing the reactivity of metal hydrides for selective CO_2 reduction. *Proceedings of the National Academy of Sciences* **2018,** *115* (50), 12686.

CHAPTER 1

Hydricity Determination, Solvent Effects, and Reactivity of $[HNi(tmepe)_2]^+$

Portions of this chapter have been published:
Ceballos, B. M.; Tsay, C.; and Yang, J. Y.; *Chem. Commun*, **2017**, *53*, 7405-7408.

1.1 Motivations and Specific Aims

Catalytic H^+ and CO_2 reduction reactions both share a key metal hydride intermediate. Thus, gaining a better understanding of metal hydride formation and reactivity is necessary for designing catalysts for these reactions. A water-soluble Ni(II) complex incorporating two electron donating bidentate phosphorous ligands was synthesized and characterized using NMR spectroscopy, mass spectrometry, and X-ray crystallography. Additionally, the thermodynamic hydricity (ΔG_{H-}) was measured and benchmarked relative to H_2 formation in acetonitrile, dimethylsufloxide (DMSO), and water to assess H^+ and CO_2 reduction capabilities. This type of quantitative thermodynamic analysis of potential catalysts can be used to direct selective catalytic pathways and to improve catalyst activity as described in Chapter 2.

1.2 Background

The reduction of CO_2 to formate is a convenient path to a carbon-neutral renewable fuel that can be transported as a liquid.[1-6] Formate can be produced from CO_2 through hydrogenation[1-2, 7-17] or direct electrochemical reduction.[18-29] Utilization of formate can be achieved through dehydrogenation reactions to liberate dihydrogen[3, 7, 30-37] or by direct formate oxidation in a fuel cell to generate energy.[38-43] All of these routes for fuel production and utilization require catalysts. For homogeneous catalysts, these reactions both proceed through a transition metal hydride intermediate (Scheme 1.1).

Scheme 1.1. Proposed mechanism for metal hydride $[HML_n]^{n-1}$ formation and H^+ and CO_2 reduction.

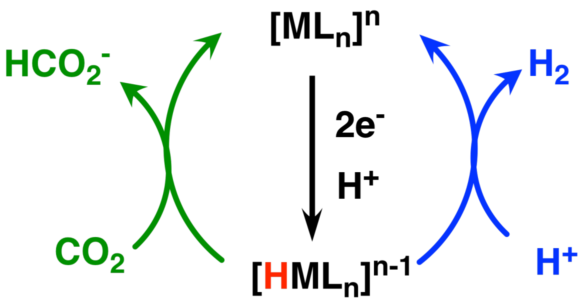

The thermodynamic cycle for hydride transfer to CO_2 to generate formate is outlined in Scheme 1.2. Comparison of the hydride transfer energy of a transition metal hydride (eq 1, ΔG_{H^-} (MH), or hydricity) to the hydride transfer energy of formate (eq 2, $\Delta G_{H^-}(HCO_2^-)$ indicates whether CO_2 reduction or formate oxidation is exergonic or endergonic (eq 3). Values for $\Delta G_{H^-}(HCO_2^-)$ have been measured or estimated in several solvents.[44-47] To develop a thermodynamic framework to guide catalyst design for the interconversion of CO_2 to formate, our group[44] and others[8, 18-19, 45, 48-56] have been quantifying hydricity values for transition metal hydrides.

A former postdoctoral associate Dr. Charlene Tsay, measured the hydricity (ΔG_{H^-}) of $[HNi(DHMPE)_2]^+$ (DHMPE= 1,2-bis(di-(hydroxymethyl)phosphino)ethane, Chart 1.1) versus dihydrogen in acetonitrile (CH_3CN), dimethylsulfoxide (DMSO), and water. In solvents with higher polarity, the hydricity of $[HNi(DHMPE)_2]^+$ shifts to lower values to

Scheme 1.2. Thermodynamic cycle for hydride transfer to CO_2 to generate formate by a metal hydride.

Free Energy of CO_2 Reduction to HCO_2^- Through H^- Transfer

$$\text{(1)}\quad [HML]^+ \rightleftharpoons [ML]^{2+} + H^- \qquad \Delta G^0_{H^-}$$

$$\text{(2)}\quad H^- + CO_2 \rightleftharpoons HCO_2^- \qquad -\Delta G^0_{H^-}(HCO_2^-)$$

$$\text{(3)}\quad [HML]^+ + CO_2 \rightleftharpoons [ML]^{2+} + HCO_2^- \quad \Delta G^0 = (\Delta G^0_{H^-}) - \Delta G^0_{H^-}(HCO_2^-)$$

become a better hydride donor.[44] In aqueous solutions, the decrease of ΔG_{H^-} for $[HNi(TMEPE)_2]^+$ (**1**) is greater in magnitude than the decrease in ΔG_{H^-} for formate. The change in free energy for CO_2 reduction to formate in water was initially observed by Creutz and coworkers with $[HRu(\eta^6\text{-}C_6Me_6)(bpy)]^+$,[52-54] and subsequent studies show a similar trend among transition metal hydrides.[18-19, 52, 55, 57-59] However, with only a few exceptions,[19, 54, 59] the ultimate reaction favorability with CO_2 remains the same across solvents. In other words, while the magnitude of the free energy changes, but the overall free energy remains either positive or negative. This is true of $[HNi(DHMPE)_2]^+$ where the free energy for hydride transfer to CO_2 (eq 3) decreases from 13.5 and 13.4 kcal/mol in DMSO and CH_3CN, and to 5.9 kcal/mol in water, but the reaction remains endergonic in all three solvents.

$[HNi(DHMPE)_2]^+$ was modified to increase the metal hydride donor strength (or decrease ΔG_{H^-}) in order to favor aqueous CO_2 reduction to formate. To increase the donor strength of the ligand while maintaining water solubility, DHMPE was replaced with TMEPE (TMEPE = 1,2-bis[di(methoxyethyl)phosphino]ethane), shown in Scheme 1.1. In TMEPE,

Chart 1.1. Nickel complex with water-soluble diphosphine ligand frameworks.

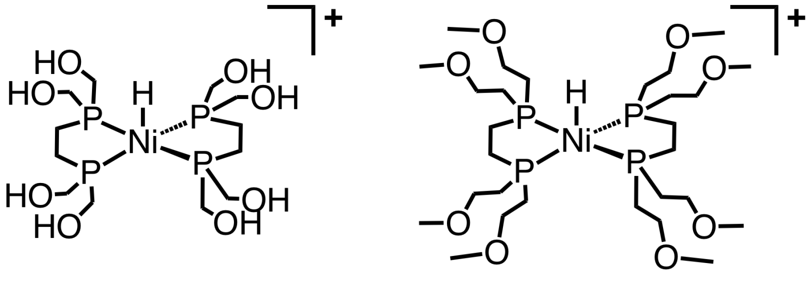

HNi(DHMPE)$_2$

$[HNi(TMEPE)_2]^+$ (1)

the electron-withdrawing oxygen heteroatom is further extended from the phosphine ligand by an additional methylene group. Additionally, previously it was observed that DHMPE was unstable to alkaline conditions, which is attributed to deprotonation of the distal alcohols. To circumvent this issue, the alcohols were replaced with methoxide substituents in TMEPE.

1.3 Results and Discussion

1.3.1 Synthesis and structure of $[Ni(TMEPE)_2][BF_4]_2$, $[HNi(TMEPE)_2][BF_4]$, and $[Ni(TMEPE)_2]$ (TMEPE = 1,2-bis[di(methoxyethyl)phosphino]ethane)

1,2-bis[di(methoxyethyl)phosphino]ethane (TMEPE) was synthesized from methyl vinyl ether[60] in 63% yield according to a modified preparation (see Experimental Section).[61] The ^1H and $^{31}P\{^1H\}$ NMR spectra (Figures 1.2 and 1.3) are consistent with the original preparation.[61]

The Ni(II) complex $[Ni(TMEPE)_2][BF_4]_2$ (**2**) was synthesized by the addition of two equivalents of TMEPE to $[Ni(CH_3CN)_6](CH_3CN)_{0.5}[BF_4]_2$ in CH_3CN and upon purification was isolated in quantitative yield. **2** was characterized by ^1H and $^{31}P\{^1H\}$ spectroscopy in water and organic solvents.[9] Single crystals suitable for analysis by X-ray crystallography were grown by vapor diffusion of diethyl ether into a THF/toluene solution; the solid-state structure is shown in Figure 1. The nickel ion lies on an inversion center and the asymmetric unit contains only one TMEPE ligand; the other half of the molecule is generated by symmetry, resulting in an ideal square planar geometry around the metal center.

The Ni(0) complex, $Ni(TMEPE)_2$ (**3**), was prepared by adding two equivalents of TMEPE to $Ni(COD)_2$ in THF at −35 °C, resulting in an immediate color change from yellow to dark orange-brown. The solution was warmed to room temperature and stirred overnight to give **3** in 95% yield. Complex **3** was characterized by ^1H and $^{31}P\{^1H\}$ NMR spectroscopy (Figures 1.6 and 1.7).

The nickel hydride complex $[HNi(TMEPE)_2][BF_4]$ (**1**, Chart 1.1), was generated by *in situ* protonation of **3** by the addition of one equivalent of acid in either H_2O, DMSO, or CH_3CN. The ^1H and $^{31}P\{^1H\}$ NMR spectra for **1** are shown in Figures 1.8 - 1.13.

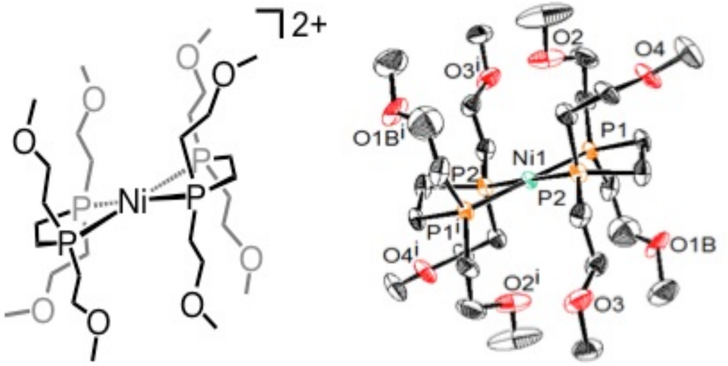

Figure 1.1. Structural representation (left) and solid-state structure (right) of $[Ni(TMEPE)_2][BF_4]_2$ (**2**). Crystal structure details: asymmetric unit contains half of the molecule, other half generated by inversion around Ni; only one orientation of a disordered methoxyethyl group shown; thermal ellipsoids drawn at 50%; hydrogen atoms and two BF_4 anions omitted for clarity.

1.3.2 Benchmarking Metal Hydricity Values in Acetonitrile, Dimethylsulfoxide (DMSO), and Water

The hydricity values were measured using the thermodynamic cycle shown in Scheme 1.3. The equilibrium constant (K_{eq}) associated with the formation of complex **1** from **2** using H_2 in the presence of a base (eq 4) was measured in CH_3CN, DMSO, and H_2O. With this method, the estimated hydricity is benchmarked to the heterolytic bond cleavage energy of H_2 ($\Delta G°_{H2}$)[62] and the pK_a values of the conjugate acids in the solvent of interest (Scheme 1.3). The values for the previously studied $[HNi(DHMPE)_2]^+$ were measured using the same method.

Scheme 1.3. Thermodynamic cycle used to determine hydricity values relative to the heterolysis of H_2

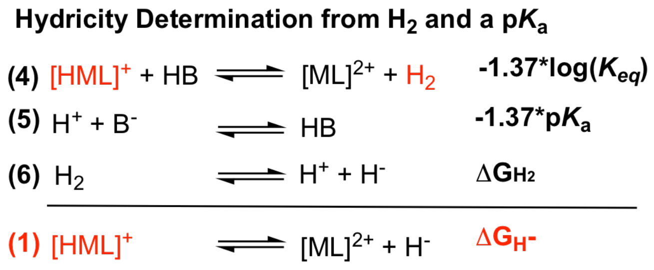

In each solvent, the reaction shown in eq 4 was monitored by ^1H and $^{31}P\{^1H\}$ NMR spectroscopy. The relative integration for $[HNi(TMEPE)_2][BF_4]$ (**1**) and $[Ni(TMEPE)_2][BF_4]_2$ (**2**) were compared to an internal capillary reference containing 0.5 M H_3PO_4 in D_2O (eq 4). To ensure that equilibrium was achieved, K_{eq} was measured when the relative amounts of **1** to **2** did not change for 3 days.

Hydricity values for **1** in non-aqueous and aqueous solvents are listed in Table 1.1 and shown in Scheme 1.4. In CH_3CN, the base Et_3N (pK_a of $[HNEt_3]^+ = 18$)[63] was used to establish an equilibrium between **1** and **2**. Coordination of NEt_3 to **2** was not observed by $^{31}P\{^1H\}$ NMR spectroscopy. The relative $^{31}P\{^1H\}$ NMR integrations at equilibrium resulted in a hydricity for **1** of 50.6 kcal/mol in CH_3CN. The hydricity of **1** in DMSO was determined using 1,8-diazabicycloundec-7-ene (DBU) as a base (pK_a of $[HDBU]^+ = 12$).[64] Again, no coordination of DBU was observed by $^{31}P\{^1H\}$ NMR spectroscopy. The reaction reached equilibrium after 6 days, and the measured K_{eq} resulted in a hydricity of 47.1 kcal/mol. In water, H_2 heterolysis was conducted in phosphate buffered solutions at pH 7, 7.5, and 8 with no added base. Equilibrium was achieved at pH 8 after 15 days and leads to a ΔG_{H^-}(**1**) of 22.8 kcal/mol.

Table 1.1. Experimentally determined hydricity values (ΔG°_{H-}) for $[HNi(TMEPE)_2]^+$ (**1**) with conjugate acid p*K*a values of bases used in acetonitrile (CH_3CN), dimethylsufloxide (DMSO), and phosphate buffer at pH 8 in H_2O (eq 1, Scheme 1.2) and published values for the heterolytic cleavage energy of H_2 (ΔG°_{H2}) and $\Delta G^\circ_{H-}(HCO_2^-)$. Shaded gray: free energy for H^- transfer from MH to CO_2 according to eq 3 in Scheme 1.2. All ΔG values are given in kcal/mol.

Solvent (ϵ)	ΔG°_{H2}	ΔG°_{H-} (HCO_2^-)	$[HNi(TMEPE)_2]^+$		ΔG° (eq 3, Scheme 1)	
			Conj. Acid (pK_a, eq 5)	ΔG°_{H-}	[g]$[HNi(TMEPE)_2]^+$	$[HNi(DHMPE)_2]^+$
CH_3CN (*38*)	[a]76	[c]44	[e]$[HNEt_3]^+$ (18)	50.6	6.6	13.4
DMSO (*50*)	[a]60	[d]42	[f][HDBU]$^+$ (12)	47.1	5.1	13.5
H_2O (*80*)	[b]34	[b]24	H_3PO_4 (7)	22.8	–1.2	5.9

[a]ref 62. [b]ref 45. [c]ref 47. [d]ref 46. [e]ref 63. [f]ref 64. [g]ΔG°_{H-} from ref 44.

Scheme 1.4. Calculation for the equilibrium reaction between complex **1** and **2** for hydricity value (ΔG°_{H-}) determination.

$$\textbf{(7)}\quad [NiL_2]^{2+} + B + H_2 \rightleftharpoons [HNL_2]^+ + BH$$

	$[NiL_2]^{2+}$	B	H_2	$[HNL_2]^+$	BH
Initial	X	X			
Change	$-\Delta$	$-\Delta$		Δ	Δ
Equilibrium	$X-\Delta$	$X-\Delta$		Δ	Δ

$$Y = \frac{[HNiL_2^{+}]}{[NiL_2^{2+}]} \qquad Z = \frac{[BH]}{[B^-]} \qquad K_{eq} = \frac{[HNiL_2^{+}]\,[BH]}{[NiL_2^{2+}]\,[B^-]} = Y \bullet Z$$

Table 1.2. Equilibrium constant (K_{eq}) calculation data for H_2 formation by complex **1** according to eq 7 in Scheme 1.4 in acetonitirile (CH_3CN), dimethylsufoxide (DMSO), and water (H_2O).

Solvent	**X (M)**	**n (eq)**	**Y**	**Δ**	**Z**	**K_{eq}**	**BH**	**pK_a**	**ΔG_{H2} (kcal/ mol)**	**ΔG_{H-} (kcal/ mol)**
CH_3CN	0.024	1	1.15	1.3 X 10^{-3}	1.15	1.32	Et_3NH^+	18	76	50
DMSO	0.015	1	0.09	1.2 X 10^{-3}	0.09	8.5 X 10^{-3}	$DBUH^+$	12	60	47
H_2O	0.024	1	0.5	7.9 X 10^{-3}	0.5	0.5	HCO_3^-	8	34	22

Hydride donor strength increases with increasing solvent polarity, as shown in Table 1.1 and Scheme 1.5. By comparing the relative hydricity values of **1** (22. 8 kcal/mol) to formate (24.1 kcal/mol), the free energy of hydride transfer to CO_2 is still endergonic in organic solvents, but is now exergonic by –1.2 kcal/mol in water.

Scheme 1.5. Benchmarking of thermodynamic hydricity values ΔG_{H-} (kcal/mol) in acetonitrile (CH_3CN), dimethylsulfoxide (DMSO), and water.

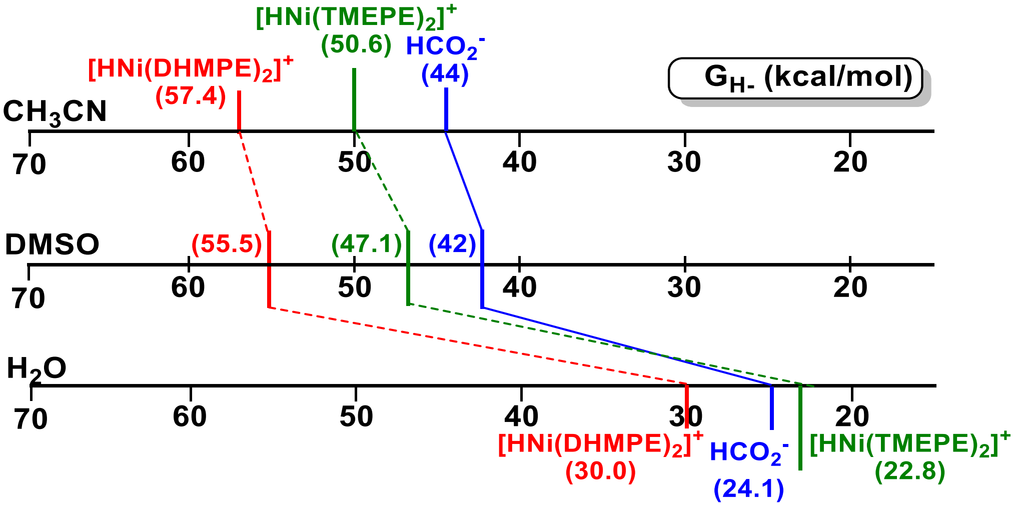

1.3.3 Reactivity of $[HNi(TMEPE)_2]^+$ towards CO_2 reduction and formate (HCO_2^-) oxidation reactions

As expected, the experimentally measured hydricity values for $[HNi(TMEPE)_2]^+$ are lower, or more hydridic, than $[HNi(DHMPE)_2]^+$ in CH_3CN, DMSO, and water. While hydride transfer from $[HNi(TMEPE)_2]^+$ is still endergonic in CH_3CN and DMSO, it is now exergonic in water. The hydricities of many transition metal complexes have been measured in CH_3CN, water, or both; this is one of few known complexes to exhibit solvent-dependent reactivity with CO_2.[19, 53-54, 59, 65-66]

The hydricity measurement was validated by examining the oxidation of lithium formate by **2**. Upon addition of lithium formate to **2**, clean hydride transfer is observed to generate **1** and CO_2 (Figures 1.2 and 1.3) in CH_3CN and DMSO, reflecting the free energies of –6.6 and –5.1 kcal/mol, respectively, associated with this reaction. As expected, no reaction is observed for the equivalent reaction in aqueous solution over 1 day, as it is endergonic (Figure 1.4).

$$[Ni(tmepe)_2][BF_4]_2 + [Li][HCO_2] \underset{1\ atm\ CO_2}{\rightleftharpoons} [HNi(tmepe)_2][BF_4] + CO_2 + [Li][BF_4]$$

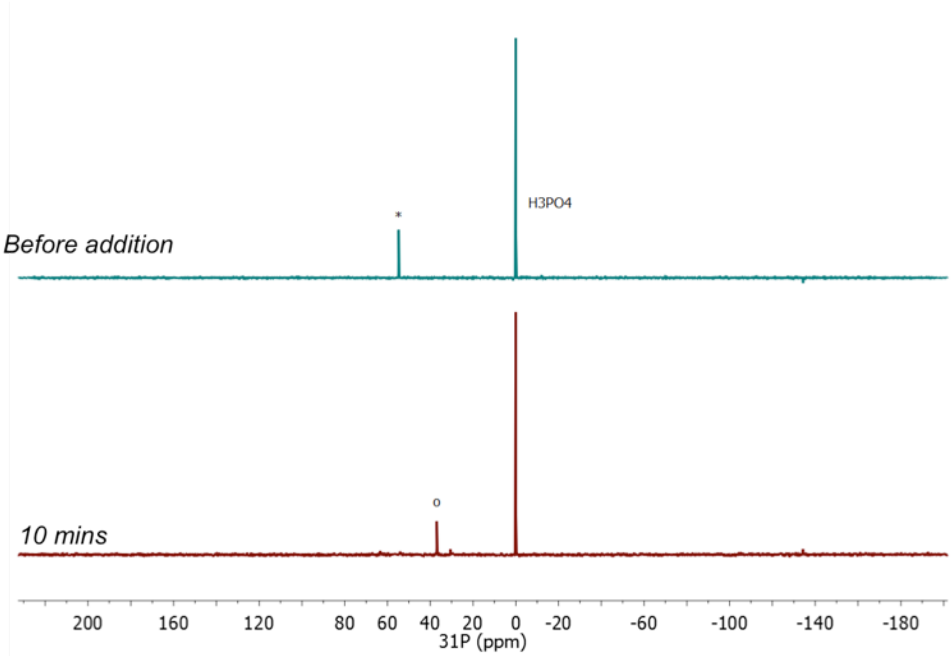

Figure 1.2. $^{31}P\{^1H\}$ NMR spectrum showing complete lithium formate oxidation by complex **2** (*) in DMSO-d_6 to generate complex **1** (o) after the addition of 1 eq of lithium formate, under N_2.

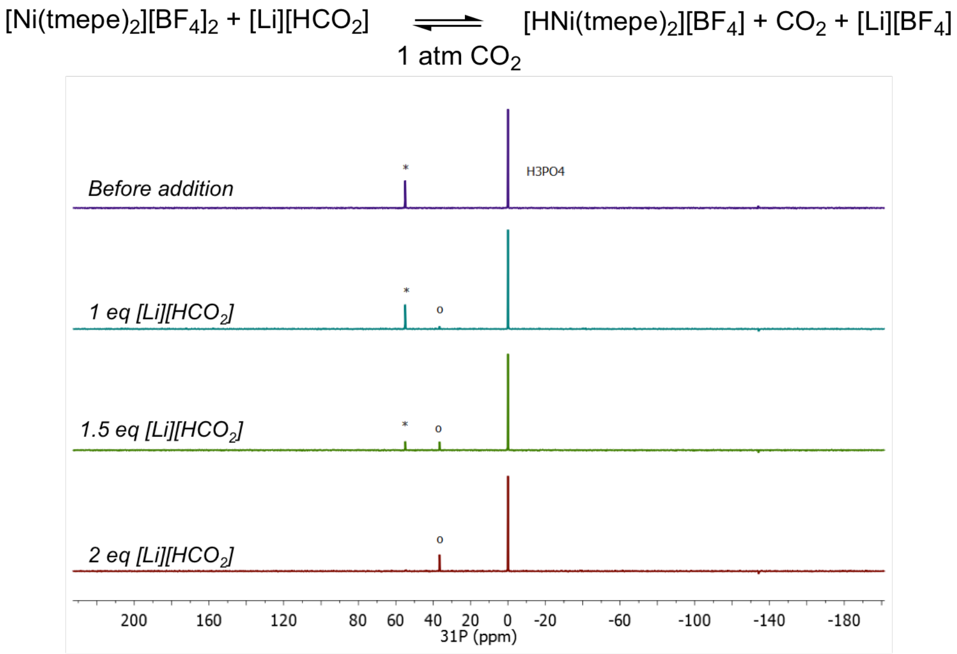

Figure 1.3. $^{31}P\{^1H\}$ NMR spectrum showing lithium formate oxidation by complex **2** (*) in CD_3CN to generate complex **1** (o) after the addition of 2 eq of lithium formate under N_2.

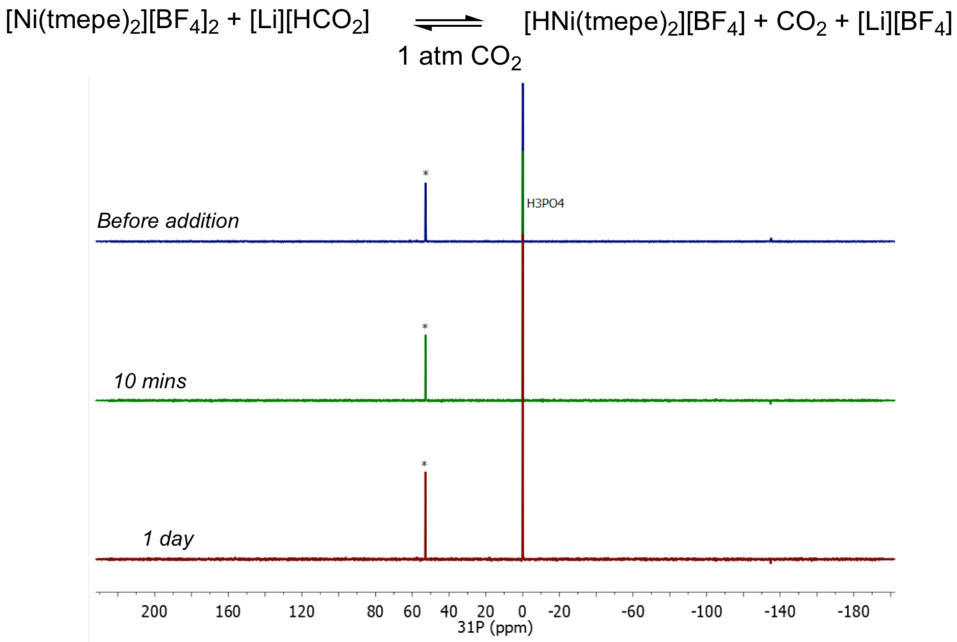

Figure 1.4. $^{31}P\{^1H\}$ NMR spectrum of no reaction between complex **2** (*) and one equivalent of lithium formate in D_2O under CO_2.

To observe the reverse reaction, hydride transfer from **1** to CO_2 to generate formate was attempted in aqueous solution. Metal hydrides are prone to protonation in protic solvent to evolve dihydrogen. However, the free energy of protonation is pH dependent according to eq 7. Using the heterolytic bond cleavage energy of H_2 and the hydricity (ΔG_{H-}) of $[HNi(TMEPE)_2]^+$ (**1**), transfer of the hydride to a proton to generate H_2 is predicted to be thermoneutral ($\Delta G = 0$) at pH 8.7, resulting in equal concentrations of **1** and **2** at equilibrium under standard conditions. The concentration of the metal hydride (**1**) and Ni(II) complex (**2**) observed at pH 9.0 bicarbonate buffer (Figure 1.5) is consistent with the calculated equilibrium from eq 7. As expected, nickel hydride (**1**) can be cleanly isolated in a carbonate buffer at pH 10.5, with no observed protonation to generate H_2 after 6 days (Figure1.6).

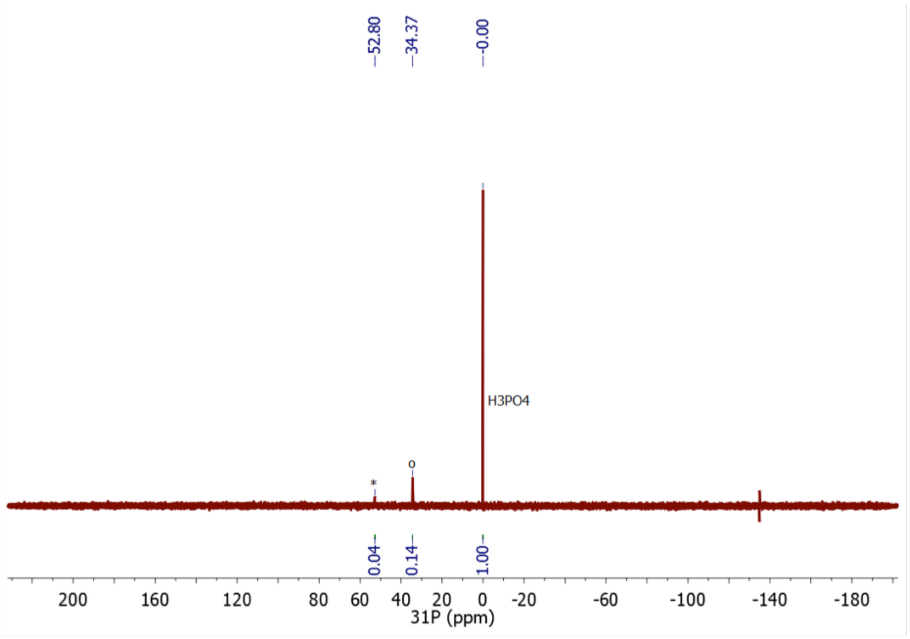

Figure 1.5. $^{31}P\{^1H\}$ NMR spectrum showing nickel hydride complex **3** (o) in pH 9 carbonate buffered D_2O with background protonation to complex **2** (*). Complex **1** generated from protonation of Ni(0) complex **3** by $[PhNH_4][BF_4]$ in CD_3CN.

Addition of 1 atm of CO_2 to solutions of **1** at pH 9 in a J. Young tube acidifies the solution to pH 7, which results in protonation of **1** to **2** along with some decomposition attributed to trace oxygen (Figure 1.7). At higher pH conditions where **1** is stable to protonation, CO_2 primarily exists as carbonate or bicarbonate. In a bicarbonate buffer at pH 10.4, hydride transfer from **1** is not observed over the course of several days although the reaction was not performed under an atmosphere of CO_2 due to solution acidification.

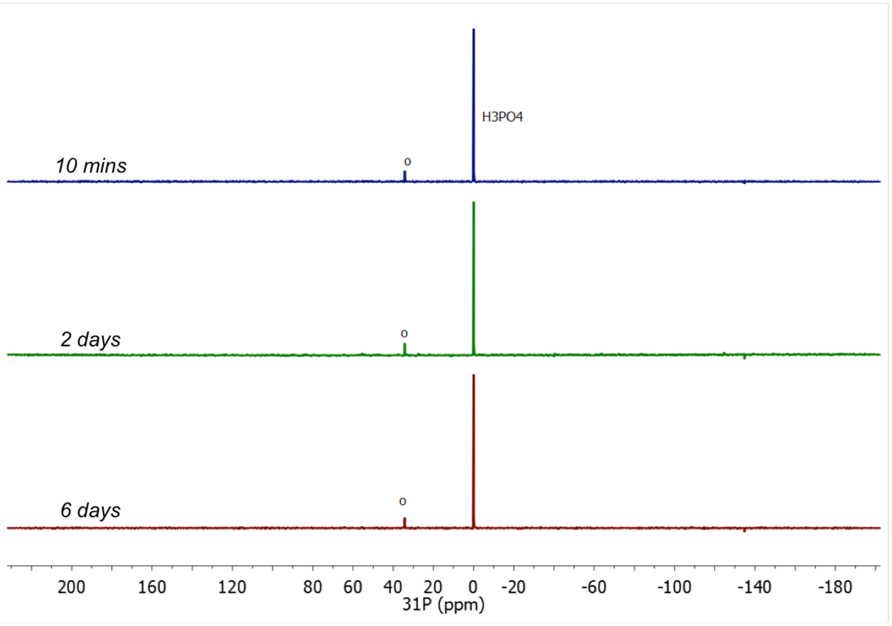

Figure 1.6. $^{31}P\{^1H\}$ NMR spectrum showing stability of nickel hydride **complex 1** (o) in pH 10.4 carbonate buffered H_2O under N_2.

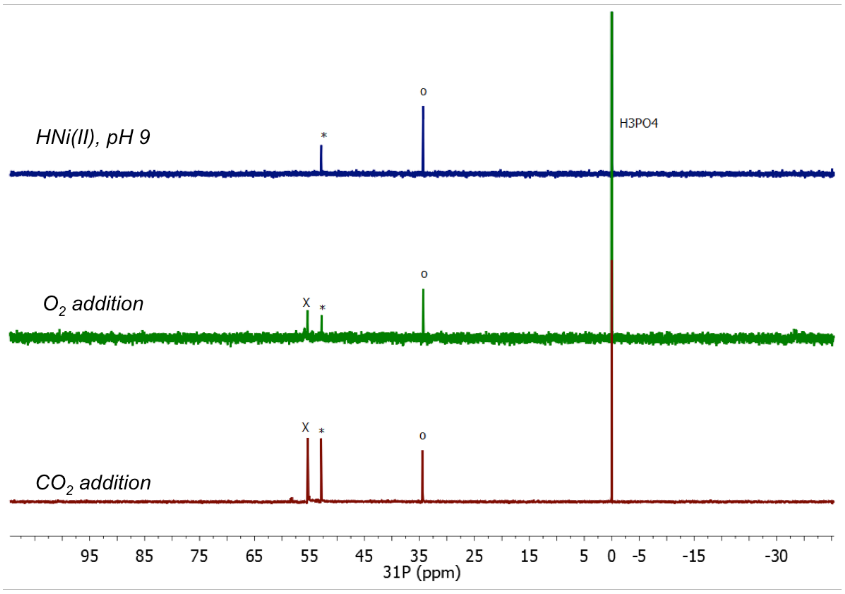

Figure 1.7. $^{31}P\{^1H\}$ NMR spectrum showing nickel hydride complex **1** (o) in pH 9 buffered H_2O under N_2 (top), nickel hydride complex **1** at pH 7 after addition of CO_2 (middle), nickel hydride complex **1** at pH 7 after addition of O_2. Where complex **1** is denoted by (o), complex **2** is denoted by (*), and unidentified decomposition complex is denoted by (X).

1.4 Conclusion

The conversion between CO_2 and formate for fuel generation and utilization in a fuel cell requires catalysts that proceed through transition metal hydride intermediates. Quantification of hydricity values for these intermediates is key to designing catalysts that can be biased towards either CO_2 reduction or formate oxidation. In this study, a simple ligand modification to a nickel bis(diphosphine) complex changes the reactivity from favoring formate oxidation in DMSO, CH_3CN, toward being exergonic for CO_2 reduction in water. This is one of only a few transition metal hydrides known to exhibit solvent-dependent reactivity with CO_2 and formate. However, hydride transfer from $[HNi(TMEPE)_2]^+$ (**1**) to CO_2 at high pH in a carbonate buffer, where the solubility of CO_2 is minimal, appears to be kinetically slow.

Moving to a more hydridic complex would likely lead to higher reaction rates with CO_2 in accordance with the Evans-Bell-Polyani principle, but the constraint of energy efficiency for renewable fuel applications requires the reaction to remain close to thermoneutral, as it currently stands for $[HNi(TMEPE)_2]^+$.[67-68] Therefore, modifications to lower the transition state barrier to improve the kinetics of hydride transfer - without increasing the driving force - is a preferable route for developing energy efficient catalysts. These results demonstrate how hydricity can be tuned through ligand design to impart favorable reactivity for the conversion between CO_2 and formate.

1.5 Experimental Details

General Considerations

All manipulations were carried out using standard Schlenk or glovebox techniques under an atmosphere of dinitrogen. Manipulations involving protic solvents were performed in a separate glovebox than those with non-protic solvents. Solvents were degassed by sparging with argon gas and dried by passage through columns of activated alumina or molecular sieves. Deuterated solvents were purchased from Cambridge Isotopes Laboratories, Inc. and were degassed and stored over activated 3 Å molecular sieves prior to use. Reagents were purchased from commercial vendors and used without further purification unless otherwise noted. $[Ni(MeCN)_6][BF_4]_2$, methyl vinyl ether, and 1,2-bis[bis(methoxyethyl)phosphino]ethane (tmepe) were synthesized according to literature procedures.[60-61, 69]

Physical Methods

NMR Spectroscopy. ^1H, $^{13}C\{^1H\}$, and $^{31}P\{^1H\}$ nuclear magnetic resonance (NMR) spectra were collected at room temperature, unless otherwise noted, on a Bruker AVANCE 400 MHz, 600 MHz or 500 MHz spectrometer. Chemical shifts are reported in δ notation in parts per million (ppm). ^{1}H and ^{13}C spectra were referenced to TMS at 0 ppm via the residual proteo or natural abundance ^{13}C solvent resonances. ^{31}P spectra were referenced to H_3PO_4 at 0 ppm within Xwin-NMR or Bruker's Topspin software, which derives the chemical shifts from the known frequency ratios of the ^{31}P standard to the lock signal of the deuterated solvent. ^{31}P spectra used in determining equilibrium concentration were obtained either with only one pulse or with long delay times (10s) for 3 scans to ensure quantitative integration. Manual shimming, Fourier transformation and automatic spectrum phasing were performed using Xwin-NMR software when using the 400MHz or 500MHz spectrometers. Automatic shimming, Fourier transformation, and automatic spectrum phasing were performed using Bruker's Topspin software on the 600MHZ spectrometer. Spectra were analyzed and figures were generated using MestReNova 6.0.2 software. Peak integrations were calculated within MestReNova.

X-ray Crystallography. The X-ray diffraction study was carried out at the UCI Department of Chemistry X-ray Crystallography Facility on a Bruker SMART APEX II diffractometer. Data were collected at 88 K using Mo Kα radiation (λ = 0.71073 Å). A full sphere of data was collected for the crystal structure. The APEX2[70] program suite was used to determine unit-cell parameters and to collect data. The raw frame data were processed and absorption corrected using the SAINT[71] and SADABS[72] programs, respectively, to yield the reflection data files. Structures were solved by direct methods using SHELXS and refined against F^2 on all data by full-matrix least squares with SHELXTL.[73]All non-hydrogen atoms were refined anisotropically. One methoxyethyl group was found to be disordered and was refined as a two-component disorder using partial site-occupancy factors. Hydrogen atoms were placed at geometrically calculated positions and refined using a riding model, and their isotropic displacement parameters were fixed at 1.2 (1.5 for methyl groups) times the Ueq of the atoms to which they are bonded.

Thermodynamic Measurements. Generation of HNi(II) from H_2 in the presence of base (for water, DMSO, and acetonitrile): Under N_2 atmosphere, $[Ni(tmepe)_2][BF_4]_2$was dissolved in the deuterated solvent of interest in a J. Young NMR tube containing a capillary filled with 0.5M H_3PO_4 in D_2O. One equivalent of base (Et_3N in CD_3CN or DBU in DMSO) was added to the sample to generate the corresponding $[HNi(tmepe)_2][BF_4]$ in equilibrium with $[Ni(tmepe)_2][BF_4]_2$, in water the buffer participated as the base. The sample was freeze-pump-thawed to remove N_2 from both the headspace and dissolved in solution. The J. Young tube was charged with H_2 or CO_2 for 2 minutes then allowed to equilibrate for 2 minutes. This charging process was repeated five times.

The resulting equilibrium was monitored by ^1H, $^{31}P\{^1H\}$ or $^{13}C\{^1H\}$ NMR spectroscopy. The relative integration of complex peaks to the capillary standard was used to monitor the equilibrium of species in solution. Equilibrium was achieved when relative integrations between peaks remained constant for 3 days.

Oxidation of lithium formate. A stock solution of lithium formate was prepared in either H_2O or DMSO-d_6. In a J. Young NMR tube, a solution of **2** was prepared in solvent of interest (10 mM in H_2O, 1.5 mM in CD_3CN or DMSO-d_6). One equivalent of lithium formate solution from stock solution was added stepwise, in water and acetonitrile. Due to insolubility of lithium formate in acetonitrile, the DMSO-d_6 lithium formate stock solution was used in experiment additions for reactions in acetonitrile. The reaction of **2** and lithium formate in each solvent was monitored by ^1H, $^{31}P\{^1H\}$ NMR spectroscopy and relative integrations were compared to an capillary standard containing 0.5M H_3PO_4 in D_2O.

Synthesis.

Synthesis of TMEPE (1,2-bis[di(methoxyethyl)phosphino]ethane). The ligand tmepe was synthesized according to a previously published method with a modified purification procedure.[61] The crude material was dissolved in acetonitrile and filtered through Celite. The filtrate was layered with pentane and chilled at –30 °C for 12 hours, during which a white solid impurity precipitated from solution and was removed by filtration. Removal of solvent under reduced pressure gave tmepe as a viscous yellow oil (63% yield).

Synthesis of $[Ni(TMEPE)_2][BF_4]_2$ (2). A yellow solution of TMEPE (0.110g, 0.338 mmol) in 3 mL of CH_3CN was added dropwise slowly to a stirring blue solution of $[Ni(MeCN)_6][BF_4]_2$ (0.084g, 0.169 mmol) in 3 mL CH_3CN resulting in an immediate color change from blue to dark orange. The solution was stirred at room temperature for 12 hrs. The solution was then filtered through Celite and concentrated under vacuum. The concentrated sample in CH_3CN was layered with Et_2O in the freezer resulting in the precipitation of a white impurity. The solution was removed from the white impurity, concentrated in acetonitrile and layered with Et_2O in the freezer resulting in a dark orange residue. The solution was removed from residue and was triturated with pentane. The sample was dried under vacuum to yield an orange tacky residue. Yield: 0.149g (0.168 mmol, 99% yield). Crystals suitable for X-ray diffraction analysis were grow by slow evaporation of Et_2O into a solution of THF-toluene at room temperature. ESI$^+$ (DCM): 797.21 m/z $\{[Ni(tmepe)_2][BF_4]^+\}$. $^{31}P\{^1H\}$ NMR (CD_3CN) δ 55.03 (s). ^1H NMR (CD_3CN) δ 2.09 (m, 8H, $PC\mathit{H_2}C\mathit{H_2}P$), δ 2.33 (m, 16H, $CH_3OCH_2C\mathit{H_2}P$), δ 3.31 (s, 24H, $C\mathit{H_3}OCH_2CH_2P$), δ 3.67 (m, 16H, $CH_3OC\mathit{H_2}CH_2P$).^{13}C $\{^1H\}$ NMR (CD_3CN) δ 58.5 (8C, $\mathit{C}H_3OCH_2CH_2P$), δ 67.2 (8C, $CH_3O\mathit{C}H_2CH_2P$), δ 25.9 (8C, $CH_3OCH_2\mathit{C}H_2P$), δ 22.6 (4C, $P\mathit{C}H_2\mathit{C}H_2P$).

Synthesis of [Ni(TMEPE)$_2$] (3). A solution of Ni(COD)$_2$ (0.27 mmol,75 mg) in 3 ml of THF was cooled to –35 °C for 5 minutes. Next a cooled solution (–35 °C) of tmepe ligand (0.54 mmol, 178 mg) in 2 mL of THF was added dropwise to the cold and stirring Ni(COD)$_2$ solution. After the addition, the solution color changed from yellow to dark orange-brown. The solution was allowed to stir at room temperature overnight to yield complex **3**. Yield: 182.4 mg (0.259 mmol, 95%yield) ^{31}P{^{1}H}NMR δ 32.2 ($\mathrm{CD_3CN}$) (s). ^{1}H NMR ($\mathrm{CD_3CN}$) δ 1.49 (m, 8H, $\mathrm{PC}\mathit{H}_2\mathrm{C}\mathit{H}_2\mathrm{P}$), δ1.79 (m, 16H, $\mathrm{CH_3OCH_2C}\mathit{H}_2\mathrm{P}$), δ 3.25 (s, 24H, $\mathrm{C}\mathit{H}_3\mathrm{OCH_2CH_2P}$), δ 3.5 (m, 16H, $\mathrm{CH_3OC}\mathit{H}_2\mathrm{CH_2P}$).^{13}C {^{1}H} NMR ($\mathrm{CD_3CN}$) δ 58.3 (8C, $\mathit{C}\mathrm{H_3OCH_2CH_2P}$), δ 71.01 (8C, $\mathrm{CH_3O}\mathit{C}\mathrm{H_2CH_2P}$), δ 33.9 (8C, $\mathrm{CH_3OCH_2}\mathit{C}\mathrm{H_2P}$), δ 23.1 (4C, $\mathrm{P}\mathit{C}\mathrm{H_2}\mathit{C}\mathrm{H_2P}$).

Generation of [HNi(TMEPE)$_2$][BF$_4$] (1). [HNi(TMEPE)$_2$][BF$_4$] was generated *in situ* using two methods for either aprotic or protic solvents. In aprotic solvents, **1** was produced via addition of 1 equivalent of [PhNH$_3$][BF$_4$] to 1 equivalent Ni(TMEPE)$_2$ (**3**) in $\mathrm{CD_3CN}$. The solvent was removed under vacuum, resulting in a light brown residue and re-dissolved in the appropriate solvent (DMSO or H_2O). Under aqueous conditions, water acted as the proton source to generate **1** in solution from **3**. The formation of the hydride was monitored by ^{1}H and ^{31}P NMR spectroscopy for up to 3 days.

^{31}P{^{1}H}NMR δ 36.6 ($\mathrm{CD_3CN}$) (s). ^{1}H NMR ($\mathrm{CD_3CN}$) δ 2.35 (m, 8H, $\mathrm{PC}\mathit{H}_2\mathrm{C}\mathit{H}_2\mathrm{P}$), δ 2.08 (m, 16H, $\mathrm{CH_3OCH_2C}\mathit{H}_2\mathrm{P}$), δ 3.27 (s, 24H, $\mathrm{C}\mathit{H}_3\mathrm{OCH_2CH_2P}$), δ 3.56 (br m, 16H, $\mathrm{CH_3OC}\mathit{H}_2\mathrm{CH_2P}$), δ -14.5 (m, 1H, HNi) ^{13}C {^{1}H} NMR ($\mathrm{CD_3CN}$) δ 58.6 (8C, $\mathit{C}\mathrm{H_3OCH_2CH_2P}$), δ 69.2 (8C, $\mathrm{CH_3O}\mathit{C}\mathrm{H_2CH_2P}$), δ 30.0 (8C, $\mathrm{CH_3OCH_2}\mathit{C}\mathrm{H_2P}$), δ 26.8 (4C, $\mathrm{PCH_2}\mathit{C}\mathrm{H_2P}$).

$^{31}P\{^1H\}$NMR δ 36.8 (DMSO-d$_6$) (s). ^{1}H NMR (DMSO-d$_6$) δ 1.90 (m, 8H, $\mathrm{PC}H_2\mathrm{C}H_2\mathrm{P}$), δ 2.02 (m, 16H, $\mathrm{CH_3OCH_2C}H_2\mathrm{P}$), δ 3.24 (s, 24H, $\mathrm{C}H_3\mathrm{OCH_2CH_2P}$), δ 3.53 (m, 16H, $\mathrm{CH_3OC}H_2\mathrm{CH_2P}$) δ -14.5 (m, 1H, HNi).

$^{31}P\{^1H\}$NMR δ 34.2 (D$_2$O) (s). ^{1}H NMR (D$_2$O) δ 2.03 (m, 8H, $\mathrm{PC}H_2\mathrm{C}H_2\mathrm{P}$), δ 2.14 (m, 16H, $\mathrm{CH_3OCH_2C}H_2\mathrm{P}$), δ 3.51 (s, 24H, $\mathrm{C}H_3\mathrm{OCH_2CH_2P}$), δ 3.70 (m, 16H, $\mathrm{CH_3OC}H_2\mathrm{CH_2P}$).

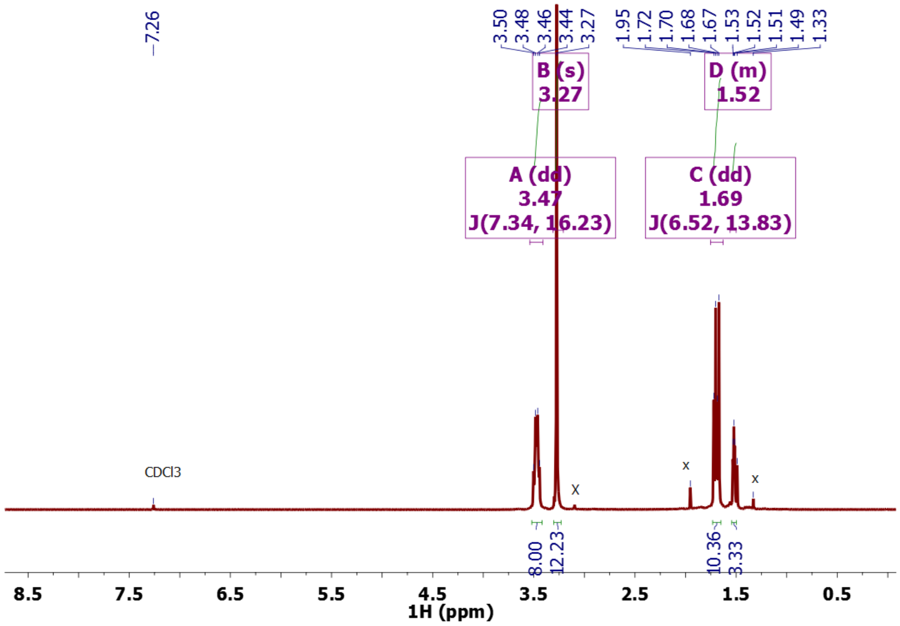

Figure 1.8. ^{1}H NMR spectrum of tmepe ligand (tmepe = 1,2-bis[di(methoxyethyl)phosphino]ethane) in CDCl$_3$ where the black X indicate unknown impurity peaks.

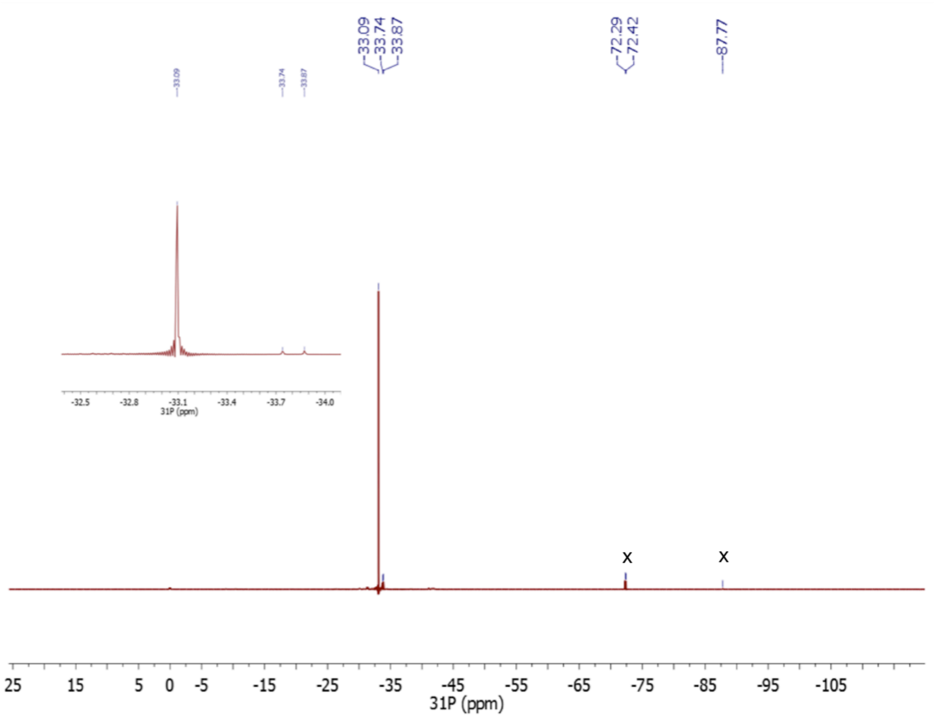

Figure 1.9. $^{31}P\{^{1}H\}$ NMR spectrum of tmepe ligand (tmepe = 1,2-bis[di(methoxyethyl)phosphino]ethane) in $CDCl_3$ where the black X denotes impurity peaks.

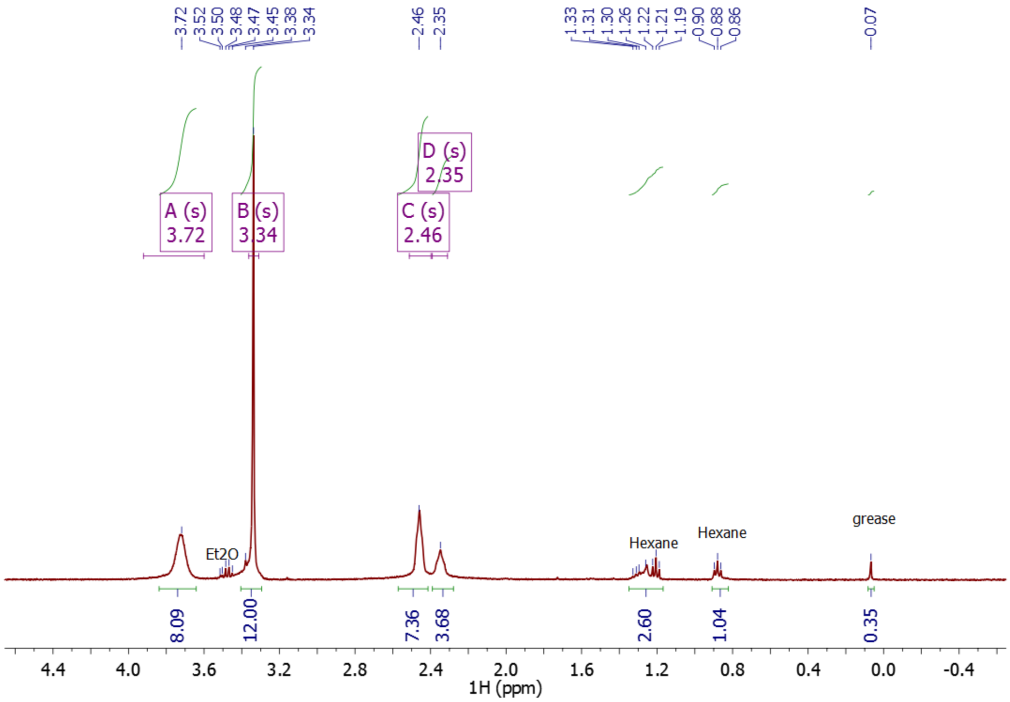

Figure 1.10. ^{1}H NMR spectra of $[Ni(tmepe)_2][BF_4]_2$ in $CDCl_3$.

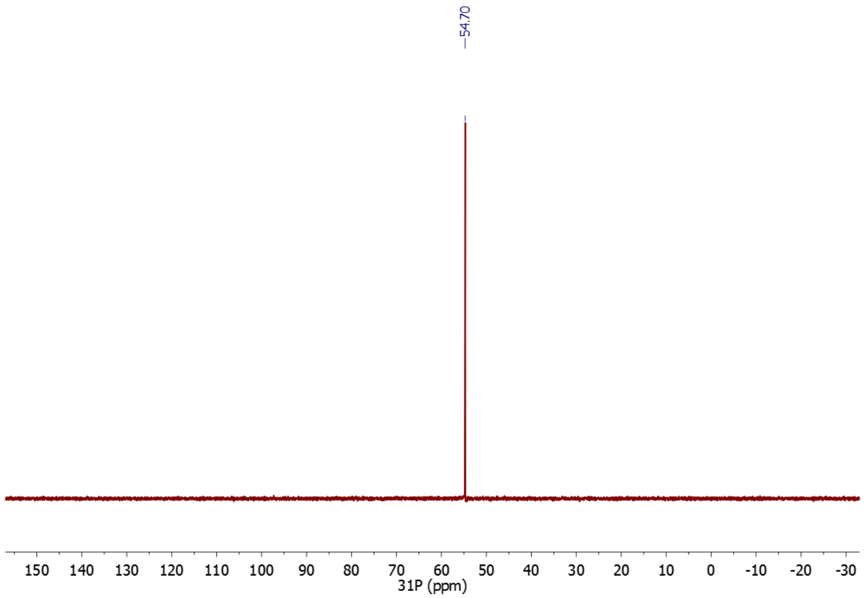

Figure 1.11. $^{31}P\{^1H\}$ NMR spectra of $[Ni(tmepe)_2][BF_4]_2$ in $CDCl_3$.

Characterization of $Ni(tmepe)_2$ (3).

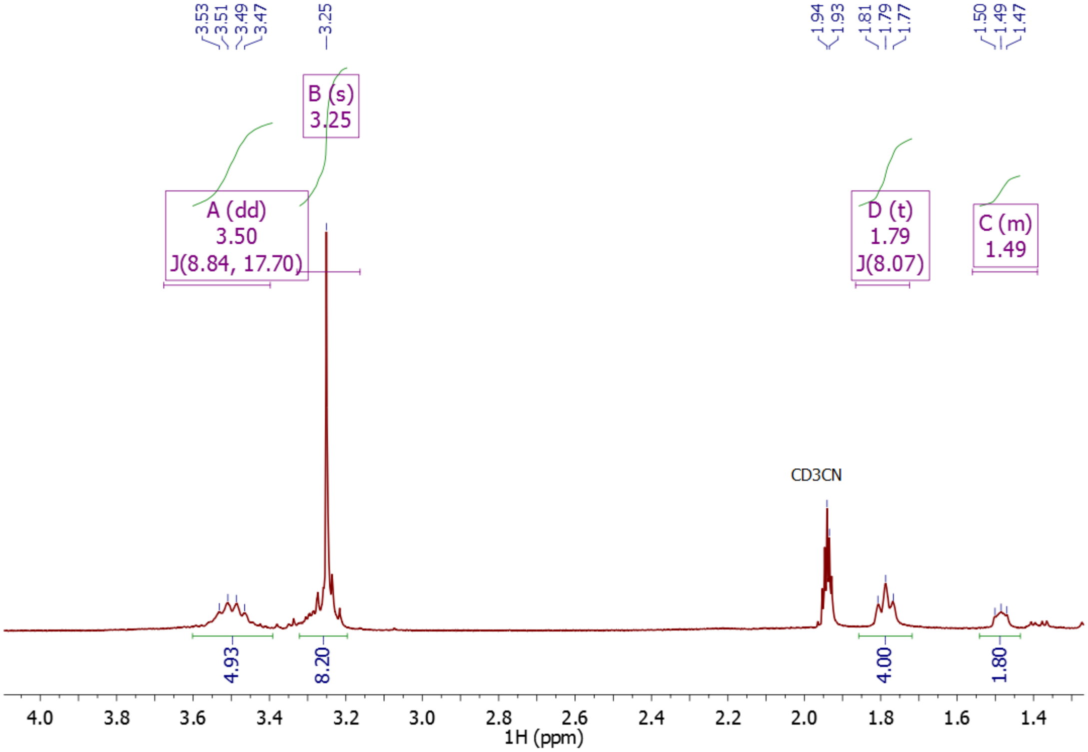

Figure 1.12. ^1H NMR spectrum of $Ni(tmepe)_2$ (**3**) in CD_3CN.

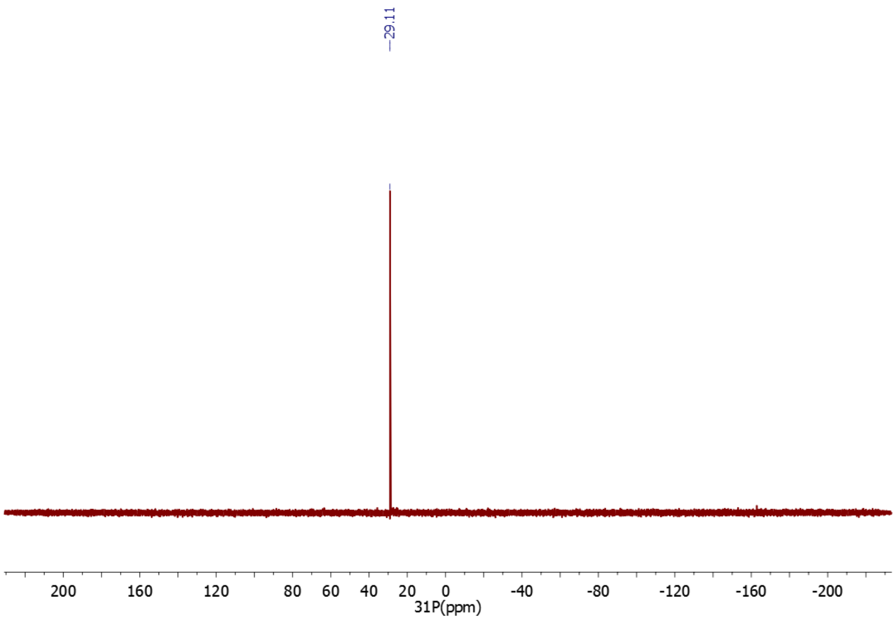

Figure 1.13. $^{31}P\{^1H\}$ NMR spectrum of Ni(tmepe)$_2$ (**3**) in CD_3CN.

Characterization of [HNi(tmepe)$_2$][BF$_4$] (1).

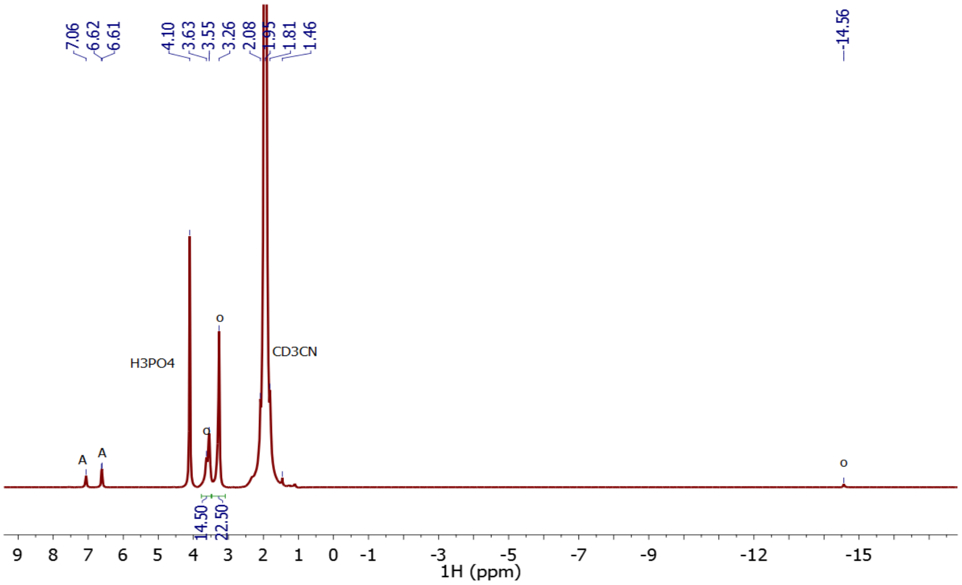

Figure 1.14. ^1H NMR spectrum showing the protonation of one equivalent of the Ni(0) complex **3** by the addition of one equivalent of [PhNH$_4$][BF$_4$] in CD_3CN to yield the nickel hydride complex **1** (o).

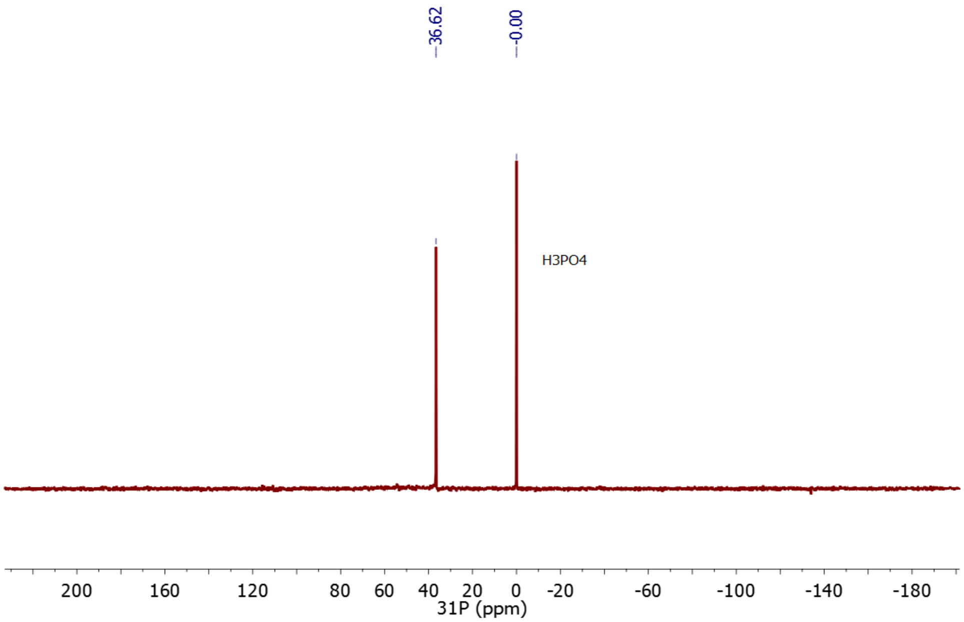

Figure 1.15. $^{31}P\{^{1}H\}$ NMR spectrum showing the protonation of Ni(0) complex **3** to nickel hydride complex **1** in CD_3CN by one equivalent of $[PhNH_4][BF_4]$.

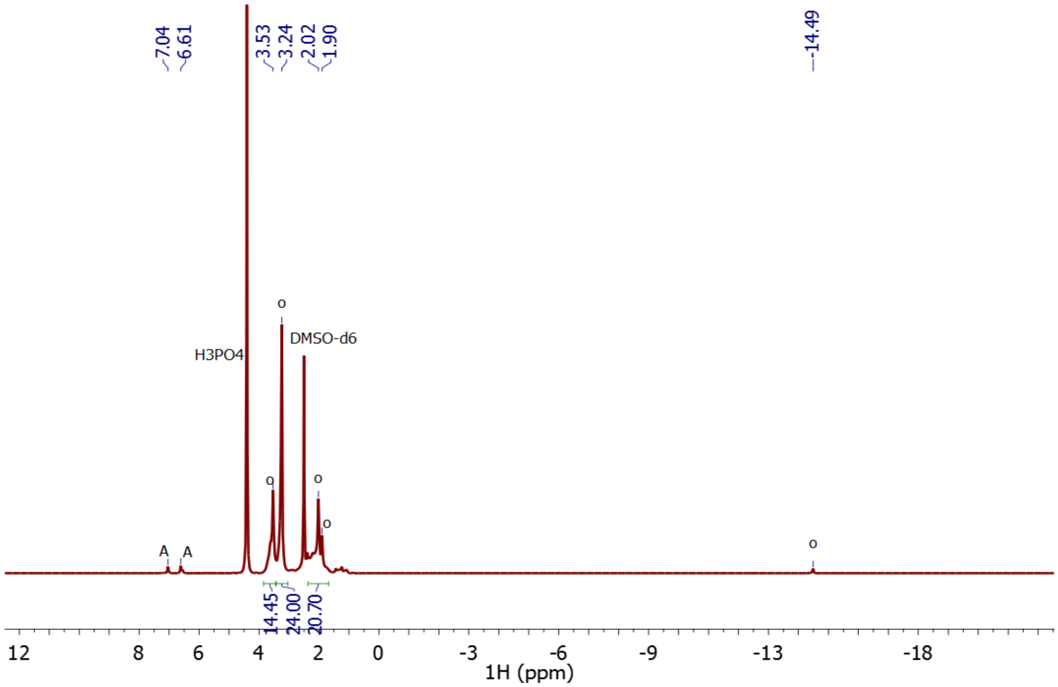

Figure 1.16. ^{1}H NMR spectrum showing the protonation of one equivalent of the Ni(0) complex **3** by the addition of one equivalent of $[PhNH_4][BF_4]$ in DMSO-d_6 to yield the nickel hydride complex **1**(o), where aniline peaks are denoted by A.

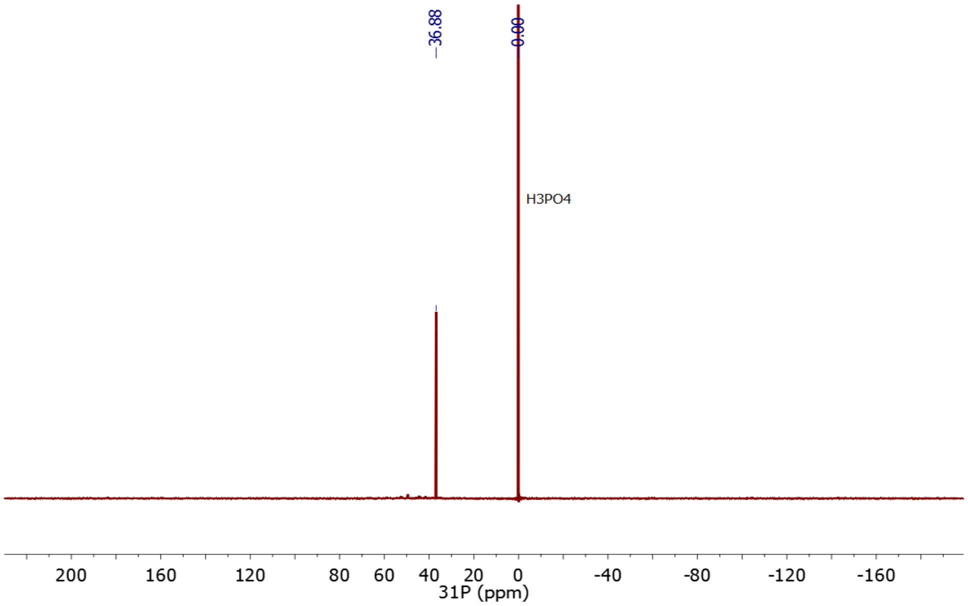

Figure 1.17. $^{31}P\{^1H\}$ NMR spectrum showing the protonation of complex **3** to **1** in DMSO-d_6 by one equivalent of $[PhNH_4][BF_4]$.

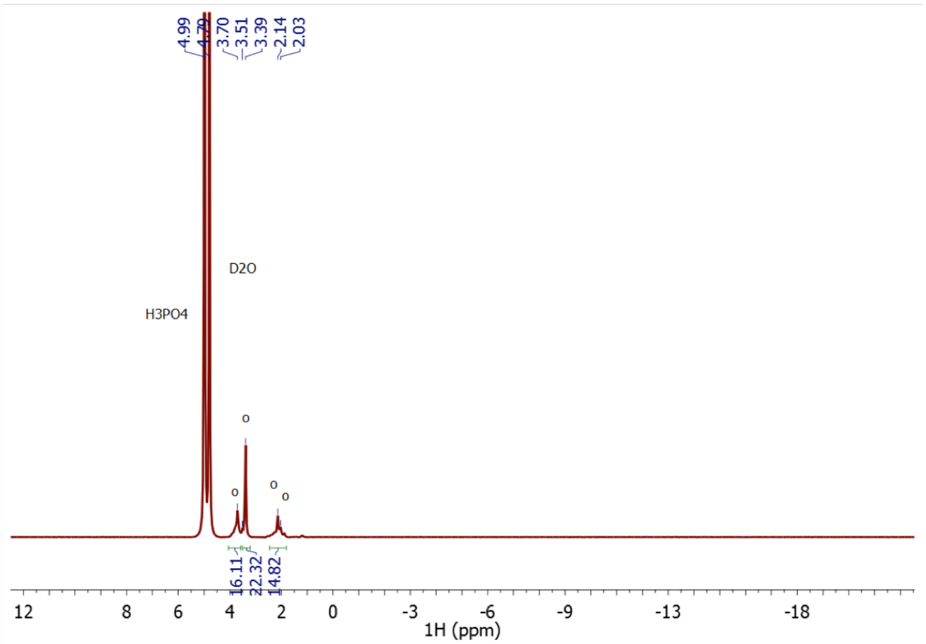

Figure 1.18. ^1H NMR spectrum showing nickel hydride complex **1**(o) in pH 10 carbonate buffered D_2O**.**

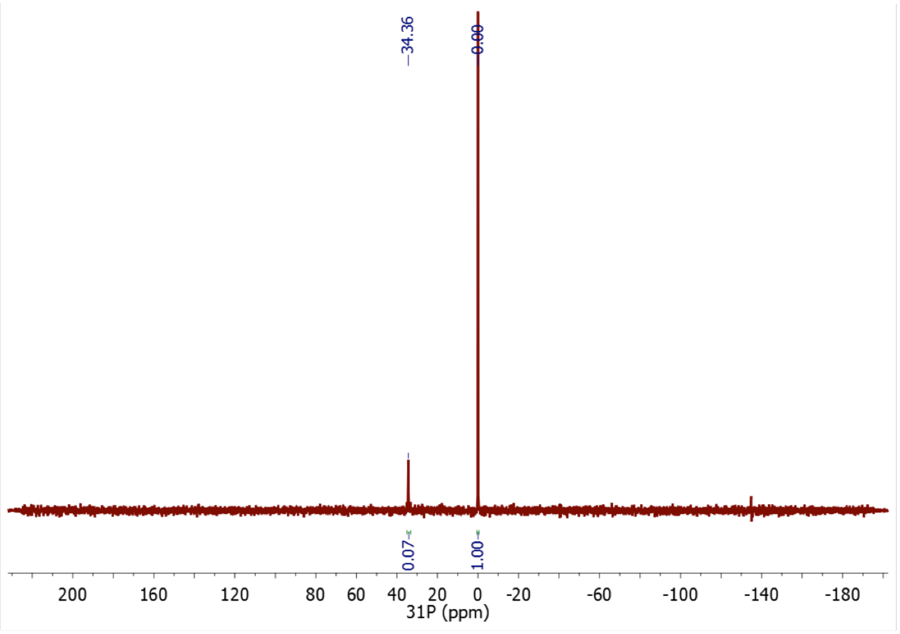

Figure 1.19. $^{31}P\{^1H\}$ NMR spectrum showing nickel hydride complex **1** (o) in pH 10 carbonate buffered D_2O.

1.6 References

1. Wang, W.-H.; Himeda, Y.; Muckerman, J. T.; Manbeck, G. F.; Fujita, E., CO_2 Hydrogenation to Formate and Methanol as an Alternative to Photo- and Electrochemical CO_2 Reduction. *Chem. Rev.* **2015,** *115* (23), 12936-12973.

2. Bernskoetter, W. H.; Hazari, N., Reversible Hydrogenation of Carbon Dioxide to Formic Acid and Methanol: Lewis Acid Enhancement of Base Metal Catalysts. *Accounts Chem. Res.* **2017**.

3. Mellmann, D.; Sponholz, P.; Junge, H.; Beller, M., Formic acid as a hydrogen storage material - development of homogeneous catalysts for selective hydrogen release. *Chem. Soc. Rev.* **2016,** *45* (14), 3954-3988.

4. Appel, A. M.; Bercaw, J. E.; Bocarsly, A. B.; Dobbek, H.; DuBois, D. L.; Dupuis, M.; Ferry, J. G.; Fujita, E.; Hille, R.; Kenis, P. J. A.; Kerfeld, C. A.; Morris, R. H.; Peden, C. H. F.; Portis, A. R.; Ragsdale, S. W.; Rauchfuss, T. B.; Reek, J. N. H.; Seefeldt, L. C.; Thauer, R. K.; Waldrop, G. L., Frontiers, Opportunities, and Challenges in Biochemical and Chemical Catalysis of CO+ Fixation. *Chem. Rev.* **2013,** *113* (8), 6621-6658.

5. Singh, A. K.; Singh, S.; Kumar, A., Hydrogen energy future with formic acid: a renewable chemical hydrogen storage system. *Catal. Sci. Technol.* **2016,** *6* (1), 12-40.

6. Klankermayer, J. r.; Wesselbaum, S.; Beydoun, K.; Leitner, W., Selective Catalytic Synthesis Using the Combination of Carbon Dioxide and Hydrogen: Catalytic Chess at the Interface of Energy and Chemistry. *Angew. Chem. Int. Ed. (English)* **2016,** *55* (26), 7296-7343.

7. Fujita, E.; Muckerman, J. T.; Himeda, Y., Interconversion of CO_2 and formic acid by bio-inspired Ir complexes with pendent bases. *(BBA) - Bioenergetics* **2013,** *1827* (8,Äì9), 1031-1038.

8. Jeletic, M. S.; Mock, M. T.; Appel, A. M.; Linehan, J. C., A Cobalt-Based Catalyst for the Hydrogenation of CO_2 under Ambient Conditions. *J. Am. Chem. Soc.* **2013,** *135* (31), 11533-11536.

9. Spentzos, A. Z.; Barnes, C. L.; Bernskoetter, W. H., Effective Pincer Cobalt Precatalysts for Lewis Acid Assisted CO_2 Hydrogenation. *Inorg. Chem.* **2016,** *55* (16), 8225-8233.

10. Ziebart, C.; Federsel, C.; Anbarasan, P.; Jackstell, R.; Baumann, W.; Spannenberg, A.; Beller, M., Well-Defined Iron Catalyst for Improved Hydrogenation of Carbon Dioxide and Bicarbonate. *J. Am. Chem. Soc.* **2012,** *134* (51), 20701-20704.

11. Langer, R.; Diskin-Posner, Y.; Leitus, G.; Shimon, L. J. W.; Ben-David, Y.; Milstein, D., Low-Pressure Hydrogenation of Carbon Dioxide Catalyzed by an Iron Pincer Complex Exhibiting Noble Metal Activity. *Angew. Chem. Int. Ed. (English)* **2011,** *50* (42), 9948-9952.

12. Schaub, T.; Paciello, R. A., A Process for the Synthesis of Formic Acid by CO_2 Hydrogenation: Thermodynamic Aspects and the Role of CO. *Angew. Chem. Int. Ed. (English)* **2011,** *50* (32), 7278-7282.

13. Huff, C. A.; Sanford, M. S., Catalytic CO_2 Hydrogenation to Formate by a Ruthenium Pincer Complex. *ACS Catal.* **2013,** *3* (10), 2412-2416.

14. Wesselbaum, S.; Hintermair, U.; Leitner, W., Continuous-Flow Hydrogenation of Carbon Dioxide to Pure Formic Acid using an Integrated $scCO_2$ Process with Immobilized Catalyst and Base. *Angew. Chem. Int. Ed. (English)* **2012,** *51* (34), 8585-8588.

15. Federsel, C.; Ziebart, C.; Jackstell, R.; Baumann, W.; Beller, M., Catalytic Hydrogenation of Carbon Dioxide and Bicarbonates with a Well-Defined Cobalt Dihydrogen Complex. *Chem. Eur. J.* **2012,** *18* (1), 72-75.

16. Badiei, Y. M.; Wang, W.-H.; Hull, J. F.; Szalda, D. J.; Muckerman, J. T.; Himeda, Y.; Fujita, E., Cp*Co(III) Catalysts with Proton-Responsive Ligands for Carbon Dioxide Hydrogenation in Aqueous Media. *Inorg. Chem.* **2013,** *52* (21), 12576-12586.

17. Bertini, F.; Gorgas, N.; St√∂ger, B.; Peruzzini, M.; Veiros, L. F.; Kirchner, K.; Gonsalvi, L., Efficient and Mild Carbon Dioxide Hydrogenation to Formate Catalyzed by Fe(II) Hydrido Carbonyl Complexes Bearing 2,6-(Diaminopyridyl)diphosphine Pincer Ligands. *ACS Catal.* **2016,** *6* (5), 2889-2893.

18. Taheri, A.; Berben, L. A., Making C-H bonds with CO2: production of formate by molecular electrocatalysts. *Chem. Commun.* **2016,** *52* (9), 1768-1777.

19. Taheri, A.; Thompson, E. J.; Fettinger, J. C.; Berben, L. A., An Iron Electrocatalyst for Selective Reduction of CO_2 to Formate in Water: Including Thermochemical Insights. *ACS Catal.* **2015,** *5* (12), 7140-7151.

20. Klinkova, A.; Luna, P. D.; Dinh, C.-T.; Voznyy, O.; Larin, E. M.; Kumacheva, E.; Sargent, E. H., Rational Design of Efficient Palladium Catalysts for Electroreduction of Carbon Dioxide to Formate. *ACS Catal.* **2016,** *6* (12), 8115-8120.

21. Zhou, X.; Liu, R.; Sun, K.; Chen, Y.; Verlage, E.; Francis, S. A.; Lewis, N. S.; Xiang, C., Solar-Driven Reduction of 1 atm of CO_2 to Formate at 10% Energy-Conversion Efficiency by Use of a TiO2-Protected III–V Tandem Photoanode in Conjunction with a Bipolar Membrane and a Pd/C Cathode. *ACS Energy Letters* **2016,** *1* (4), 764-770.

22. Min, X.; Kanan, M. W., Pd-Catalyzed Electrohydrogenation of Carbon Dioxide to Formate: High Mass Activity at Low Overpotential and Identification of the Deactivation Pathway. *J. Am. Chem. Soc.* **2015,** *137* (14), 4701-4708.

23. Lee, S. Y.; Lim, S. Y.; Seo, D.; Lee, J.-Y.; Chung, T. D., Light-Driven Highly Selective Conversion of CO_2 to Formate by Electrosynthesized Enzyme/Cofactor Thin Film Electrode. *Adv. Energy Mater.* **2016,** *6* (11), 1502207-n/a.

24. Sreekanth, N.; Phani, K. L., Selective reduction of CO_2 to formate through bicarbonate reduction on metal electrodes: new insights gained from SG/TC mode of SECM. *Chem. Commun.* **2014,** *50* (76), 11143-11146.

25. Kang, P.; Zhang, S.; Meyer, T. J.; Brookhart, M., Rapid Selective Electrocatalytic Reduction of Carbon Dioxide to Formate by an Iridium Pincer Catalyst Immobilized on Carbon Nanotube Electrodes. *Angew. Chem. Int. Ed. (English)* **2014,** *53* (33), 8709-8713.

26. Zhang, S.; Kang, P.; Meyer, T. J., Nanostructured Tin Catalysts for Selective Electrochemical Reduction of Carbon Dioxide to Formate. *J. Am. Chem. Soc.* **2014,** *136* (5), 1734-1737.

27. Kang, P.; Meyer, T. J.; Brookhart, M., Selective electrocatalytic reduction of carbon dioxide to formate by a water-soluble iridium pincer catalyst. *Chem. Sci.* **2013,** *4* (9), 3497-3502.

28. Narayanan, S. R.; Haines, B.; Soler, J.; Valdez, T. I., Electrochemical Conversion of Carbon Dioxide to Formate in Alkaline Polymer Electrolyte Membrane Cells. *J. Electrochem. Soc.* **2011,** *158* (2), A167-A173.

29. Kang, P.; Cheng, C.; Chen, Z.; Schauer, C. K.; Meyer, T. J.; Brookhart, M., Selective Electrocatalytic Reduction of CO_2 to Formate by Water-Stable Iridium Dihydride Pincer Complexes. *J. Am. Chem. Soc.* **2012,** *134* (12), 5500-5503.

30. Myers, T. W.; Berben, L. A., Aluminium-ligand cooperation promotes selective dehydrogenation of formic acid to H_2 and CO_2. *Chem. Sci.* **2014,** *5* (7), 2771-2777.

31. Boddien, A.; Loges, B. r.; G√§rtner, F.; Torborg, C.; Fumino, K.; Junge, H.; Ludwig, R.; Beller, M., Iron-Catalyzed Hydrogen Production from Formic Acid. *J. Am. Chem. Soc.* **2010,** *132* (26), 8924-8934.

32. Boddien, A.; Mellmann, D. r.; G√§rtner, F.; Jackstell, R.; Junge, H.; Dyson, P. J.; Laurenczy, G. b.; Ludwig, R.; Beller, M., Efficient Dehydrogenation of Formic Acid Using an Iron Catalyst. *Science* **2011,** *333* (6050), 1733-1736.

33. Celaje, J. J. A.; Lu, Z.; Kedzie, E. A.; Terrile, N. J.; Lo, J. N.; Williams, T. J., A prolific catalyst for dehydrogenation of neat formic acid. *Nat. Commun.* **2016,** *7*, 11308.

34. Mellone, I.; Gorgas, N.; Bertini, F.; Peruzzini, M.; Kirchner, K.; Gonsalvi, L., Selective Formic Acid Dehydrogenation Catalyzed by Fe-PNP Pincer Complexes Based on the 2,6-Diaminopyridine Scaffold. *Organometallics* **2016,** *35* (19), 3344-3349.

35. Bertini, F.; Mellone, I.; Ienco, A.; Peruzzini, M.; Gonsalvi, L., Iron(II) Complexes of the Linear rac-Tetraphos-1 Ligand as Efficient Homogeneous Catalysts for Sodium Bicarbonate Hydrogenation and Formic Acid Dehydrogenation. *ACS Catal.* **2015,** *5* (2), 1254-1265.

36. Zell, T.; Butschke, B.; Ben-David, Y.; Milstein, D., Efficient Hydrogen Liberation from Formic Acid Catalyzed by a Well-Defined Iron Pincer Complex under Mild Conditions. *Chem. Eur. J.* **2013,** *19* (25), 8068-8072.

37. Bielinski, E. A.; Lagaditis, P. O.; Zhang, Y.; Mercado, B. Q.; W√ºrtele, C.; Bernskoetter, W. H.; Hazari, N.; Schneider, S., Lewis Acid-Assisted Formic Acid Dehydrogenation Using a Pincer-Supported Iron Catalyst. *J. Am. Chem. Soc.* **2014,** *136* (29), 10234-10237.

38. An, L.; Chen, R., Direct formate fuel cells: A review. *J. Power Sources* **2016,** *320*, 127-139.

39. Mao, H.; Huang, T.; Yu, A., Electrochemical surface modification on CuPdAu/C with extraordinary behavior toward formic acid/formate oxidation. *Int. J. Hydrogen Energy* **2016,** *41* (30), 13190-13196.

40. Sakai, K.; Kitazumi, Y.; Shirai, O.; Kano, K., Bioelectrocatalytic formate oxidation and carbon dioxide reduction at high current density and low overpotential with tungsten-containing formate dehydrogenase and mediators. *Electrochem Commun.* **2016,** *65*, 31-34.

41. Seu, C. S.; Appel, A. M.; Doud, M. D.; DuBois, D. L.; Kubiak, C. P., Formate oxidation via [small beta]-deprotonation in [Ni(PR2NR[prime or minute]2)2(CH3CN)]2+ complexes. *Energ. Environ. Sci.* **2012,** *5* (4), 6480-6490.

42. Galan, B. R.; Sch√∂ffel, J.; Linehan, J. C.; Seu, C.; Appel, A. M.; Roberts, J. A. S.; Helm, M. L.; Kilgore, U. J.; Yang, J. Y.; DuBois, D. L.; Kubiak, C. P., Electrocatalytic Oxidation of Formate by [Ni(PR2NR‚Ä≤2)2(CH3CN)]2+ Complexes. *J. Am. Chem. Soc.* **2011,** *133* (32), 12767-12779.

43. Li, Y.; Feng, Y.; Sun, X.; He, Y., A Sodium-Ion-Conducting Direct Formate Fuel Cell: Generating Electricity and Producing Base. *Angew. Chem. Int. Ed. (English)* **2017**, n/a-n/a.

44. Tsay, C.; Livesay, B. N.; Ruelas, S.; Yang, J. Y., Solvation Effects on Transition Metal Hydricity. *J. Am. Chem. Soc.* **2015,** *137* (44), 14114-14121.

45. Connelly, S. J.; Wiedner, E. S.; Appel, A. M., Predicting the reactivity of hydride donors in water: thermodynamic constants for hydrogen. *Dalton Trans.* **2015,** *44* (13), 5933-5938.

46. Moret, S. v.; Dyson, P. J.; Laurenczy, G. b., Direct synthesis of formic acid from carbon dioxide by hydrogenation in acidic media. *Nat. Commun.* **2014,** *5*, 4017.

47. DuBois, D. L.; Berning, D. E., Hydricity of transition-metal hydrides and its role in CO_2 reduction. *Appl. Organomet. Chem.* **2000,** *14* (12), 860-862.

48. Wiedner, E. S.; Chambers, M. B.; Pitman, C. L.; Bullock, R. M.; Miller, A. J. M.; Appel, A. M., Thermodynamic Hydricity of Transition Metal Hydrides. *Chem. Rev.* **2016,** *116* (15), 8655-8692.

49. Lilio, A. M.; Reineke, M. H.; Moore, C. E.; Rheingold, A. L.; Takase, M. K.; Kubiak, C. P., Incorporation of Pendant Bases into Rh(diphosphine)2 Complexes: Synthesis, Thermodynamic Studies, And Catalytic CO_2 Hydrogenation Activity of [Rh(P2N2)2]+ Complexes. *J. Am. Chem. Soc.* **2015,** *137* (25), 8251-8260.

50. Estes, D. P.; Vannucci, A. K.; Hall, A. R.; Lichtenberger, D. L.; Norton, J. R., Thermodynamics of the Metal,ÄìHydrogen Bonds in (Œ∑5-C5H5)M(CO)2H (M = Fe, Ru, Os). *Organometallics* **2011,** *30* (12), 3444-3447.

51. Rakowski Dubois, M.; Dubois, D. L., Development of Molecular Electrocatalysts for CO_2 Reduction and H_2 Production/Oxidation. *Acc. Chem. Res.* **2009,** *42* (12), 1974-1982.

52. Creutz, C.; Chou, M. H., Rapid Transfer of Hydride Ion from a Ruthenium Complex to C1 Species in Water. *J. Am. Chem. Soc.* **2007,** *129* (33), 10108-10109.

53. Creutz, C.; Chou, M. H., Hydricities of d6 Metal Hydride Complexes in Water. *J. Am. Chem. Soc.* **2009,** *131* (8), 2794-2795.

54. Matsubara, Y.; Fujita, E.; Doherty, M. D.; Muckerman, J. T.; Creutz, C., Thermodynamic and Kinetic Hydricity of Ruthenium(II) Hydride Complexes. *J. Am. Chem. Soc.* **2012,** *134* (38), 15743-15757.

55. Brereton, K. R.; Pitman, C. L.; Cundari, T. R.; Miller, A. J. M., Solvent-Dependent Thermochemistry of an Iridium/Ruthenium H_2 Evolution Catalyst. *Inorg. Chem.* **2016,** *55* (22), 12042-12051.

56. Pitman, C. L.; Brereton, K. R.; Miller, A. J. M., Aqueous Hydricity of Late Metal Catalysts as a Continuum Tuned by Ligands and the Medium. *J. Am. Chem. Soc.* **2016,** *138* (7), 2252-2260.

57. Tsay, C.; Yang, J. Y., Electrocatalytic Hydrogen Evolution under Acidic Aqueous Conditions and Mechanistic Studies of a Highly Stable Molecular Catalyst. *J. Am. Chem. Soc.* **2016,** *138* (43), 14174-14177.

58. Levina, V. A.; Filippov, O. A.; Gutsul, E. I.; Belkova, N. V.; Epstein, L. M.; Lledos, A.; Shubina, E. S., Neutral Transition Metal Hydrides as Acids in Hydrogen Bonding and Proton Transfer: Media Polarity and Specific Solvation Effects. *J. Am. Chem. Soc.* **2010,** *132* (32), 11234-11246.

59. Connelly Robinson, S. J.; Zall, C. M.; Miller, D. L.; Linehan, J. C.; Appel, A. M., Solvent influence on the thermodynamics for hydride transfer from bis(diphosphine) complexes of nickel. *Dalton Trans.* **2016,** *45* (24), 10017-10023.

60. K. Ospay, J. D., K. M. Nsunda, E. Roli, R. Houriet, and L. Hevesi, Experimental and Theoretical Studies of the Gas-Phase Protonation of Vinyl Ethers, Vinyl Sulfide, and Vinyl Selenides. *J. Am. Chem. Soc.* **1989,** *111* (14), 5028-5036.

61. Deutsch, A. H. a. E. A., 1,2-Bis[bis(methoxyethyl)phosphino]ethane, 1,2-bis[bis(methoxypropyl)ohosphino]ethane and their quarternary salts. Unexpected hydroltyic susceptibility of the ethanediylbis[bis(methoxyethyl)phosphonium]-PH,P' H' cation. *J. Organomet. Chem.* **1993,** *460*, 19-23.

62. Wayner, D. D. M.; Parker, V. D., Bond energies in solution from electrode potentials and thermochemical cycles. A simplified and general approach. *Acc. Chem. Res.* **1993,** *26* (5), 287-294.

63. Kaljurand, I.; Kütt, A.; Sooväli, L.; Rodima, T.; Mäemets, V.; Leito, I.; Koppel, I. A., Extension of the Self-Consistent Spectrophotometric Basicity Scale in Acetonitrile to a Full Span of 28 pKa Units: Unification of Different Basicity Scales. *J. Org. Chem.* **2005,** *70* (3), 1019-1028.

64. Tsutomu Ishikawa, Y. K., Hiyoshizo Kotsuki, Takuya Kumamoto, Davor Margetic, Kazuo Nagasawa, Waka Nakanishi, Superbases for Organic Synthesis: Guanidines, Amidines, Phosphazenes and Related Organocatalyts. Ishikawa, T., Ed. John Wiley & Sons, Ltd.: The Atrium, Southern Gate, Chichester, West Sussex, Po19 8SQ, United Kingdom, 2009.

65. Burgess, S. A.; Kendall, A. J.; Tyler, D. R.; Linehan, J. C.; Appel, A. M., Hydrogenation of CO_2 in Water Using a Bis(diphosphine) Ni–H Complex. *ACS Catal.* **2017,** *7* (4), 3089-3096.

66. Burgess, S. A.; Appel, A. M.; Linehan, J. C.; Wiedner, E. S., Changing the Mechanism for CO_2 Hydrogenation Using Solvent-Dependent Thermodynamics. *Angewandte Chemie* **2017,** *129* (47), 15198-15201.

67. Armstrong, F. A.; Hirst, J., Reversibility and efficiency in electrocatalytic energy conversion and lessons from enzymes. *Proceedings of the National Academy of Sciences* **2011,** *108* (34), 14049-14054.

68. Smith, S. E.; Yang, J. Y.; DuBois, D. L.; Bullock, R. M., Reversible Electrocatalytic Production and Oxidation of Hydrogen at Low Overpotentials by a Functional Hydrogenase Mimic. *Angew. Chem. Int. Ed. (English)* **2012,** *51* (13), 3152-3155.

69. Hathaway, B. J.; Holah, D. G.; Underhill, A. E., 468. The preparation and properties of some bivalent transition-metal tetrafluoroborate-methyl cyanide complexes. *J. Chem. Soc. (Resumed)* **1962,** (0), 2444-2448.

70. *APEX2*, Version 2014.11-0; Bruker AXS, Inc.; Madison, WI 2014.

71. *SAINT*, Version 8.34a; Bruker AXS, Inc.; Madison, WI 2013.

72. Sheldrick *G. M. SADABS*, Version 2014/5; Bruker AXS, Inc.; Madison, WI 2014.

73. Sheldrick *G. M. SHELXTL*, Version 2014/7; Bruker AXS, Inc.; Madison, WI 2014.

CHAPTER 2

Selective CO_2 Reduction at $[HPt(dmpe)_2]^+$ through Thermodynamic and Kinetic Control

Portions of this chapter have been published:
Ceballos, B. M.; Yang, J. Y., *Proc. Natl. Acad. Sci. USA*, **2018**, *115* (50), 12686 - 12691.
Ceballos, B. M.; Yang, J. Y., *Organometallics, 2019, accepted.* .

2.1 Motivations and Specific Aims

Thermodynamic relationships that describe the reactivity of metal hydrides with H^+ and CO_2 were utilized to generate a modified Pourbaix diagram which outlines product favorability as a function of proton activity and hydricity (ΔG_{H^-}), or hydride donor strength. The diagram describes a region of metal hydricity and proton activity in which CO_2 reduction is favorable and H^+ reduction is suppressed. This diagram was used to select $[Pt(dmpe)_2](PF_6)_2$ (dmpe = 1,2-bis(dimethylphosphino)ethane) as a potential catalyst because the corresponding hydride $[HPt(dmpe)_2]^+$ has the correct hydricity to access the region where selective CO_2 reduction is possible. The selective catalytic activity of $[Pt(dmpe)_2](PF_6)_2$ toward CO_2 reduction is reported. The kinetic and thermodynamic factors that result in the observed catalytic selectivity are investigated by measuring relative rates of electron transfer and chemical steps using electrochemical and spectroscopic techniques. The thermodynamic and kinetic analysis of the catalytic selectivity of $[Pt(dmpe)_2](PF_6)_2$ illustrates the value of using thermodynamic product diagrams to guide selective and efficient catalyst discovery.

2.2 Background

Applying renewable electricity to reduce CO_2 through formation of energy-rich C-H bonds is a central goal for the generation of sustainable fuels.[2-4] However, low product selectivity (or Faradaic yield) is often the result of parasitic H_2 evolution or the generation of a mixture of carbon-based products.[5-6] Unselective reduction ultimately stems from competitive reactions between CO_2 and H^+ with intermediates in the catalytic cycle. Thus, orchestrating the sequence of catalyst reactivity with CO_2 and H^+ is essential to achieving high selectivity.

In order to understand the factors that determine selectivity between CO_2 and H^+ reduction, the reactivity of metal hydrides was investigated. Selectivity for formate is a particularly difficult challenge because metal hydride intermediates are common to both reaction pathways (Scheme 2.1). As a result, very few heterogeneous[7-9] or homogeneous[10-13] catalysts have been reported with high (>90%) Faradaic efficiency for formate production.

Understanding the reactivity of metal hydrides is key to controlling the divergent reaction pathways that ultimately determine selectivity. Electrochemical generation of competent intermediates for catalysis at a metal hydride requires a series of electron transfer, protonation, and hydride transfer steps (Scheme 2.1). Thermodynamic relationships can be used to describe the stability of metal hydrides in the presence of protons as well as define the thermodynamic requirements necessary to reduce CO_2 to formate.[11, 14-23] The reactivity of a metal hydride toward H^+ or CO_2 can be assessed using the thermodynamic cycles for H_2 evolution or CO_2 reduction (Scheme 2.3).

In the case of H_2 evolution, there are two significant factors that describe overall thermodynamic reactivity (a) metal hydricity value (ΔG_{H^-}) and (b) solution acidity (pK_a) (Scheme 2.3; a). The first requirement can be satisfied by comparing hydricity values of the hydride donor to H_2 in the appropriate solvent. This comparison is useful for predicting reactivity

Scheme 2.1. Proposed catalytic cycle for H^+ and CO_2 reduction at a metal hydride $[HML_2]^n$.

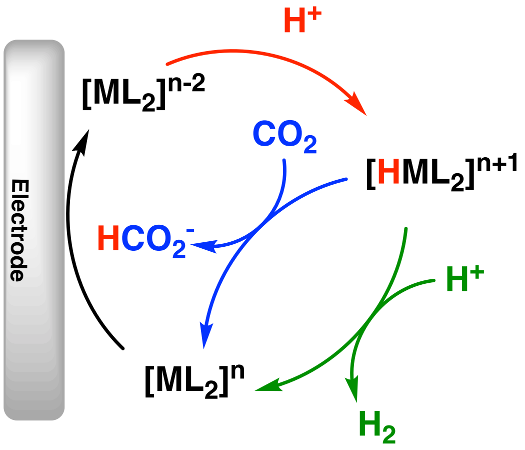

as well as quantifying the expected reaction driving force for H^+ reduction. Since hydricity values have been measured for many classes of compounds, they can be predictably tuned through metal and ligand framework design.[24] Second, solution acidity (or pK_a of the proton source) is significant because the acid source must be sufficiently acidic to both generate a metal hydride at a reduced metal center and subsequently accept a hydride to generate H_2.

In contrast, the thermodynamic cycle of CO_2 reduction at a metal hydride (Scheme 2.3; b) is independent of solution acidity. Although solution acidity is an important factor to consider for metal hydride formation via protonation it does not contribute to the overall free energy of the reaction for CO_2 reduction to formate (ΔG_{HCO2-}). Instead, solution acidity can direct the CO_2 reduction product to the 2 e^-, 2 H^+ formic acid (H_2CO_2) or the 2 e^-,1 H^+ deprotonated formate (HCO_2^-) product by inhibiting H_2 evolution.

Gaining a complete understanding of the reactivity of metal hydrides is crucial for improving catalyst design. In Chapter 2.2.1, the thermodynamic and kinetic intersection of both of these reduction reactions on product selectivity at a metal hydride is explored. Chapter 2.2.2 describes use of the thermodynamic cycles (Scheme 2.3) to identify a metal hydride $[HPt(dmpe)_2]^+$ with an appropriate hydricity to access conditions in which selective CO_2 reduction to formate is favorable. In Chapter 2.2.3, I demonstrate the resting state, $[Pt(dmpe)_2](PF_6)_2$, is an electrocatalysts for CO_2 reduction to formate with high Faradaic efficiency with negligible H_2 evolution when using an acid with the appropriate pK_a that ‘turns off’ the hydrogen evolution pathway. $[Pt(dmpe)_2]^{2+}$ joins the iron carbonyl cluster reported by Berben et al.,[15, 25-26] an iridium complex reported by Brookhart and Meyer et al.,[12, 27-28] and a cobalt complex reported by Artero et al.[11] as rare examples of molecular electrocatalysts that can reduce CO_2 to HCO_2^- with Faradaic efficiencies of greater than 90%.

In addition to a thermochemical understanding of metal hydride reactivity, reaction kinetics also have critical consequences on product selectivity and overall catalyst efficiency. Previous studies by our group[22, 29] and others[30-33] have highlighted the importance of considering reaction kinetics alongside thermodynamic requirements for catalyst development. I delved further into the mechanistic and kinetic details of catalytic CO_2 reduction by $[Pt(dmpe)_2](PF_6)_2$ (**1**). The proposed catalytic cycle is outlined in Scheme 2.1, along with potential off-cycle HER reactions at a metal hydride intermediate. The mechanistic studies were enabled by the facile isolation and characteristic ^{31}P NMR signatures of the proposed intermediates $[Pt(dmpe)_2]$ (**2**) and $[HPt(dmpe)_2]^+$ (**3**) to investigate stepwise reactivity. Cyclic voltammetry was used to determine the electron transfer kinetics (Chapter 2.2.4) and the reactivity of the proposed intermediates with either H+ or CO_2 (Chapter 2.2.5-2.2.6). The energy landscape outlined by the mechanistic studies is described in Chapter 2.2.7. Finally, the general applicability of the thermodynamic product diagrams for catalyst discovery is discussed in Chapter 2.2.8.

2.3 Results and Discussion

2.3.1 Constructing Thermodynamic Product Diagrams

Thermodynamic cycles for H_2 evolution and CO_2 reduction have been useful in identifying active catalysts. In order to investigate the metal hydricity-pK_a relationship a modified Pourbaix diagram is used (Scheme 2.2). In this diagram, thermodynamic products are specified with respect to hydricity instead of redox potential. Using hydricity instead of redox potential results in a diagram that details the thermodynamically anticipated product distribution and provides a

Scheme 2.2. Thermodynamic Product Diagrams for H^+ or CO_2 Reduction Reactions at a Metal Hydride in Acetonitrile.

(a) **Heterolytic H_2 Bond Formation**

(1) $[HML]^+ \rightleftharpoons [ML]^{2+} + H^-$ $\quad \Delta G_{H^-}$

(2) $HB \rightleftharpoons H^+ + B^-$ $\quad 1.37{*}pK_a$

(3) $H^+ + H^- \rightleftharpoons H_2$ $\quad$ **- 77 kcal/mol**

---

(4) $[HML]^+ + HB \rightleftharpoons [ML]^{2+} + H_2$ $\quad \Delta G_{H2}$

$$\Delta G_{H_2} = \Delta G_{H^-} + 1.37{*}pK_a - 77 \text{ kcal/mol}$$

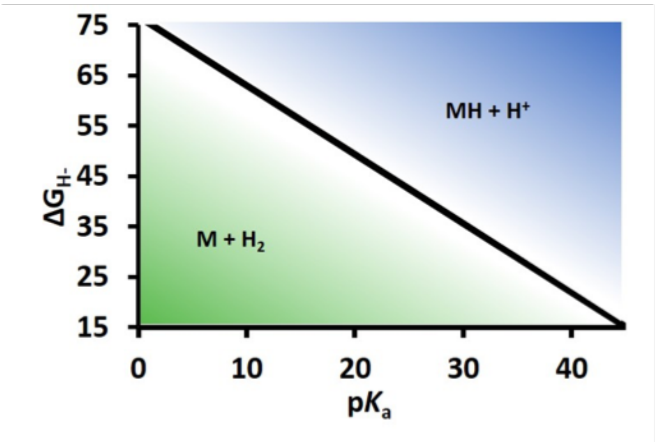

(b) **Free Energy of CO_2 Reduction to HCO_2^- via H^- Transfer**

(1) $[HML]^+ \rightleftharpoons [ML]^{2+} + H^-$ $\quad \Delta G_{H^-}$

(5) $H^- + CO_2 \rightleftharpoons HCO_2^-$ $\quad -\Delta G_{H^-}(HCO_2^-)$

---

(6) $[HML]^+ + CO_2 \rightleftharpoons [ML]^{2+} + HCO_2^-$ $\quad \Delta G_{HCO2-}$

$$\Delta G_{HCO2-} = (\Delta G_{H^-}) - \Delta G_{H^-}(HCO_2^-)$$

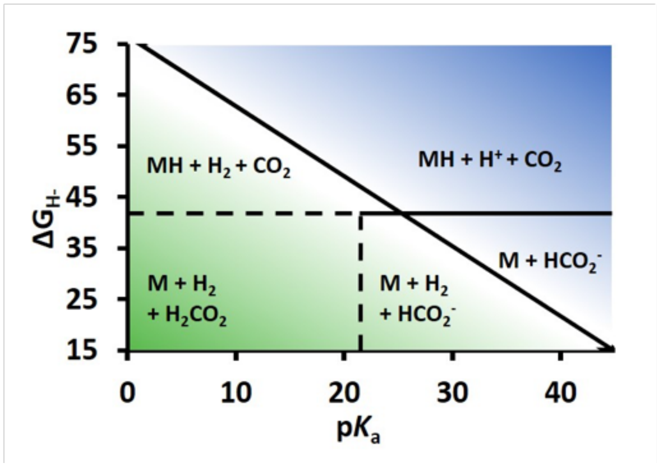

more instructive guideline for targeting the discovery of selective reduction catalysts.

The relationship between pK_a, hydricity, and H_2 evolution in acetonitrile is quantitatively depicted in Scheme 2.2 (a). The thermodynamic cycles describing the free energy for the reaction of a metal hydride towards H^+ to evolve H_2 is shown in Scheme 2.2 (a). The free energy of H_2 evolution (eq 4) is dependent on the hydricity, pK_a of the acid, and the heterolytic bond forming energy of H_2, which is 77 kcal/mol in acetonitrile.[24] The gray line differentiates the boundary where the free energy of H_2 evolution at a metal hydride (eq 4) in Scheme 2.2 (ΔG_{H2}) equals zero and $MH/H^+/H_2$ exist in equilibrium, analogous to lines in a Pourbaix diagram. Protonation to evolve hydrogen is exergonic for hydride complexes of a given hydricity under conditions below the gray line (green zone), and endergonic above the line (blue zone).

The thermodynamic requirement for reduction of CO_2 to formate, a net hydride transfer, is also dictated by the hydricity (ΔG_{H-}) of the donor as shown in eq 6 (Scheme 2.2, b). Transition metal hydricity values lower than that of formate will result in exergonic hydride transfer to CO_2. This information can be mapped onto the thermodynamic diagram illustrating metal hydride reactivity with protons (Scheme 2.2, b). The thermodynamic product distribution that results from a stoichiometric mixtures of metal hydride and acid of specific pK_a values under 1 atm of CO_2 is described in this diagram. The pK_a of formic acid is estimated to be ~20.9 in acetonitrile;[37] therefore it is expected to be protonated at lower pK_a values.

In Scheme 2.3 (b), a region is defined where specific metal hydricity and pK_a combinations will result in which selective reduction of CO_2 to formate without concomitant H_2 evolution. The challenge of selective CO_2 reduction is often introduced by comparing the thermodynamic potentials for H^+ reduction compared to CO_2 reduction to formate (-0.028 V[34] vs -0.150 V[18] vs $Fe(C_5H_5)_2^{+/0}$, respectively, in CH_3CN). Since the former is more positive than the latter, hydrogen is the more favorable thermodynamic product upon reduction under standard state conditions (1 M H^+).

A full Pourbaix diagram that spans a larger range of proton activity (pK_a) provides a more complete picture in acetonitrile (Scheme 2.3). The thermodynamic potential for proton reduction shifts according to the pK_a of the solution by 59 mV per unit according to the Nernst equation for a 2 e-, $2H^+$ process. Similarly, CO_2 reduction to formic acid follows the same relationship until the solution pK_a matches that of formic acid to generate formate. For CO_2 reduction to formate, the thermodynamic potential shifts will deviate in accordance with a 2 e^-, 1 H^+ process, or 34.5 (or 59/2) mV per pK_a unit. The smaller decline in thermodynamic potential vs pK_a compared to H^+ reduction results in a crossing of potentials, where CO_2 reduction to formate occurs at a more positive potential at higher pK_a values and can thus be the more favorable thermodynamic product. The crossing point in the Pourbaix diagram (Scheme 2.3) matches the pK_a (25.1) which defines the initial point in which selective CO_2 reduction can be achieved in our diagram. A similar crossing in the $2H^+/H_2$ and CO_2/HCO_2^- is observed in Pourbaix diagrams in water,[35] although it is complicated by CO_2 equilibria with hydroxide at high pH.[36] The redrawn Pourbaix diagram shown in Scheme 2.2, where potential is replaced by hydricity, provides a more instructive guide for targeting catalysts to access the region where selective CO_2 reduction is possible.

2.3.2 Application of Thermodynamic Product Diagrams for Catalyst Discovery

To target the region in Scheme 2.1 (b) where selective CO_2 reduction to HCO_2^- is possible, $[HPt(dmpe)_2](PF_6)$ (**3**) was selected as a potential catalyst as it has an experimentally measured hydricity (ΔG_{H^-}) of 41.4 (eq 1).[15, 38] The preparation and characterization of the hydride $[HPt(dmpe)_2](PF_6)$ (**3**), hydride precursor $[Pt(dmpe)_2]$ (**2**), and post-hydride transfer intermediate

$[Pt(dmpe)_2](PF_6)_2$ (**1**) have been previously reported.[38-39] Complex **1**, **2** and **3** are diamagnetic with easily distinguishable ^{31}P {^{1}H} NMR spectral signatures. $[Pt(dmpe)_2](PF_6)_2$ (**1**) exhibits a 2 e^- reduction to $[Pt(dmpe)_2]$ (**2**) at -1.73 V vs $Fe(C_5H_5)_2^{+/0}$ in acetonitrile (Figure 2.1, black trace). The reactions with protons and pK_a of each step starting with the fully reduced species is described in eq 7.

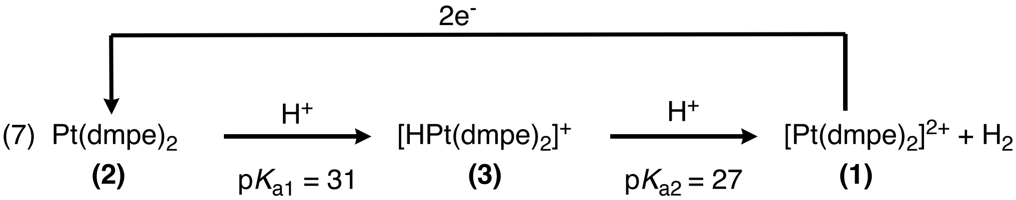

$$(7)\quad \underset{\textbf{(2)}}{Pt(dmpe)_2} \xrightarrow[pK_{a1} = 31]{H^+} \underset{\textbf{(3)}}{[HPt(dmpe)_2]^+} \xrightarrow[pK_{a2} = 27]{H^+} \underset{\textbf{(1)}}{[Pt(dmpe)_2]^{2+}} + H_2$$

values will result in H_2 evolution. Conversely, the metal hydride will be stable to protonation using acids with higher pK_a values.

The pK_a (31.1) [38] of the metal hydride (designated as pK_{a1} in eq 7) provides an upper bound on acids that can be used for metal hydride generation. According to eq 4 and Scheme 2.2, the threshold for H_2 evolution lies at a pK_a of 26 (designated as pK_{a2} in eq 7); acids with lower pK_a. According to Scheme 2.2, $[HPt(dmpe)_2](PF_6)$ (**3**) can be selectively generated at an electrode using proton sources with pK_a values between pK_{a1} (31.1) and pK_{a2} (25.5). For this purpose phenol was selected as the acid source, which has a pK_a of 29.1 in CH_3CN,[40] which is sufficiently acidic to generate $[HPt(dmpe)_2](PF_6)$ (**3**) without additional protonation to evolve H_2. No reaction is observed upon addition of phenol to $[HPt(dmpe)_2](PF_6)$ (**3**) by ^{31}P NMR spectroscopy, confirming it is not sufficiently acidic to protonate the metal (Figure 2.2).

Electrolytic generation of $[HPt(dmpe)_2](PF_6)_2$ (**2**) is also facilitated because its reduction potential lies more negative (–2.8 V vs $Fe(C_5H_5)_2^{+/0}$) than the catalyst resting state $[Pt(dmpe)_2](PF_6)_2$ (**3**) (–1.7 V vs $Fe(C_5H_5)_2^{+/0}$, (Figure 2.3),). This property has been observed in other Group 10 metal hydride complexes[21] along with multiple cobalt hydride complexes.[41-45] In

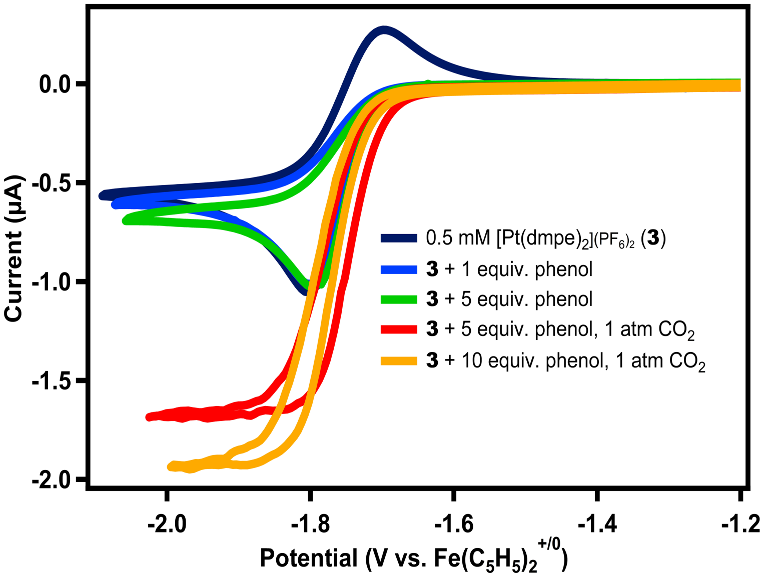

Figure 2.1. Cyclic voltammetry under 1 atm of N_2 of 0.5 mM solution of $[Pt(dmpe)_2](PF_6)_2$ (**1**) (black); after addition of 1 equivalent of phenol (blue); and 5 equivalents of phenol (green); and under CO_2 with 5 equivalents of phenol (red); and 10 equivalents phenol (orange). Conditions: 0.1 M Et_4NPF_6, 1mM $Fe(C_5H_5)_2$ present as an internal reference, glassy carbon working and auxiliary electrode, Ag/AgCl pseudoreference electrode, 10 mV/s scan rate.

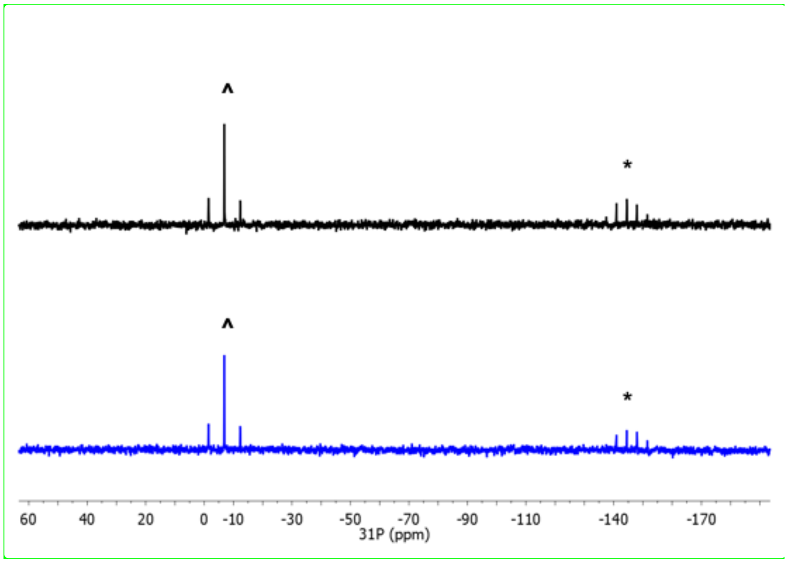

Figure 2.2. $^{31}P\{^1H\}$ NMR spectra of $[HPt(dmpe)_2](PF_6)$ (top) and after addition 1 equivalent of phenol (bottom). Where ^ denotes $[HPt(dmpe)_2]^+$ and * denotes PF_6 ion.

cases where the reduction potential of the hydride intermediate is positive of the parent complex, it will likely be reduced under electrolytic conditions to generate a stronger hydride donor. This

property is observed in cobaloxime complexes. In these cases, the hydricity of the reduced complex (or stronger hydride donor) can be applied to understand the p*K*a−dependent hydrogen evolution catalysis, as it is likely to be the dominant intermediate in heterolytic H−H bond formation. However, isolation of the metal hydride under electrochemical conditions could be more challenging. The reduced metal hydride would require a sufficiently large gap in pK_{a1} and pK_{a2} to achieve conditions where it would be stable, which may not apply in all cases.

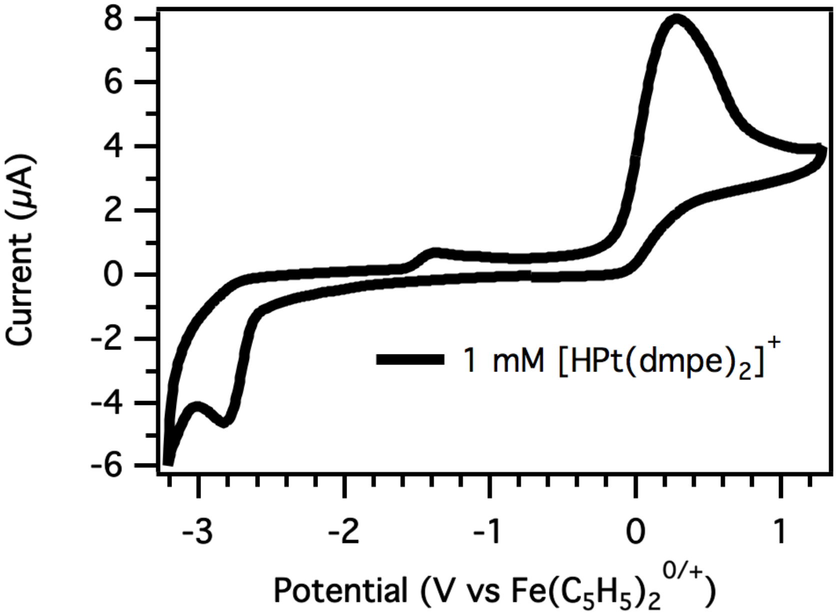

Figure 2.3. Cyclic voltammetry of 1 mM $[HPt(dmpe)_2](PF_6)$ (**2**) in 0.1 M $TBAPF_6$ in CH_3CN at 100 mV/s scan rate; under N_2.

Electrochemical reduction of **1** to **2** in the presence of phenol results in a loss of reversibility (blue trace in Figure 2.1), which is attributed to formation of the hydride, **3**. Higher concentrations of phenol do not result in an increase in current (green trace in Figure 2.1). This suggests that catalytic H_2 is not occurring at the Pt(II/0) reduction potential following hydride formation at the electrode. Instead, this suggests that the hydride intermediate could be isolated electrochemically under these conditions without appreciable H_2 evolution. Thus, these protonation studies show the utility of these diagrams in identifying suitable catalysts for target reactivity and optimizing catalyst operation conditions for product selectivity by tuning acid pK_a.

2.3.3 Selective Electrocatalytic Reduction of CO_2 to Formate

According to our thermodynamic analysis, $[HPt(dmpe)_2](PF_6)$ (**3**) is sufficiently hydridic to react with CO_2 to generate formate (ΔG in eq 6 = –2 kcal/mol). The cyclic voltammogram upon addition of CO_2 (1 atm) to **1** with phenol is shown in as the red trace in Figure 2.1. Titration of increasing concentrations of phenol results in an increase in current (Figure 2.1) which reaches a maximum at 10 equivalents.

Electrolysis was performed at –2.4 V vs $Fe(C_5H_5)_2^{+/0}$ under CO_2 (1 atm, 1 mM $[HPt(dmpe)_2](PF_6)$ in 10 mM phenol) for one hour (Figure 2.4 and 2.5). The headspace of the cell was analyzed by gas chromatography to detect and quantify H_2 and CO production. A small amount of H_2 (< 0.1 %) was sometimes observed but CO was never detected (see Figure 2.6 for H_2 calibration curve). The concentration of formate after electrolysis was either directly quantified using an internal DMF standard by ^1H NMR spectroscopy or by acidifying the post-electrolysis solution with HCl to quantify formic acid with a DMF internal standard using ^1H NMR spectroscopy, as described in the experimental methods (Figure 2.7 and Figure 2.8). The faradaic efficiency for formate production from either method was greater than 90% (see Figure 2.9 for formate calibration curve).

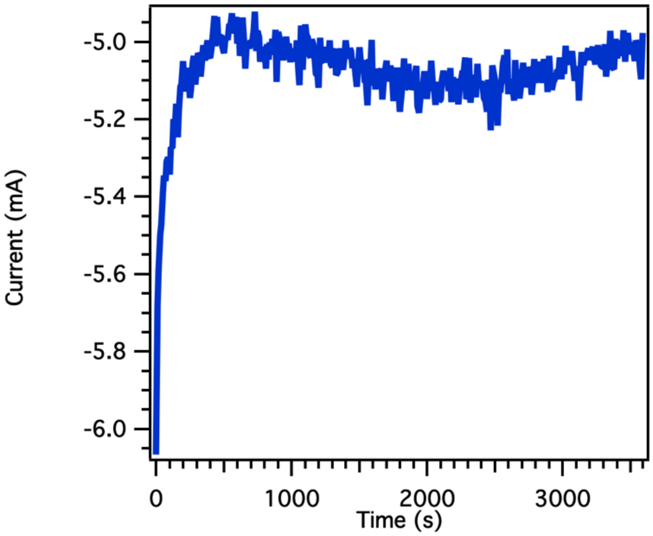

Figure 2.4. Current vs. Time plot of 1 hour electrolysis at -2.4 V vs. $Fe(C_5H_5)_2^{+/0}$ of 1 mM $[Pt(dmpe)_2](PF_6)_2$, 10 mM phenol and 1 mM $FeCp_2$ with 0.1 M $TBAPF_6$ in CH_3CN; under CO_2 (run 1). Total charge passed: 18.2 C; 3.14 equivalents of charge with respect to **3**.

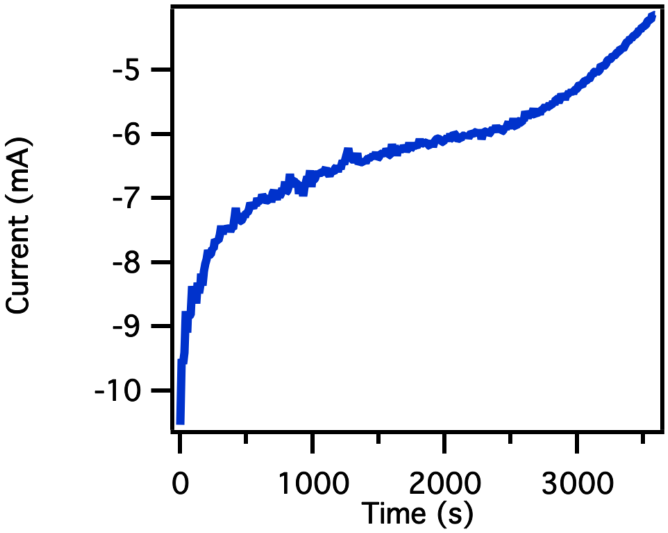

Figure 2.5. Current vs. Time plot of 1 hour electrolysis at -2.3 V vs. $Fe(C_5H_5)_2^{+/0}$ of 1 mM $[Pt(dmpe)_2](PF_6)_2$, 10 mM phenol and 1 mM $FeCp_2$ with 0.1 M $TBAPF_6$ in CH_3CN; under CO_2 (run 2). Total charge passed: 22.4 C; 3.87 equivalents of charge passed with respect to **3**.

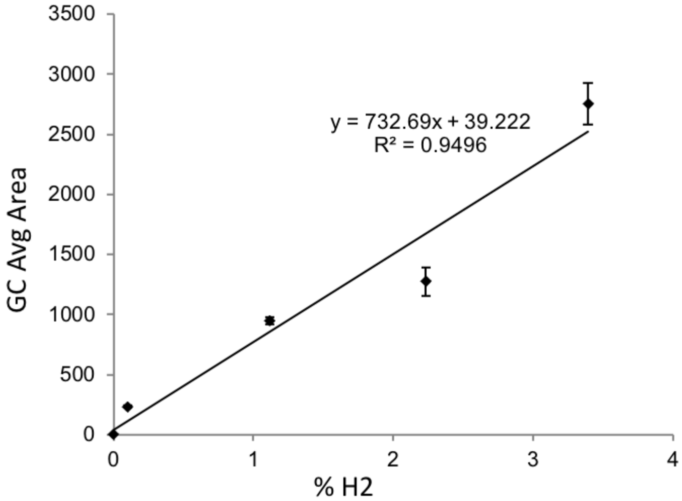

Figure 2.6. GC calibration curve for H_2 with 1 hour mixing time in acetonitrile. Points show average peak area and error bars show the standard deviation across 6 measurements. Linear fit equations are shown on the graph.

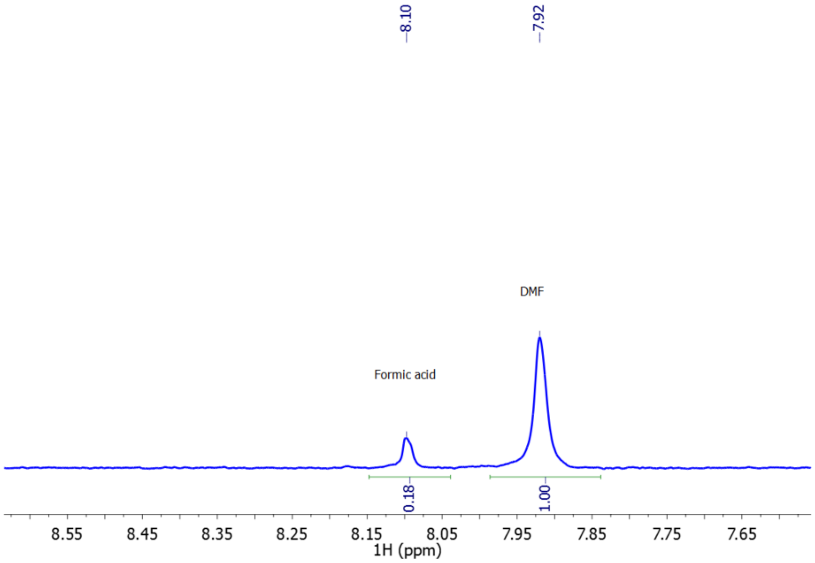

Fig. 2.8. ^{1}H NMR post electrolysis solution of run 1 with DMF standard following solution acidification (method B formic acid quantification). Run 2 electrolysis solution: 10 mM phenol and 1 mM $Fe(C_5H_5)_2$ with 0.1 M $TBAPF_6$ in CH_3CN; under CO_2.

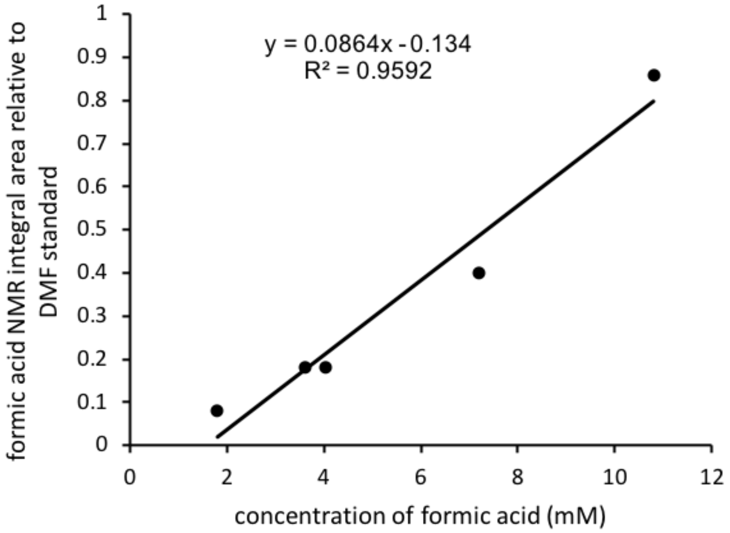

Figure 2.9. ^{1}H NMR solvent suppression calibration curve for formic acid in acetonitrile. Points show peak area Linear fit equations are shown on the graph.

$^{31}P\{^1H\}$ NMR spectra of the pre- and post-electrolysis solution displays a single resonance that corresponds to **1**. Quantification by integration relative to the PF_6^- anion (Figure 2.10 and 2.11) confirms complete retention of the catalyst after electrolysis.

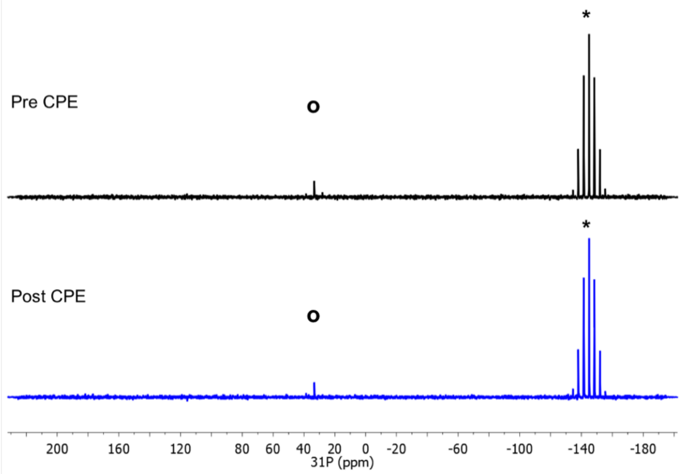

Figure 2.10. $^{31}P\{^1H\}$ NMR spectra of pre- (top) and post- (bottom) electrolysis solution (run 1); where **o** denotes $[Pt(dmpe)_2]^{2+}$ and * denotes PF_6 ion. Run 1 electrolysis solution: 1 mM $[Pt(dmpe)_2](PF_6)_2$, 10 mM phenol, and 1 mM $Fe(C_5H_5)_2$ with 0.1 M $TBAPF_6$ in CH_3CN; under CO_2.

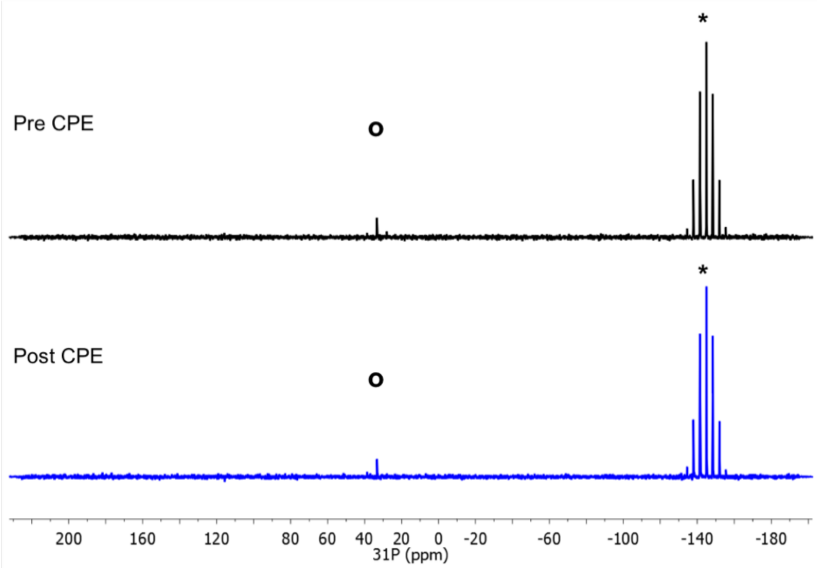

Figure 2.11. $^{31}P\{^{1}H\}$ NMR spectra of pre- (top) and post- (bottom) electrolysis solution (run 2); where **o** denotes $[Pt(dmpe)_2]^{2+}$ and * denotes PF_6 ion. Run 2 electrolysis solution: 1 mM $[Pt(dmpe)_2](PF_6)_2$, 10 mM phenol, and 1 mM $Fe(C_5H_5)_2$ with 0.1 M $TBAPF_6$ in CH_3CN; under CO_2.

The maximum catalytic current (i_c) in the cyclic voltammetry (Figure 2.1, orange trace) was used with the peak current under non-catalytic conditions (i_p) (Figure 2.1, black trace) to calculate an estimated observed rate constant (k_{obs}) of 0.5 s^{-1} (eq 8)[1, 46] for CO_2 reduction to formate. In eq 8, F is faraday's constant, v is scan rate, R is the ideal gas constant, T is temperature, n is the number of electrons passed and $\frac{i_c}{i_p}$ is the ratio of max catalytic current (i_c) observed under CO_2 with 10 equivalents of phenol and the peak current (i_p) with 10 equivalents of phenol in the absence of CO_2.

$$(8)\ k_{obs} = F\frac{v}{RT}(n')^3\left[\left(\frac{i_c}{i_p}\right)\left(\frac{0.446}{n}\right)\right]^2$$

The expression detailed in equation 8 can be used to calculate k_{obs} in pure kinetic zones where S-shaped curves are observed and the peak catalytic current (i_c) is not limited by substrate diffusion. In order to experimentally access this region, the rate of the chemical step must be fast relative to the timescale of the voltammogram. Thus, in the case of a fast catalytic step, S-shaped curves can be observed by increasing the substrate concentration or increasing the scan rate to limit substrate consumption. When catalysis is slow, scan rates should be decreased to approach the rate of the chemical step and must show 1st order dependence on catalyst concentration to ensure that substrate is not being depleted.[47] The conditions used to calculate the observed catalytic rate are detailed in Table 2.1.

The standard potential for CO_2 reduction to formate in acetonitrile was recently estimated.[18] Using this approximation, the thermodynamic potential under our conditions (pK_a of 29.1) is E° = –1.64 V vs $Fe(C_5H_5)_2^{+/0}$. Using the half-wave potential $E°_{1/2}$ = –1.73 V vs $Fe(C_5H_5)_2^{+/0}$,[48] the overpotential for catalysis is 90 mV.

To quantify any potential H_2 or formate generated directly at the electrode, an equivalent electrolysis in the absence of any Pt compound was performed (Figure 2.15). Analysis of the headspace by gas chromatography detected the presence of <0.1% mL H_2 and no CO in the headspace with no formate observed in solution by ^{1}H NMR spectroscopy.

Table 2.1. Conditions used to calculate observed catalytic rate constant (k_{obs})

scan rate (V/s)	n	n'	*ic* (uA)	*ip* (uA)	*ic/ip*	k_{obs}
0.01	2	2	1.92	1.05	1.8	0.5

2.3.4 Kinetics of Electron Transfer

To better understand the overall rate limiting factors for catalysis, the kinetics of electron transfer to generate the reduced metal species $[Pt(dmpe)_2]$ (**2**) at an electrode (step A in Figure

2.12) was considered. The two-electron reduction of $[Pt(dmpe)_2](PF_6)_2$ (**1**) to $[Pt(dmpe)_2]$ (**2**) was observed in acetonitrile by cyclic voltammetry (Figure 2.13).

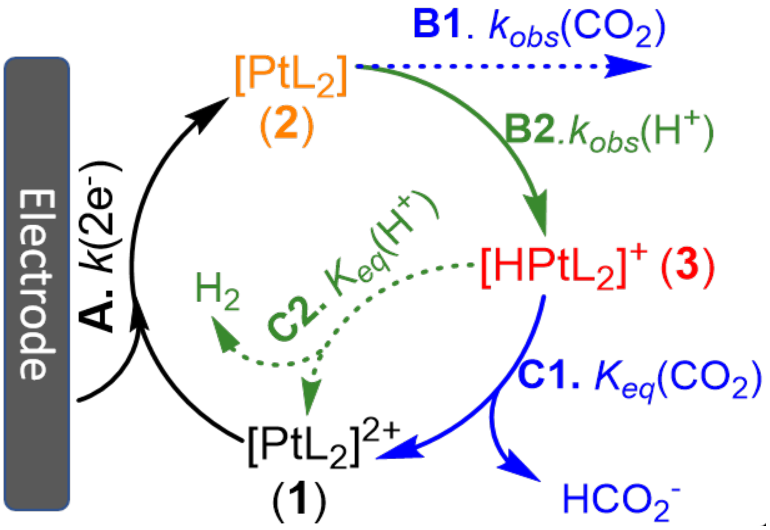

Figure 2.12. Proposed catalytic cycle for $[PtL_2]^{2+}$ in the presence of H^+ and CO_2, where L = (dmpe = 1,2-bis(dimethylphosphino)ethane) (dmpe). Potential branch points that could lead to unselective reduction are shown as dotted arrows. Solids arrows depict reaction pathways favored by either kinetic (*k*) or thermodynamic (K_{eq}) parameters, leading to high selectivity for CO_2 reduction to HCO_2^-.

The anodic and cathodic peak currents increase linearly with the square root of the scan rate (υ) (Figure 2.14) as predicted for a diffusion-controlled process by the Randles-Sevcik equation, eqn 9:

$$(9)\ i_p = 0.446\, F\, A\, C\, n^{\frac{3}{2}} \sqrt{\frac{F}{RT}}\, \sqrt{D}\, \sqrt{\upsilon}$$

Where i_p is the peak current (A), F is Faraday's constant (C mol^{-1}), A is the surface area of the electrode (cm^2), C is the bulk concentration of $[Pt(dmpe)_2](PF_6)_2$ (**1**) (mol cm^{-3}), n is the number of electrons, *D* is the diffusion coefficient (cm^2 s^{-1}), and υ is scan rate (V/s).[30, 49-50] The electrochemically-active surface area of the glassy carbon electrode was measured to be 0.011 cm^2 using chronoamperometry on a $Fe(C_5H_5)_2$ solution.[51]

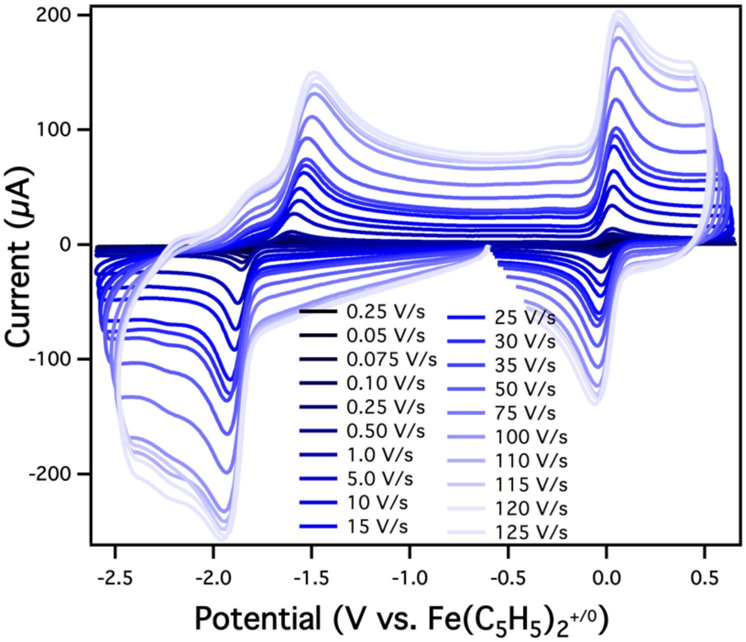

Figure 2.13. Cyclic voltammograms of a solution of 1 mM $[Pt(dmpe)_2](PF_6)_2$ in 0.1 M NBu_4PF_6 with 1 mM ferrocene at a glassy carbon working and counter electrode with a glass jacketed silver wire reference electrode in 0.1 M NBu_4PF_6 acetonitrile solution separated from the bulk solution by a porous Vycor frit.

The diffusion coefficient was found using the peak currents of reversible waves from scan rates (υ) 0.01 – 0.1 V/s using the Randles-Sevcik equation (Eq 9).[30, 50] For a reversible system, D for the oxidized or reduced species can be calculated using the slope of the best fit line in the i_p vs. $\upsilon^{1/2}$ plot (Figure 2.14) based on the relationship described by equation 10. [30, 50] From the slope (*m*) of the best fit line, the diffusion coefficients for the oxidized and reduced species are 2.49×10^{-6} and 4.15×10^{-6} cm^2 s^{-1} respectively.

$$(10)\qquad D = \left(\frac{m}{2.69 \times 10^5 * n^{\frac{3}{2}} * A * C}\right)^2$$

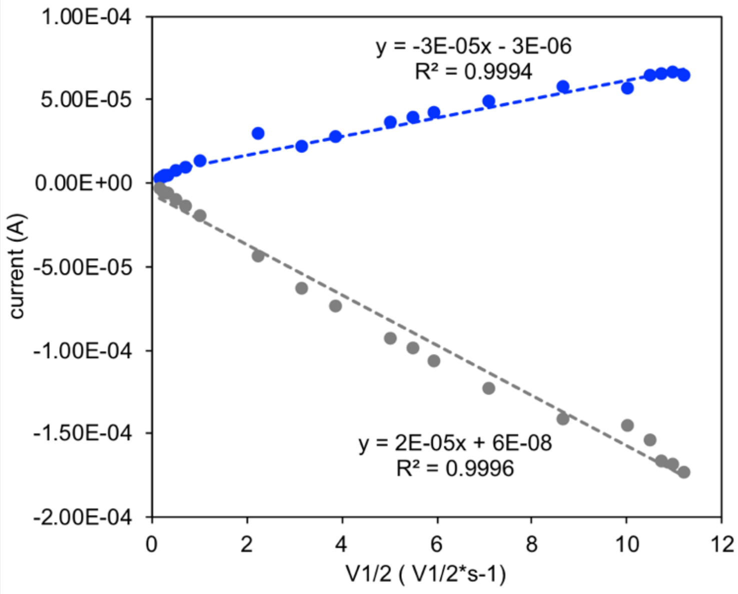

Figure 2.14. Plot of anodic (blue) and cathodic (grey) peak current (i_p) vs. $\upsilon^{1/2}$ for a solution of 1 mM $[Pt(dmpe)_2](PF_6)_2$ used to calculate D_O and D_R from scan rates between 0.025 – 125 V/s with 0.1 M NBu_4PF_6 in acetonitrile under N_2 atmosphere. Dotted trace shows best fit line.

The transfer coefficient α, which describes the symmetry of the electron transfer barrier, is 0.69 for reduction and was determined using the slope of the line from the plot of E_p vs. log(υ) (Figure 2.15).[50] The resulting values for α_c is 0.69 and α_a is 0.45, were calculated from scan rates 0.025 – 125 V/s using equations 11 and 12.[30]

$$(11)\qquad \alpha_c = \left(\frac{-2.303\,RT}{2nF}\right)\left(\frac{1}{m_c}\right)$$

$$(12)\qquad \alpha_a = 1 - \left(\frac{-2.303\,RT}{2nF}\right)\left(\frac{1}{m_a}\right)$$

At higher scan rates (υ > 0.1 V/s) ΔE_p increases, indicative of a quasi-reversible electrochemical couple.[52] The $E_{1/2}$ value of quasi-reversible redox events can be accurately obtained using the midpoint potential ($E_{1/2}(Pt^{II/0}) = -1.73$ V vs. $Fe(C_5H_5)_2^{0/+}$).[53]

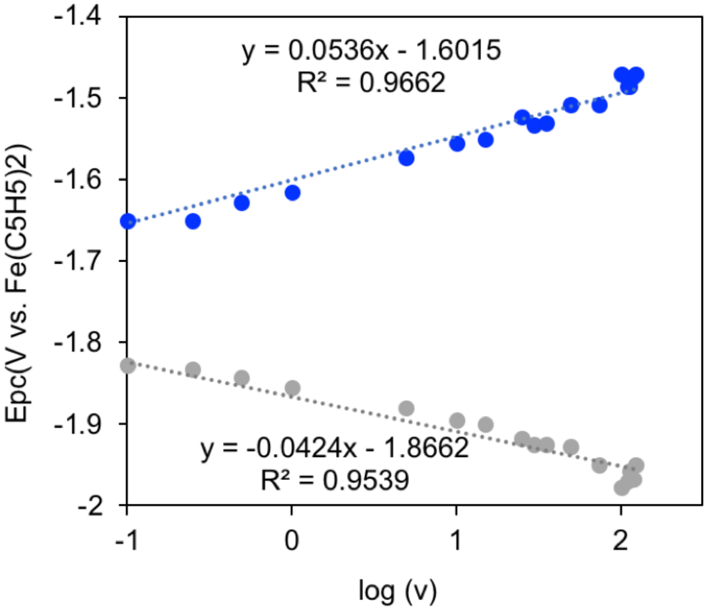

Figure 2.15. Plot of anodic (blue) and cathodic (grey) peak potential (E_p) vs. log of scan rate (υ) for a solution of 1 mM [Pt(dmpe)$_2$](PF$_6$)$_2$ used to calculate the electron transfer constant from scan rates between 0.025 – 125 V/s.

The rate of electron transfer (k_{ET}) was estimated using the Butler-Volmer method, where the change in peak potential difference with increasing scan rate was considered for the cathodic event according to the relationship described in equation 13.[30, 49-50]

$$(13) \quad E_{pc} = -\frac{2.303\,RT}{2\propto nF} log(\upsilon) + \left[E^{o\prime} - \frac{0.78\mathrm{RT}}{\alpha nF} + \frac{2.303RT}{\alpha nF}\log\left(k_{ET}\left(\frac{\sqrt{RT}}{\sqrt{\alpha nFD}}\right)\right)\right]$$

Solving equation 13 for the intercept portion (intercept described by Eq. 14) for k_{ET} gives the rate in log form shown in equation 15.

$$(14) \quad intercept = E^{o\prime} - \frac{0.78\,RT}{\propto nF} + \frac{2.303\,RT}{\propto nF}\, log\left(k_{ET}\left(\frac{\sqrt{RT}}{\sqrt{\propto nFD}}\right)\right)$$

$$(15) \quad log(k_{ET}) = \frac{\alpha nF}{2.303\,RT}\,(intercept - E^{o\prime}) + \; 0.339 - \log\left(\frac{\sqrt{RT}}{\sqrt{\alpha nFD}}\right)$$

Constants $\propto, n, F, D$, and the intercept from the best fit line for the cathodic scans (Figure 2.21), and E_{pc} of the best fit line are used in equation 15. The first term, $\frac{\alpha nF}{2.303\,RT}$ = 23.59; second term, $(intercept - E^{o\prime}) = -0.0885$; third term $\log\left(\frac{\sqrt{RT}}{\sqrt{\alpha nFD}}\right) = 1.76$ with a $D_R = 4.15 \times 10^{-6}$ cm^2 s^{-1}; and plugging into equation 15 gives equation 16. Solving equation 16 results in the expected electron transfer rate k_{ET} or 3.08×10^{-4} cm s^{-1}.

$$(16) \qquad log(k_{ET}) = [(23.59) * (-0.0885)] + 0.339 - 1.76$$

For comparison, the electron transfer rate constant for a series of other molecular electrocatalysts and their corresponding catalytic rates are given in Table 2.2, where electron transfer is not considered to be rate limiting. The reported electron transfer for the well-studied hydrogen evolution catalyst $[Co(dmgBF_2)_2(CH_3CN)]$ is one order of magnitude slower (10^{-5} $M^{-1}s^{-1}$) than that found for $[Pt(dmpe)_2](PF_6)_2$ (10^{-4} s^{-1}). However, this slow observed rate for electron transfer does not limit the overall observed rate reported for H_2 production (770 - 2.3 X 10^5 $M^{-1}s^{-1}$).

Table 2.2. Comparison of select reported electron transfer rates for transition metal complexes.

Compound		k_{ET} (cm s^{-1})	k_{app}	Ref.
$Fe(C_5H_5)_2$	Fe (III/II)	0.25 – 0.00089	N/A	*a-d*
$[Co(dmgBF_2)_2(CH_3CN)_2]$	Co (III/II)	2 x 10^{-5}	770 – 2 ×10^5 M^{-1} s^{-1}	*e,f*
Fe(TPP)Cl	Fe(I/0)	6.6 – 7.3×10^2	2.13× 10^5 M^{-2} s^{-1}	*g,h*
$[Pt(dmpe)_2]^{2+}$	Pt (II/I)	3.8 x 10^{-4}	0.5 s^{-1}	This work

a = *Anal. Chem.* **2011**, *83*, 1791–1799.; *b* = *Electrochim. Acta* **1983**, *28*, 301. ; *c* = *J. Appl. Electrochem.* **2010**, *40*, 409.; *d* = *Electroanalysis* 2010, 22, 269. ; *e* = *J. Am. Chem. Soc.* **2016**, *138*, 8309−8318.; *f* = *Chem. Commun.,* **2005**, 4723–4725. ; *g* = *Inorg. Chem.* **1988**, *27*, 12, 2144-2149. *h* = Chem. Sci., 2018, 9, 2952 – 2960.

2.3.5 Reactivity of [Pt(dmpe)$_2$] with CO$_2$

Generation of the reduced metal species [Pt(dmpe)$_2$] (**2**) offers the first divergent point in the proposed mechanism for catalysis at a metal hydride (Figure 2.12, Step B). The reduced metal species can either react with protons (step B2) to generate the metal hydride [HPt(dmpe)$_2$](PF$_6$) (**3**) or bind CO$_2$ to form CO$_2$ bound Pt complexes and off cycle products such as CO (Figure 2.12, Step B1).[54-59] The reaction between the reduced complex **2** and CO$_2$ in the absence of a proton source was investigated by ^{31}P{^{1}H} NMR spectroscopy in benzonitrile (**2** is sparingly soluble in acetonitrile). Upon addition of CO$_2$, there is complete conversion of **2** to a new species with a resonance of 29.58 ppm (Figure 2.16), which is likely either CO$_2$ or CO bound Pt complexes (*vide infra*).

The reactivity of [Pt(dmpe)$_2$] (**2**) with CO$_2$ was also explored using electrochemical techniques. The reduction of [Pt(dmpe)$_2$](PF$_6$)$_2$ (**1**) under 1 atm of CO$_2$ is irreversible at slow

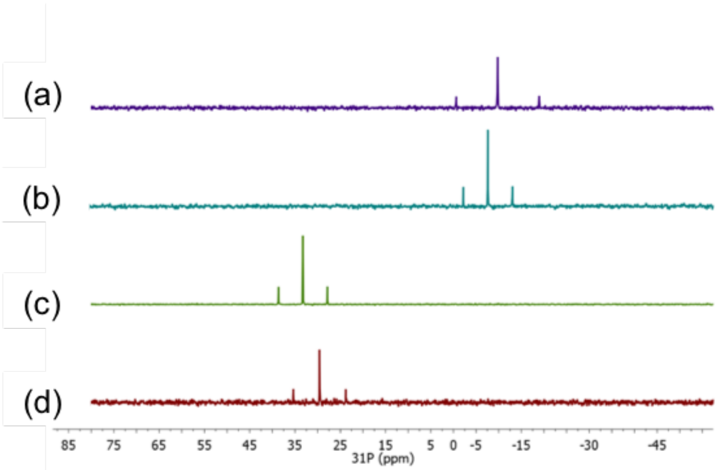

Figure 2.16. ^{31}P {^{1}H} NMR spectra of (a) [Pt(dmpe)$_2$], -9.77 ppm ($^3J_{Pt\text{-}P}$ = 3698 Hz); (b) [HPt(dmpe)$_2$]$^+$ -7.60 ppm ($^3J_{Pt\text{-}P}$ = 2199 Hz) (c) [Pt(dmpe)$_2$]$^{2+}$ 33.25 ppm ($^3J_{Pt\text{-}P}$ = 2175 Hz) under N$_2$ in benzonitrile and (d) [Pt(dmpe)$_2$] 29.58 ppm ($^3J_{Pt\text{-}P}$ = 2338 Hz) in saturated CO$_2$ benzonitrile.

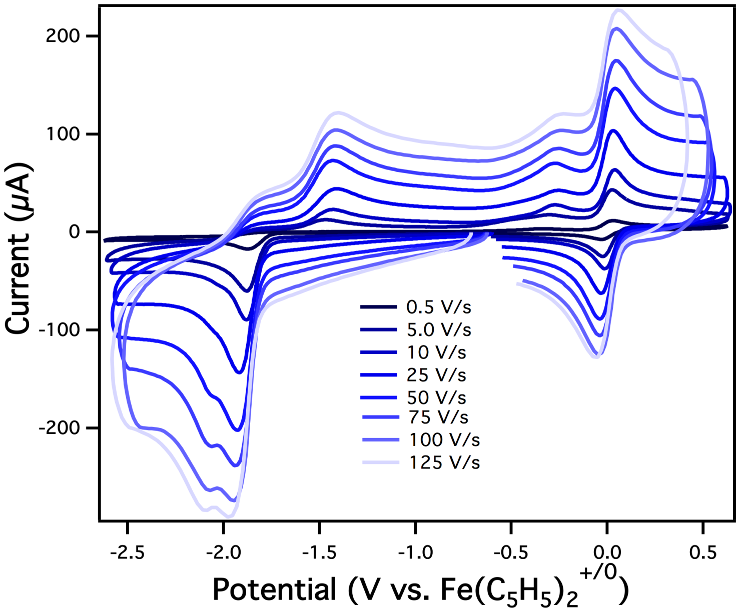

Figure 2.17. Cyclic voltammograms of $[Pt(dmpe)_2](PF_6)_2$ (1 mM) in acetonitrile (0.1 M NBu_4PF_6) with $Fe(C_5H_5)_2$ (1 mM) under CO_2 at a glassy carbon electrode at fast scan rates (v > 0.5 V/s). The reversible couple at 0.0 V is $Fe(C_5H_5)_2^{+/0}$.

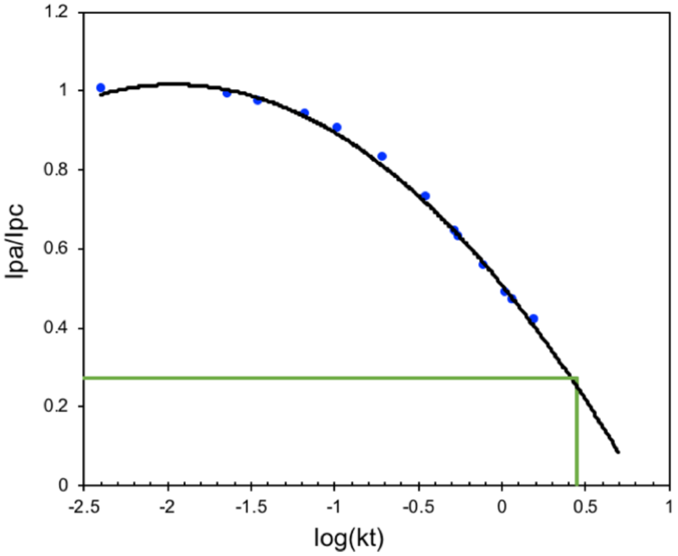

Figure 2.18. Working curve of i_{pa}/i_{pc} vs $k\tau$ used to calculate k_{CO2} plotted using tabulated data.[1] Green line shows average i_{pa}/i_{pc} ratio and corresponding $\log(k\tau)$ value observed at fast scan rates.

scan rates, indicating the reaction between [Pt(dmpe)$_2$] and CO$_2$ is complete (Figure 2.17). Both the cyclic voltammetry and NMR experiments indicate the reaction of **2** with CO$_2$ is exergonic.

Scan-rate dependent cyclic voltammetry of [Pt(dmpe)$_2$](PF$_6$)$_2$ (**1**) under 1 atm of CO$_2$ was used to determine the rate of the reaction. At fast scan rates, ($\upsilon > 1$ V/s) a return oxidation peak appears, but full reversibility is never recovered, and is accompanied by a shift of the E_{pc} to more negative potentials with increasing scan rate (Figure 2.17). Additionally, a new irreversible reduction peak is observed about ~200 mV more negative than the Pt(II/0) couple. The rate of CO$_2$ binding, k_{CO_2}, was extrapolated from a working curve of i_{pa}/i_{pc} vs. log($k\tau$) (Figure 2.18), where τ is the time in seconds to scan from $E_{1/2}$ to the turning potential.[1] An average CO$_2$ reaction rate, k_{CO_2}, of 352 s^{-1} was determined using peak current ratios at fast scan rates.

Infrared spectroelectrochemistry (IR-SEC) was used to characterize the product of the reaction between [Pt(dmpe)$_2$] and CO$_2$. Electrolysis of a CO$_2$ saturated solution of **1** (Figure 2.19) in 0.1 M NBu$_4$PF$_6$ at –1.83 V Fe(C$_5$H$_5$)$_2^{+/0}$ resulted in the formation of a new species, indicated by the growth of bands at 1890, 1729, 1680, 1643, and 1606 cm^{-1}. The bands observed at 1680, 1643, and 1606 cm^{-1} correlate to C=O stretching of CO$_3^{2-}$ and C-O stretch of HCO$_3^-$ in acetonitrile.[60] The bands at 1890 and 1729 cm^{-1} agree with previously reported CO and CO$_2$ bound transition metal complexes.[56, 59, 61-64] The reaction of CO$_2$ with reduced metal centers is proposed to generate unstable metal carboxylates with highly nucleophilic oxygen atoms which can react with another equivalent of CO$_2$ to give CO and CO$_3^{2-}$.[65-71] For comparison, the infrared spectra of the reduced species in the absence of CO$_2$ was also obtained. Upon electrolysis under N$_2$, two IR bands were observed at 2069 and 1825 cm^{-1} that correspond to NBu$_4$PF$_6$ and acetonitrile in solution (Figure 2.20). [72]

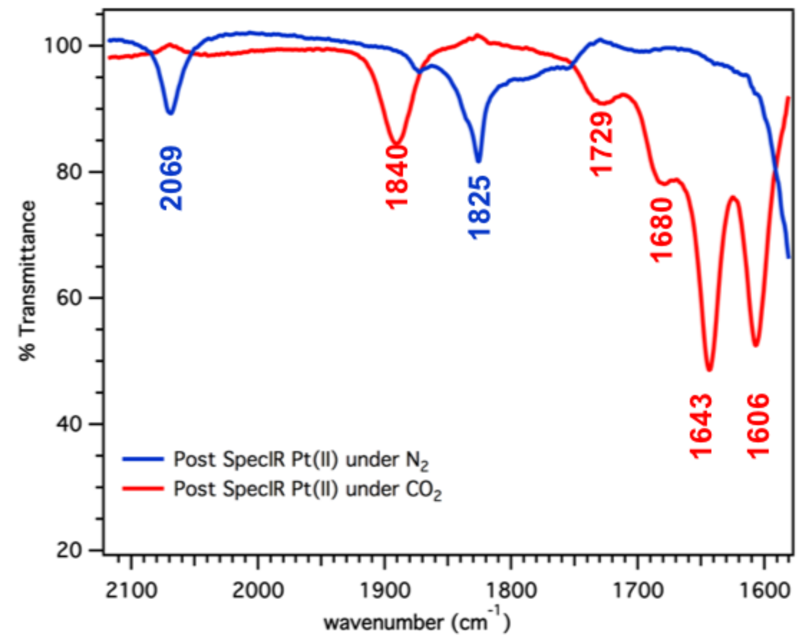

Figure 2.20. IR spectra collected after a 5 minute controlled potential electrolysis of a thin film containing 5 mM [Pt(dmpe)$_2$](PF$_6$)$_2$ and 0.1 M NBu$_4$PF$_6$ in acetonitrile under N$_2$ (blue) or CO$_2$ (red).

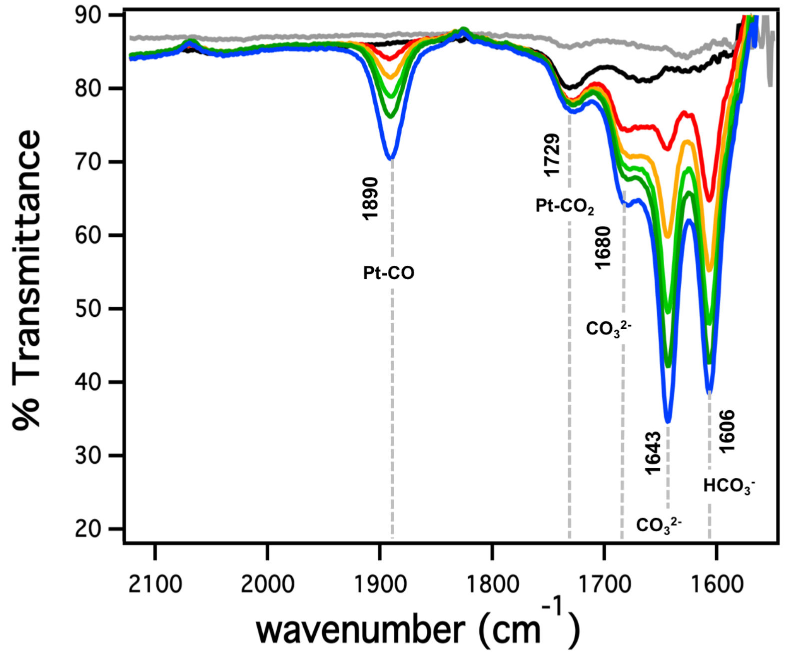

Figure 2.19. IR spectra of electyrolyzed solution of [Pt(dmpe)$_2$](PF$_6$)$_2$ at –1.83 V vs. Fe(C$_5$H$_5$)$_2^{+/0}$ in 0.1 M NBu$_4$PF$_6$ in CO$_2$ saturated solution (black to blue trace). Grey trace shows [Pt(dmpe)$_2$](PF$_6$)$_2$ solution before electrolysis under N$_2$.

2.3.6 Reactivity of [Pt(dmpe)$_2$] with H$^+$

Protonation of [Pt(dmpe)$_2$] (**2**) to generate the hydride [HPt(dmpe)$_2$]$^+$ (**3**) is necessary to ensure product selectivity for formate Figure 2.12, Step B2). The pK_a of [HPt(dmpe)$_2$]$^+$ (**3**) was previously measured to be 31.1;[38] therefore the free energy of protonation with phenol (pK_a = 29.1)[40] is –2.74 kcal/mol.

The chemical step of protonation that follows the two-electron reduction of [Pt(dmpe)$_2$](PF$_6$)$_2$ (**3**) is evident by the scan-rate dependent cyclic voltammetry. The Pt(II/0) reduction becomes irreversible upon the addition of phenol and retains its irreversibility at scan rates between 0.1-125 V/s (Figure 2.21).

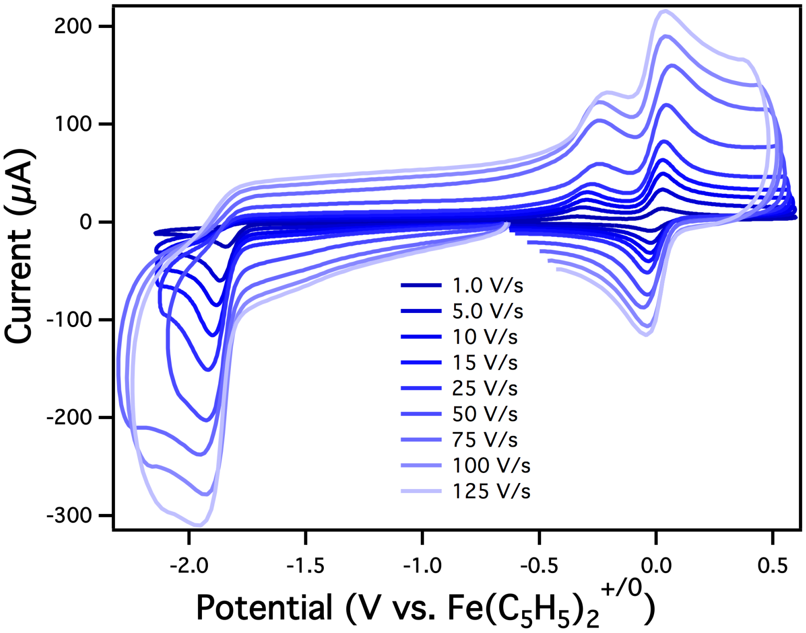

Figure 2.21. Cyclic voltammograms of [Pt(dmpe)$_2$](PF$_6$)$_2$ (1 mM) in the presence of phenol (0.1 M) in acetonitrile (0.1 M NBu$_4$PF$_6$) with Fe(C$_5$H$_5$)$_2$ (1 mM) under N$_2$ at a glassy carbon electrode at fast scan rates 5 – 125 V/s. The reversible couple at 0.0 V is Fe(C$_5$H$_5$)$_2^{+/0}$.

Determination of the protonation rate constant (k_{PT}) was complicated by slow electron transfer. The quasireversible behavior at higher scan rates complicates the direct measurement of the rate of protonation. Consequently, only a minimum bound for the rate of protonation could be determined using the expression described in equation 17. An irreversible chemical step following reversible electron transfer was used to determine that k_{PT} is greater than 10^5 s^{-1}, which is also consistent with the scan rate dependent data.

$$(17) \qquad k_{PT} \gg \frac{nF\upsilon}{RT}$$

2.3.7 Kinetic Control vs. Thermodynamic Control

From this thermodynamic and kinetic analysis, the free energy landscape (shown in Figure 2.22) for the proposed reactivity pathways at key branching points can be constructed using experimentally measured values.

Our collective experimental data outlines an energy landscape and compares the relative energetics of possible reaction pathways. The energy landscape is drawn at a potential equal to $E_{1/2}$ of $[Pt(dmpe)_2](PF_6)_2$ reduction potential of –1.73 V vs $Fe(C_5H_5)_2^{+/0}$. At this potential the free energies of the oxidized (**1**) and reduced (**2**) complex are equal in energy. This investigation gives insight into how $[Pt(dmpe)_2](PF_6)_2$ (**1**) achieves high product selectivity using kinetic and thermodynamic control at different proposed intermediates.

The reactivity of both H^+ and CO_2 at the first proposed intermediate $[Pt(dmpe)_2]$ (**2**) is exergonic (Figure 2.22). However, the rate of protonation is several orders of magnitude greater than the reaction with CO_2, indicating that hydride formation is favored under electrocatalytic conditions. The free energy of the reaction of $[Pt(dmpe)_2]$ with H^+ is –2.7 kcal/mol based on the difference in pK_a between $[HPt(dmpe)_2]^+$ (**3**) and phenol (Figure 2.22). The free energy of the reaction of CO_2 with $[Pt(dmpe)_2]$ was not calculated because the Pt-CO_2 intermediate could not be easily isolated for spectroscopic characterization. Since CO_2 binding proceeds to completion, the equilibrium constant (K_{eq}) is > 100, corresponding to a free energy greater than –2.7 kcal/mol (Figure 2.22). Therefore, the free energy for the reaction with CO_2 is at least as favorable as that for the reactivity with H^+. However, the rate constant for protonation is at least 5 orders of magnitude greater than that for CO_2 binding. Thus, the reactivity of the $[Pt(dmpe)_2]$ (**2**) to generate the active metal hydride $[HPt(dmpe)_2](PF_6)$ (**3**) in step B is under kinetic control.

Using thermodynamic cycles, the free energy of CO_2 and H^+ addition to $[HPt(dmpe)_2]^+$ are –2.2 and 5.5 kcal/mol, respectively (Figure 2.22). Therefore, selectivity for CO_2 insertion into the metal hydride instead of protonation to make H_2 is under thermodynamic control.

Under catalytic conditions, cyclic voltammetry was used to calculate an electrocatalytic rate of 0.5 s^{-1} as previously determined.[73] Slow electron transfer complicates the kinetic analysis of CO_2 insertion into **3** using electrochemical techniques. Nevertheless, the measured rate of

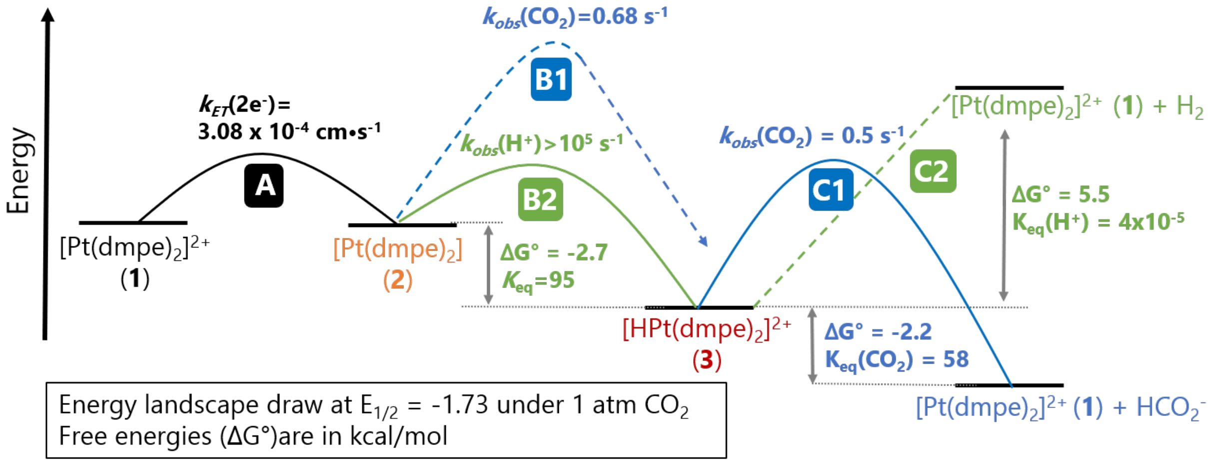

Figure 2.22. Proposed energy landscape for $[Pt(dmpe)_2](PF_6)_2$ electron transfer and possible chemical pathways. Transition state energies are not to scale. The products of B1 were not characterized and the equilibrium constant was not measured, although the reaction of 2 with CO_2 proceeds to completion. Equilibrium constants are given under standard state conditions.

protonation for the reduced species $[Pt(dmpe)_2]$ (**2**) to form $[HPt(dmpe)_2]^+$ (**3**) is significantly faster than the observed overall catalytic rate. Therefore, the reaction of CO_2 with $[HPt(dmpe)_2]^+$ (**3**) to form formate is likely the rate limiting chemical step with a rate of 0.5 s^{-1}.

2.3.8 Applicability of Thermodynamic Product Diagrams

The diagrams in Scheme 2.2 informed our choice of $[Pt(dmpe)_2](PF_6)_2$ (**1**) as a good catalyst candidate for selective CO_2 reduction to formate. The hydricity of the corresponding hydride $[HPt(dmpe)_2](PF_6)$ (**3**) is sufficient to reduce CO_2 and there are appropriate acids to access the region of selective reduction. Although the thermodynamic framework described herein proved effective for $[Pt(dmpe)_2]^{2+}$ (**1**), some considerations on its application to other potential catalysts are discussed. The diagrams shown in Scheme 2.2 can be drawn for any solvent provided the appropriate constants (ΔG_{H2} and ΔG_{HCO2-}) are known in each solvent. For example, the diagram illustrating the relationships between metal hydricity and proton activity in dimethylsulfoxide (DMSO) is shown in Figure 2.23 (ΔG_{H2} = 60.7 kcal/mol in DMSO).[24] The hydricity of formate (ΔG_{HCO2-}) in DMSO is estimated to be 42 kcal/mol)[74] so the equivalent diagram is shown in Figure 2.23. A published value for the pK_a of formic acid in DMSO was not found. Instead the line between CO_2/HCO_2^- is drawn across the whole range of pK_a values shown. Applying thermodynamic relationships with metal hydricity is most useful in organic solvents with self-consistent data on acid pK_a values. Most measurements of this type have been made in CH_3CN,[75-79] and to a lesser extent DMSO,[40] but additional values in various solvents are continually reported. Most measurements of this type have been made lesser extent DMSO,[40] but additional values in various solvents are continually reported.

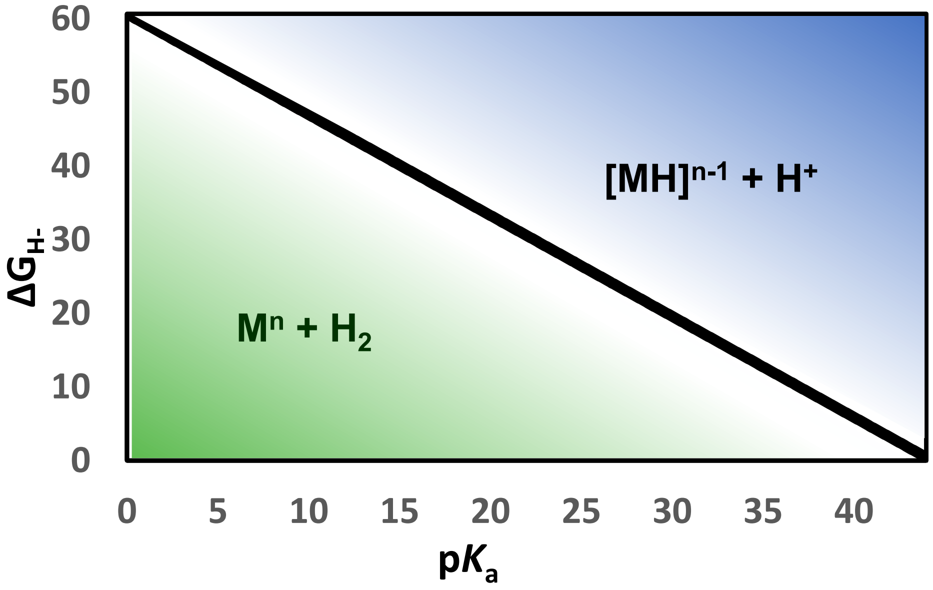

Figure 2.23. Thermodynamic product diagram showing the relationship between hydricity (ΔG_{H-}) and stability at various pK_a values to H_2 evolution in dimethylsulfoxide.

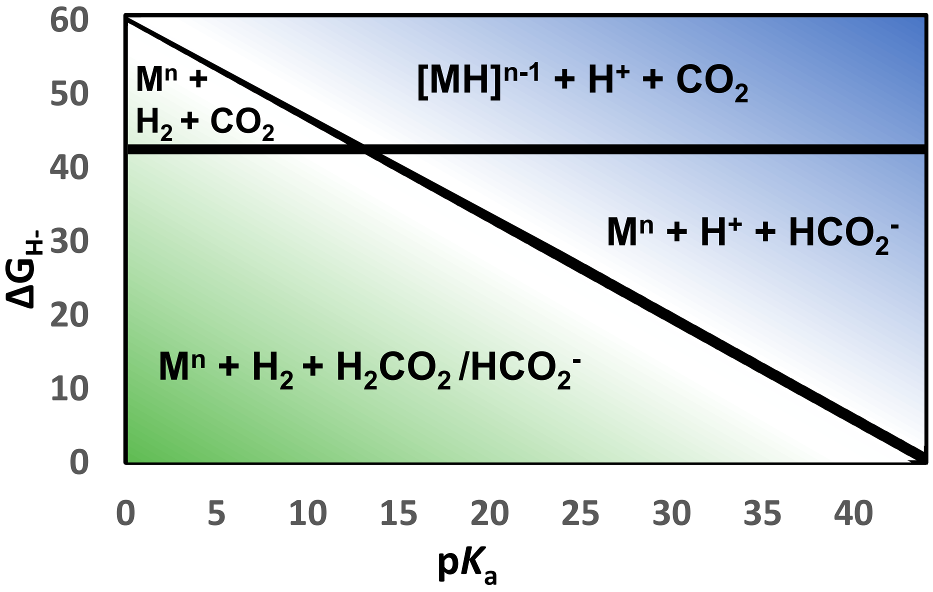

Figure 2.24. Thermodynamic product diagram showing the relationship between hydricity (ΔG_{H-}) and reactivity towards H^+ of various pK_a values to H_2 evolution or CO_2 reduction in dimethylsulfoxide.

ΔG_{H2} and ΔG_{HCO2-} have also been reported in aqueous solution (34.2 and 24.1 kcal/mol, respectively)[13] and the analogous diagrams are shown in Figure 2.25 and Figure 2.26, respectively. However, the diagrams do not account for the equilibria between CO_2 and OH^- to form HCO_3^- and CO_3^{2-}, which becomes more significant at higher pH values.

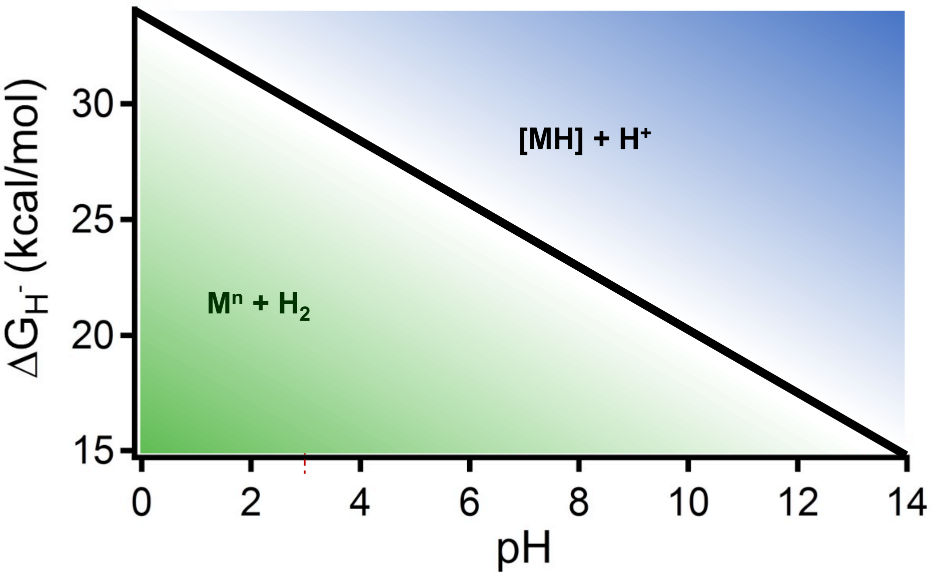

Figure 2.25. Thermodynamic product diagram showing the relationship between hydricity (ΔG_{H-}) and stability at various pH values to H_2 evolution in water.

The hydricity value (ΔG_{H}–) for equivalent metal hydrides also has a solvent dependence as described in Chapter 1 and other studies.[10, 14-15, 19-20, 22, 80] Hydricity values for transition metal hydrides tend to be lower and span a narrower range in solvents with higher dielectric constants, but their absolute values do not change in a predictable fashion by solvent. However, a notable trend is that hydricity values for transition metal hydrides in organic solvents tend to decline to a greater magnitude (become better donors) in water than HCO_2^- (ΔG_{HCO2-}). As a result, there are a few examples where CO_2 reduction to HCO_2^- is exergonic in water but endergonic in organic solvents, such as $[HNi(TMEPE)]^{2+}$ described in Chapter 1.[10, 22, 81] Additionally, detailed studies by Miller and coworkers determined that aqueous hydricity can also be dependent on anions commonly found in aqueous buffers, as well as hydroxide at higher pH values.[82]

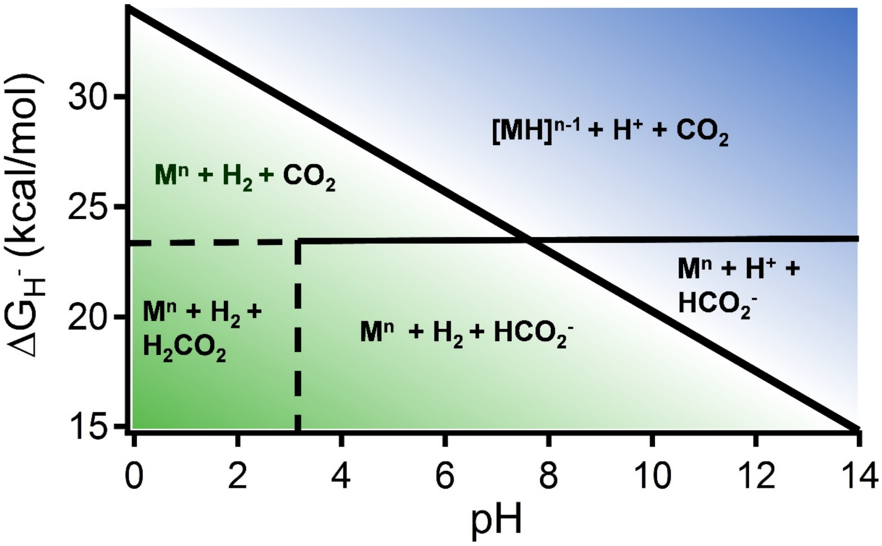

Figure 2.26. Thermodynamic product diagram showing the relationship between hydricity (ΔG_{H^-}) and reactivity towards H^+ of various pH values to H_2 evolution or CO_2 reduction in water.

2.4 Conclusion

Despite immense interest in electrolytic fuel generation, there are few guidelines for the rational design of catalysts for selective CO_2 reduction. Herein, thermodynamic relationships are utilized to understand the reactivity of metal hydrides as a branch point in the reactivity for formation of either H_2 or HCO_2^-. Analysis of these hydricity-pK_a relationships are used to construct a diagram that defines catalyst parameters for achieving selective CO_2 reduction by targeting an appropriate hydricity. Hydricity is a thermodynamic quantity that describes the bond energy of a key intermediate for catalysis and an activity descriptor for H_2 and HCO_2^- generation. Like activity descriptors, hydricity is general across many classes of compounds, expanding its utility. Identifying descriptors in molecular systems is particularly advantageous as bond energies are easily tuned through metal-ligand design.

A free energy landscape of our proposed catalytic cycle was constructed using experimentally measured observed rates. This landscape illustrates the relative energies of proposed intermediates in the catalytic cycle for CO_2 reduction using $[Pt(dmpe)_2](PF_6)_2$ complex.

The rate of electron-transfer was quantified from the electrode to $[Pt(dmpe)_2](PF_6)_2$ (**1**) to generate $[Pt(dmpe)_2]$ (**2**). The reduced species, **2** is the first critical intermediate for selective reduction, where direct activation of CO_2 could potentially lead to CO as the major CO_2 reduction product. In this study, the reaction of both H^+ and CO_2 with $[Pt(dmpe)_2]$ (**2**) is exergonic while the rate of the reaction with H^+ is several orders of magnitude faster. As a result, selective formation of $[HPt(dmpe)_2]^+$ (**3**) under catalytic conditions is under kinetic control. The reaction of the metal hydride **3** with CO_2 to generate formate is exergonic, while protonation to form H_2 is endergonic. Thus, selective reactivity at **3** with CO_2 is under thermodynamic control. Comparison of the overall catalytic rate with the rate constants measured for proposed individual steps indicates C-H bond formation by **3** and CO_2 is the rate-limiting step. To date, several kinetic studies of catalysis reactions at a metal hydride have found that hydride transfer (or substrate insertion into the metal hydride) is the rate determining step.[30-31]

2.5 Experimental Details

General considerations. All synthetic manipulations were performed under air and moisture-free conditions using a N_2 atmosphere unless otherwise noted. Solvents were degassed by sparging with argon gas and dried by passage through columns of activated alumina or molecular sieves. Deuterated solvents were purchased from Cambridge Isotopes Laboratories, Inc. and were degassed and stored over activated 3 Å molecular sieves prior to use. Ligand 1,2-bis(dimethylphosphino)ethane (dmpe), 98% and dichloro(1,5-cyclooctadiene)platinum(II), 99% were purchased from STREM and used as received. Compounds $[Pt(dmpe)_2][PF_6]_2$, $[HPt(dmpe)_2][PF_6]$, and $[Pt(dmpe)_2]$, were all prepared according to previously published procedures.[83-84]

For experiments carried out under CO_2, CO_2 gas was first passed through a VICI Metronics column and then through an acetonitrile bubbler. The acetonitrile-saturated CO_2 was used to sparge solution for at least 5 min before data collection, the sample was kept under a blanket of CO_2 for the duration of the experiment, and solution was re-sparged periodically between scans to maintain a constant CO_2 concentration in solution.

All other reagents were purchased from commercial vendors and used without further purification unless otherwise noted.

Physical Methods. ^1H and $^{31}P\{^1H\}$ nuclear magnetic resonance (NMR) spectra were collected at room temperature, unless otherwise noted, on a Bruker AVANCE 500 MHz spectrometer. Chemical shifts are reported in δ notation in parts per million (ppm). ^1H spectra referenced to residual proteo resonances of deuterated solvent. $^{31}P\{^1H\}$ spectra were referenced to H_3PO_4 at 0 ppm within Xwin-NMR or Bruker's Topspin software, which derives the chemical shifts from the known frequency ratios of the ^{31}P standard to the lock signal of the deuterated solvent. $^{31}P\{^1H\}$ spectra used in determining concentration were obtained either with long delay times (20 s) for 64 scans to ensure quantitative integration. Manual shimming, Fourier transformation, and automatic spectrum phasing were performed using Xwin-NMR software when using the 500 MHz spectrometer. Spectra were analyzed and figures were generated using MestReNova 6.0.2 software. Peak integrations were calculated within MestReNova.

Electrochemistry. Cyclic voltammetry was performed on a Pine Wavedriver 10 potentiostat with AfterMath software. For pre- and post-electrolysis solution analysis, CV was performed in a 150 mL glass controlled potential electrolysis cell using cylindrical carbon foam working and counter electrodes. All other CV experiments were performed in a 3 mL glass cell using glassy carbon working and counter electrodes. A glass jacketed silver wire reference electrode in 0.1 M $TBAPF_6$ acetonitrile solution separated from the bulk solution by a porous Vycor tip was used. Electrochemistry was performed on 0.5 mM or 1 mM solutions of analyte with appropriate amounts of phenol, 1 mM $Fe(C_5H_5)_2$, and 0.1 M $TBAPF_6$ as supporting electrolyte. For experiments carried out under CO_2, CO_2 gas was first run through a Drierite column and secondly through an acetonitrile bubbler. The acetonitrile-saturated CO_2 was used to sparge solution for at least 5 min before data collection, and the sample was kept under a blanket of CO_2 for the duration of the experiment. All CVs were recorded with compensation for solution resistance and were referenced relative to $Fe(C_5H_5)_2^{+/0}$ couple.

Controlled Potential Electrolysis and Product Analysis. Controlled potential electrolyses were performed in a Pine 150 mL cell with water jacket and five ground-glass ports (one 24/40, four

14/20). All cell ports were sealed with greased ground-glass joints with the exception of one 14/20 port, which was sealed with a SubaSeal rubber septum used for headspace sampling. Vitreous carbon foam rods were used for the working and counter electrodes, while a glass jacketed silver wire electrode in 0.1M $TBAPF_6$ fit with a Vycor tip was used as the reference. The carbon foam rods were attached to copper wire leads using conductive silver epoxy (AI Technology Prima-Solder EG8050) under Loctite epoxy. The counter electrode was separated from the bulk solution by a 10 mm glass tube with an extra-fine (Ace glass porosity E) fritted glass bottom; the tube was inserted through the 24/40 cell port and sealed with a ground-glass joint. The working and reference electrodes were connected to the exterior of the cell via nickel sleeves joining the electrode leads to a tungsten wire that was sealed through a 14/20 ground-glass stopper. A mercury pool, contained in a shallow glass cup, was placed at the bottom of each electrolysis sample.

Cell headspace was sampled with a Restek A-2 Luer lock gas-tight syringe. Headspace hydrogen was quantified by gas chromatography on an Agilent 7890B instrument with a Molsieve column. GC method details are as follows: dinitrogen carrier gas, 40 °C column temperature, TCD detector at 220 °C; helium carrier gas, 40 °C column temperature, TCD detector at 220 °C. Calibration curve was generated by injecting known percentages of H_2 into the full electrolysis cell setup, including the appropriate amount of acetonitrile, and stirring for 1 hour (Figure S19). CO_2 gas was first run through a VICI Metronics CO_2 gas purification column and secondly through an acetonitrile bubbler to saturate CO_2 with acetonitrile vapor before sparging solution for 30 mins. The electrolysis cell sample was kept under a blanket of CO_2 for the duration of data collection and sealed under acetonitrile saturated CO_2.

The post-electrolysis solution was collected for solution product analysis, quantification and catalyst retention. $^{31}P\{^{1}H\}$ NMR was used to determine catalyst concentration before and after electrolysis, by comparing catalyst resonance integration area to that of the PF_6 anion in solution. The solution product formate was identified and quantified using ^{1}H NMR spectroscopy. Formate product concentration was determined by comparing resonance integration area to that of an added internal DMF standard.

Method A: A 0.5 mL sample of post-electrolysis solution with added DMF standard was diluted with 0.05 mL of CD_3CN and spectra were collected using 16 scans with long delay times (20 seconds).

Method B: Post-electrolysis solution was acidified using dilute HCl (0.1 M) and DMF aliquot was added. A sample of 0.5 mL of solution was diluted with 0.05 mL of CD_3CN and spectra were collected using solvent suppression, 16 scans and long delay times (20 seconds). Observed relative concentrations of formic acid to DMF standard were corrected using a calibration curve for formic acid in acetonitrile using solvent suppression ^{1}H NMR spectroscopy.

Infrared Spectroelectrochemistry. Spectroelectrochemistry conducted using a Room Temperature Optically Transparent Thin Layer Electrochemical (RT OTTLE) cell fit with a CaF_2 window and a 3-electrode cell with Pt working, Pt counter electrode, and Ag wire reference electrode. Acetonitrile solutions of 5 mM $[Pt(dmpe)_2](PF_6)_2$ in 0.1 M NBu_4PF_6 under N_2 or saturated with CO_2 were loaded into cell. A cyclic voltammogram was collected prior to electrolysis to locate peak cathodic potential. Controlled potential electrolysis performed at peak cathodic potential for 5 minutes.

Concurrently, IR spectra were collected on a Thermo Scientific Nicolet iS5 FTIR spectrometer using with iD1 transmission accessory to hold OTTLE cell. IR spectra were collected Pre- and Post- electrolysis, as well as after 1 minute intervals during electrolysis.

2.6 References

1. Nicholson, R. S.; Shain, I., Theory of Stationary Electrode Polarography. Single Scan and Cyclic Methods Applied to Reversible, Irreversible, and Kinetic Systems. *Anal. Chem.* **1964,** *36* (4), 706-723.

2. Seh, Z. W.; Kibsgaard, J.; Dickens, C. F.; Chorkendorff, I.; Nørskov, J. K.; Jaramillo, T. F., Combining theory and experiment in electrocatalysis: Insights into materials design. *Science* **2017,** *355* (6321).

3. Inglis, J. L.; MacLean, B. J.; Pryce, M. T.; Vos, J. G., Electrocatalytic pathways towards sustainable fuel production from water and CO2. *Coord. Chem. Rev.* **2012,** *256* (21), 2571-2600.

4. Li, C. W.; Ciston, J.; Kanan, M. W., Electroreduction of carbon monoxide to liquid fuel on oxide-derived nanocrystalline copper. *Nature* **2014,** *508*, 504.

5. Mariano, R. G.; McKelvey, K.; White, H. S.; Kanan, M. W., Selective increase in CO<sub>2</sub> electroreduction activity at grain-boundary surface terminations. *Science* **2017,** *358* (6367), 1187.

6. Wang, Y.; Liu, J.; Wang, Y.; Al-Enizi, A. M.; Zheng, G., Tuning of CO_2 Reduction Selectivity on Metal Electrocatalysts. *Small* **2017,** *13* (43), 1701809.

7. Min, X.; Kanan, M. W., Pd-Catalyzed Electrohydrogenation of Carbon Dioxide to Formate: High Mass Activity at Low Overpotential and Identification of the Deactivation Pathway. *J. Am. Chem. Soc.* **2015,** *137* (14), 4701-4708.

8. Lee, C. H.; Kanan, M. W., Controlling H+ vs CO_2 Reduction Selectivity on Pb Electrodes. *ACS Catal.* **2015,** *5* (1), 465-469.

9. Zhang, S.; Kang, P.; Meyer, T. J., Nanostructured Tin Catalysts for Selective Electrochemical Reduction of Carbon Dioxide to Formate. *J. Am. Chem. Soc.* **2014,** *136* (5), 1734-1737.

10. Taheri, A.; Thompson, E. J.; Fettinger, J. C.; Berben, L. A., An Iron Electrocatalyst for Selective Reduction of CO_2 to Formate in Water: Including Thermochemical Insights. *ACS Catal.* **2015,** *5* (12), 7140-7151.

11. Roy, S.; Sharma, B.; Pecaut, J.; Simon, P.; Fontecave, M.; Tran, P. D.; Derat, E.; Artero, V., Molecular Cobalt Complexes with Pendant Amines for Selective Electrocatalytic Reduction of Carbon Dioxide to Formic Acid. *J. Am. Chem. Soc.* **2017,** *139* (10), 3685-3696.

12. Kang, P.; Cheng, C.; Chen, Z.; Schauer, C. K.; Meyer, T. J.; Brookhart, M., Selective Electrocatalytic Reduction of CO_2 to Formate by Water-Stable Iridium Dihydride Pincer Complexes. *J. Am. Chem. Soc.* **2012,** *134* (12), 5500-5503.

13. Connelly, S. J.; Wiedner, E. S.; Appel, A. M., Predicting the reactivity of hydride donors in water: thermodynamic constants for hydrogen. *Dalton Trans.* **2015,** *44* (13), 5933-5938.

14. Matsubara, Y.; Fujita, E.; Doherty, M. D.; Muckerman, J. T.; Creutz, C., Thermodynamic and Kinetic Hydricity of Ruthenium(II) Hydride Complexes. *J. Am. Chem. Soc.* **2012,** *134* (38), 15743-15757.

15. Wiedner, E. S.; Chambers, M. B.; Pitman, C. L.; Bullock, R. M.; Miller, A. J. M.; Appel, A. M., Thermodynamic Hydricity of Transition Metal Hydrides. *Chem. Rev.* **2016,** *116* (15), 8655-8692.

16. Loewen, N. D.; Neelakantan, T. V.; Berben, L. A., Renewable Formate from C–H Bond Formation with CO2: Using Iron Carbonyl Clusters as Electrocatalysts. *Acc. Chem. Res.* **2017,** *50* (9), 2362-2370.

17. DuBois, D. L.; Berning, D. E., Hydricity of transition-metal hydrides and its role in CO_2 reduction. *Appl. Organomet. Chem.* **2000,** *14* (12), 860-862.

18. Waldie, K. M.; Ostericher, A. L.; Reineke, M. H.; Sasayama, A. F.; Kubiak, C. P., Hydricity of Transition-Metal Hydrides: Thermodynamic Considerations for CO_2 Reduction. *ACS Catal.* **2018,** *8* (2), 1313-1324.

19. Creutz, C.; Chou, M. H., Rapid Transfer of Hydride Ion from a Ruthenium Complex to C1 Species in Water. *J. Am. Chem. Soc.* **2007,** *129* (33), 10108-10109.

20. Tsay, C.; Livesay, B. N.; Ruelas, S.; Yang, J. Y., Solvation Effects on Transition Metal Hydricity. *J. Am. Chem. Soc.* **2015,** *137* (44), 14114-14121.

21. Tsay, C.; Yang, J. Y., Electrocatalytic Hydrogen Evolution under Acidic Aqueous Conditions and Mechanistic Studies of a Highly Stable Molecular Catalyst. *J. Am. Chem. Soc.* **2016,** *138* (43), 14174-14177.

22. Ceballos, B. M.; Tsay, C.; Yang, J. Y., CO_2 reduction or HCO_2^- oxidation? Solvent-dependent thermochemistry of a nickel hydride complex. *Chem. Commun.* **2017,** *53* (53), 7405-7408.

23. Taheri, A.; Berben, L. A., Making C-H bonds with CO_2: production of formate by molecular electrocatalysts. *Chem. Commun.* **2016,** *52* (9), 1768-1777.

24. Wayner, D. D. M.; Parker, V. D., Bond energies in solution from electrode potentials and thermochemical cycles. A simplified and general approach. *Acc. Chem. Res.* **1993,** *26* (5), 287-294.

25. Fraze, K.; Wilson, A. D.; Appel, A. M.; Rakowski DuBois, M.; DuBois, D. L., Thermodynamic Properties of the Ni−H Bond in Complexes of the Type $[HNi(P_2RN_2R')_2](BF_4)$

and Evaluation of Factors That Control Catalytic Activity for Hydrogen Oxidation/Production. *Organometallics* **2007,** *26* (16), 3918-3924.

26. Rakowski Dubois, M.; Dubois, D. L., Development of Molecular Electrocatalysts for CO_2 Reduction and H_2 Production/Oxidation. *Acc. Chem. Res.* **2009,** *42* (12), 1974-1982.

27. Kang, P.; Meyer, T. J.; Brookhart, M., Selective electrocatalytic reduction of carbon dioxide to formate by a water-soluble iridium pincer catalyst. *Chem. Sci.* **2013,** *4* (9), 3497-3502.

28. Kang, P.; Zhang, S.; Meyer, T. J.; Brookhart, M., Rapid Selective Electrocatalytic Reduction of Carbon Dioxide to Formate by an Iridium Pincer Catalyst Immobilized on Carbon Nanotube Electrodes. *Angew. Chem. Int. Ed. (English)* **2014,** *53* (33), 8709-8713.

29. Tsay, C.; Ceballos, B. M.; Yang, J. Y., pH-Dependent Reactivity of a Water-Soluble Nickel Complex: Hydrogen Evolution vs Selective Electrochemical Hydride Generation. *Organometallics* **2018**.

30. Taheri, A.; Carr, C. R.; Berben, L. A., Electrochemical Methods for Assessing Kinetic Factors in the Reduction of CO_2 to Formate: Implications for Improving Electrocatalyst Design. *ACS Catal.* **2018,** *8* (7), 5787-5793.

31. Heimann, J. E.; Bernskoetter, W. H.; Hazari, N., Understanding the Individual and Combined Effects of Solvent and Lewis Acid on CO_2 Insertion into a Metal Hydride. *J. Am. Chem. Soc.* **2019,** *141* (26), 10520-10529.

32. Roubelakis, M. M.; Bediako, D. K.; Dogutan, D. K.; Nocera, D. G., Proton-coupled electron transfer kinetics for the hydrogen evolution reaction of hangman porphyrins. *Energ. Environ. Sci.* **2012,** *5* (7), 7737-7740.

33. Clark, M. L.; Cheung, P. L.; Lessio, M.; Carter, E. A.; Kubiak, C. P., Kinetic and Mechanistic Effects of Bipyridine (bpy) Substituent, Labile Ligand, and Brønsted Acid on Electrocatalytic CO_2 Reduction by Re(bpy) Complexes. *ACS Catal.* **2018**, 2021-2029.

34. Roberts, J. A. S.; Bullock, R. M., Direct Determination of Equilibrium Potentials for Hydrogen Oxidation/Production by Open Circuit Potential Measurements in Acetonitrile. *Inorg. Chem.* **2013,** *52* (7), 3823-3835.

35. Costentin, C.; Robert, M.; Savéant, J.-M., Current Issues in Molecular Catalysis Illustrated by Iron Porphyrins as Catalysts of the CO_2-to-CO Electrochemical Conversion. *Acc. Chem. Res.* **2015,** *48* (12), 2996-3006.

36. Keene, F. R., Chapter 1 - THERMODYNAMIC, KINETIC, AND PRODUCT CONSIDERATIONS IN CARBON DIOXIDE REACTIVITY A2 - Sullivan, B.P. In *Electrochemical and Electrocatalytic Reactions of Carbon Dioxide*, Elsevier: Amsterdam, 1993; pp 1-18.

37. Stirling, M. J.; Sweeney, G.; MacRory, K.; Blacker, A. J.; Page, M. I., The kinetics and mechanism of the organo-iridium-catalysed enantioselective reduction of imines. *Organic & Biomolecular Chemistry* **2016,** *14* (14), 3614-3622.

38. Curtis, C. J.; Miedaner, A.; Ellis, W. W.; DuBois, D. L., Measurement of the Hydride Donor Abilities of $[HM(diphosphine)_2]^+$ Complexes (M = Ni, Pt) by Heterolytic Activation of Hydrogen. *Journal of the American Chemical Society* **2002,** *124* (9), 1918-1925.

39. Berning, D. E.; Noll, B. C.; DuBois, D. L., Relative Hydride, Proton, and Hydrogen Atom Transfer Abilities of $[HM(diphosphine)_2]PF_6$ Complexes (M = Pt, Ni). *J. Am. Chem. Soc.* **1999,** *121* (49), 11432-11447.

40. Kütt, A.; Movchun, V.; Rodima, T.; Dansauer, T.; Rusanov, E. B.; Leito, I.; Kaljurand, I.; Koppel, J.; Pihl, V.; Koppel, I.; Ovsjannikov, G.; Toom, L.; Mishima, M.; Medebielle, M.; Lork, E.; Röschenthaler, G.-V.; Koppel, I. A.; Kolomeitsev, A. A., Pentakis(trifluoromethyl)phenyl, a Sterically Crowded and Electron-withdrawing Group: Synthesis and Acidity of Pentakis(trifluoromethyl)benzene, -toluene, -phenol, and -aniline. *J. Org. Chem.* **2008,** *73* (7), 2607-2620.

41. Fang, M.; Wiedner, E. S.; Dougherty, W. G.; Kassel, W. S.; Liu, T.; DuBois, D. L.; Bullock, R. M., Cobalt Complexes Containing Pendant Amines in the Second Coordination Sphere as Electrocatalysts for H_2 Production. *Organometallics* **2014,** *33* (20), 5820-5833.

42. Koelle, U.; Paul, S., Electrochemical reduction of protonated cyclopentadienylcobalt phosphine complexes. *Inorganic Chemistry* **1986,** *25* (16), 2689-2694.

43. Marinescu, S. C.; Winkler, J. R.; Gray, H. B., Molecular mechanisms of cobalt-catalyzed hydrogen evolution. *Proceedings of the National Academy of Sciences* **2012,** *109* (38), 15127-15131.

44. Solis, B. H.; Hammes-Schiffer, S., Proton-Coupled Electron Transfer in Molecular Electrocatalysis: Theoretical Methods and Design Principles. *Inorg. Chem.* **2014,** *53* (13), 6427-6443.

45. Wiedner, E. S.; Bullock, R. M., Electrochemical Detection of Transient Cobalt Hydride Intermediates of Electrocatalytic Hydrogen Production. *J. Am. Chem. Soc.* **2016,** *138* (26), 8309-8318.

46. Saveant, J. M.; Vianello, E., Potential-sweep chronoamperometry: Kinetic currents for first-order chemical reaction parallel to electron-transfer process (catalytic currents). *Electrochimica Acta* **1965,** *10* (9), 905-920.

47. Rountree, E. S.; McCarthy, B. D.; Eisenhart, T. T.; Dempsey, J. L., Evaluation of Homogeneous Electrocatalysts by Cyclic Voltammetry. *Inorg. Chem.* **2014,** *53* (19), 9983-10002.

48. Appel, A. M.; Helm, M. L., Determining the Overpotential for a Molecular Electrocatalyst. *ACS Catalysis* **2014,** *4* (2), 630-633.

49. Allen J. Bard, L. R. F., *Electrochemical Methods: Fundamentals and Applications, 2nd Edition*. Wiley: 200.

50. Saveant, J.-M., *Elements of Molecular and Biomolecular Electrochemistry*. Wiley: New York: 2006.

51. Kadish, K. M.; Ding, J. Q.; Malinski, T., Resistance of nonaqueous solvent systems containing tetraalkylammonium salts. Evaluation of heterogeneous electron transfer rate constants for the ferrocene/ferrocenium couple. *Analytical Chemistry* **1984,** *56* (9), 1741-1744.

52. Zanello, P., *Inorganic Electrochemistry: Theory, Practice and Application*. The Royal Society of Chemistry 2003.

53. Connelly, N. G.; Zanello, P., *Inorganic Electrochemistry: Theory, Practice and Application*. Royal Society of Chemistry: 2007.

54. Leitner, W., The coordination chemistry of carbon dioxide and its relevance for catalysis: a critical survey. *Coordination Chemistry Reviews* **1996,** *153*, 257-284.

55. Gibson, D. H., The Organometallic Chemistry of Carbon Dioxide. *Chemical Reviews* **1996,** *96* (6), 2063-2096.

56. Aresta, M.; Nobile, C. F.; Albano, V. G.; Forni, E.; Manassero, M., New nickel–carbon dioxide complex: synthesis, properties, and crystallographic characterization of (carbon dioxide)-bis(tricyclohexylphosphine)nickel. *Journal of the Chemical Society, Chemical Communications* **1975,** (15), 636-637.

57. Dohring, A. J., P. W.; Kruger, C.; Romao, M. J., The Ni(0)-CO_2 System: Structure and Reactions of [Ni(PCy_3)$_2$(n_2-CO_2)]. *Z. Naturforsch.* **1985,** *40B*, 484-488.

58. Mason, M. G.; Ibers, J. A., Reactivity of some transition metal systems toward liquid carbon dioxide. *Journal of the American Chemical Society* **1982,** *104* (19), 5153-5157.

59. Aresta, M.; Nobile, C. F., (Carbon dioxide)bis(trialkylphosphine)nickel complexes. *Journal of the Chemical Society, Dalton Transactions* **1977,** (7), 708-711.

60. Figueiredo, M. C.; Ledezma-Yanez, I.; Koper, M. T. M., In Situ Spectroscopic Study of CO_2 Electroreduction at Copper Electrodes in Acetonitrile. *ACS Catalysis* **2016,** *6* (4), 2382-2392.

61. Anderson, J. S.; Iluc, V. M.; Hillhouse, G. L., Reactions of CO_2 and CS_2 with 1,2-Bis(di-tert-butylphosphino)ethane Complexes of Nickel(0) and Nickel(I). *Inorg. Chem.* **2010,** *49* (21), 10203-10207.

62. Kim, Y.-E.; Kim, J.; Lee, Y., Formation of a nickel carbon dioxide adduct and its transformation mediated by a Lewis acid. *Chem. Commun.* **2014,** *50* (78), 11458-11461.

63. Kou, Y.; Nabetani, Y.; Masui, D.; Shimada, T.; Takagi, S.; Tachibana, H.; Inoue, H., Direct Detection of Key Reaction Intermediates in Photochemical CO_2 Reduction Sensitized by a Rhenium Bipyridine Complex. *J. Am. Chem. Soc.* **2014,** *136* (16), 6021-6030.

64. Sampson, M. D.; Froehlich, J. D.; Smieja, J. M.; Benson, E. E.; Sharp, I. D.; Kubiak, C. P., Direct observation of the reduction of carbon dioxide by rhenium bipyridine catalysts. *Energ. Environ. Sci.* **2013,** *6* (12), 3748-3755.

65. Maher, J. M.; Cooper, N. J., Reduction of carbon dioxide to carbon monoxide by transition-metal dianions. *Journal of the American Chemical Society* **1980,** *102* (25), 7604-7606.

66. Lee, G. R.; Maher, J. M.; Cooper, N. J., Reductive disproportionation of carbon dioxide by dianionic carbonylmetalates of the transition metals. *Journal of the American Chemical Society* **1987,** *109* (10), 2956-2962.

67. Chatt, J.; Kubota, M.; Leigh, G. J.; March, F. C.; Mason, R.; Yarrow, D. J., A possible carbon dioxide complex of molybdenum and its rearrangement product di-[small micro]-carbonato-bis{carbonyltris(dimethylphenylphosphine)molybdenum}: X-ray crystal structure. *Journal of the Chemical Society, Chemical Communications* **1974,** (24), 1033-1034.

68. Karsch, H. H., Funktionelle Trimethylphosphinderivate, III. Ambivalentes Verhalten von Tetrakis(trimethylphosphin)eisen : Reaktion mit CO_2. *Chemische Berichte* **1977,** *110* (6), 2213-2221.

69. Evans, G. O.; Walter, W. F.; Mills, D. R.; Streit, C. A., Reactions of carbon dioxide with metal carbonyl anions. *Journal of Organometallic Chemistry* **1978,** *144* (2), C34-C38.

70. Machan, C. W.; Chabolla, S. A.; Yin, J.; Gilson, M. K.; Tezcan, F. A.; Kubiak, C. P., Supramolecular Assembly Promotes the Electrocatalytic Reduction of Carbon Dioxide by Re(I) Bipyridine Catalysts at a Lower Overpotential. *Journal of the American Chemical Society* **2014,** *136* (41), 14598-14607.

71. Nichols, A. W.; Chatterjee, S.; Sabat, M.; Machan, C. W., Electrocatalytic Reduction of CO_2 to Formate by an Iron Schiff Base Complex. *Inorg. Chem.* **2018**.

72. Machan, C. W.; Sampson, M. D.; Kubiak, C. P., A Molecular Ruthenium Electrocatalyst for the Reduction of Carbon Dioxide to CO and Formate. *J. Am. Chem. Soc.* **2015,** *137* (26), 8564-8571.

73. Ceballos, B. M.; Yang, J. Y., Directing the reactivity of metal hydrides for selective CO_2; reduction. *Proceedings of the National Academy of Sciences* **2018,** *115* (50), 12686.

74. Moret, S.; Dyson, P. J.; Laurenczy, G., Direct synthesis of formic acid from carbon dioxide by hydrogenation in acidic media. *Nat Commun* **2014,** *5*.

75. Kütt, A.; Leito, I.; Kaljurand, I.; Sooväli, L.; Vlasov, V. M.; Yagupolskii, L. M.; Koppel, I. A., A Comprehensive Self-Consistent Spectrophotometric Acidity Scale of Neutral Brønsted Acids in Acetonitrile. *J. Org. Chem.* **2006,** *71* (7), 2829-2838.

76. Eckert, F.; Leito, I.; Kaljurand, I.; Kütt, A.; Klamt, A.; Diedenhofen, M., Prediction of acidity in acetonitrile solution with COSMO-RS. *Journal of Computational Chemistry* **2009,** *30* (5), 799-810.

77. Izutsu, K.; Pure, I. U. o.; Chemistry, A. C. C. o. E., *Acid-base Dissociation Constants in Dipolar Aprotic Solvents*. Blackwell Scientific Publications: 1990.

78. Kaljurand, I.; Kütt, A.; Sooväli, L.; Rodima, T.; Mäemets, V.; Leito, I.; Koppel, I. A., Extension of the Self-Consistent Spectrophotometric Basicity Scale in Acetonitrile to a Full Span of 28 pKa Units: Unification of Different Basicity Scales. *J. Org. Chem.* **2005,** *70* (3), 1019-1028.

79. Lõkov, M.; Tshepelevitsh, S.; Heering, A.; Plieger, P. G.; Vianello, R.; Leito, I., On the Basicity of Conjugated Nitrogen Heterocycles in Different Media. *European Journal of Organic Chemistry* **2017,** *2017* (30), 4475-4489.

80. Brereton, K. R.; Pitman, C. L.; Cundari, T. R.; Miller, A. J. M., Solvent-Dependent Thermochemistry of an Iridium/Ruthenium H_2 Evolution Catalyst. *Inorg. Chem.* **2016,** *55* (22), 12042-12051.

81. Burgess, S. A.; Appel, A. M.; Linehan, J. C.; Wiedner, E. S., Changing the Mechanism for CO_2 Hydrogenation Using Solvent-Dependent Thermodynamics. *Angew. Chem. Int. Ed. (English)* **2017,** *56* (47), 15002-15005.

82. Pitman, C. L.; Brereton, K. R.; Miller, A. J. M., Aqueous Hydricity of Late Metal Catalysts as a Continuum Tuned by Ligands and the Medium. *J. Am. Chem. Soc.* **2016,** *138* (7), 2252-2260.

83. A. Miedaner, D. L. D., and C. J. Curtis, Generation of Metal Formyl Complexes Using Nickel and Platinum Hydrides as Reducing Agents. *Organometallics* **1993,** *12*, 299-303.

84. Miller, A. J. M.; Labinger, J. A.; Bercaw, J. E., Homogeneous CO Hydrogenation: Ligand Effects on the Lewis Acid-Assisted Reductive Coupling of Carbon Monoxide. *Organometallics* **2010,** *29* (20), 4499-4516.

Appendix A

Electrochemical Investigation of $Al(OTf)_3$ Cation Effects on Fe Prophyrins CO_2 Reduction Reactivity

A.1. Motivations and Specific Aims

The product selectivity of Fe tetraphenylporphyrin (TPP) for the reduction of CO_2 to CO or formate (HCO_2^-) was investigated. Previous studies of FeTPP complexes found that the catalytic activity for CO_2 reduction increased in the presence of either Lewis acid cations or weakly H-bonding Bronsted acid in solution. Accompanying this increase in catalytic activity was a shift in product distribution from favoring CO (> 90%) to also generating small amounts of formate (10-35 %).[1-2] Electrochemical experiments were used to interrogate the interaction of Al(+3) cations with FeTPPCl (5,10,15,20-tetraphenyl-21*H*,23*H*-porphine iron(III) chloride) and FeF20TPPCl (FeF20TPPCl = 5,10,15,20-tetrakis(pentafluorophenyl)-21H,23H-porphyrin iron chloride) under catalytic CO_2 reduction conditions.

A.2. Background

Electrochemical CO_2 reduction to CO by Fe porphyrin catalysts has been well studied in the literature.[3-6] Initial work on Fe porphyrin complexes was performed by Saveant and co-workers using FeTPPCl (5,10,15,20-tetraphenyl-21*H*,23*H*-porphine iron(III) chloride). FeTPPCl was found to catalytically produce CO in the absence of a proton source under CO_2.[1-2, 7]

Previous studies utilizing mono- and divalent Lewis acid cations were found to improve the catalytic rate for CO production while also producing 10-35% formate as a byproduct.[2] The concentration of formate observed after electrolysis was greater for divalent Mg(2+), Ca(2+), and Ba(2+) cations than monovalent Li(+1) and Na(+1) cations. Electrochemical studies of FeTPPCl in the presence of Lewis acid cations were used to propose a mechanism for catalytic CO_2 reduction (Figure A.1). The Lewis acid cation is proposed to participate in a synergistic push-pull mechanism to activate CO_2, where the cation stabilizes the metal carboxylate formed at the reduced metal center. Similar synergistic effects were found using weak Brønstead acids; the

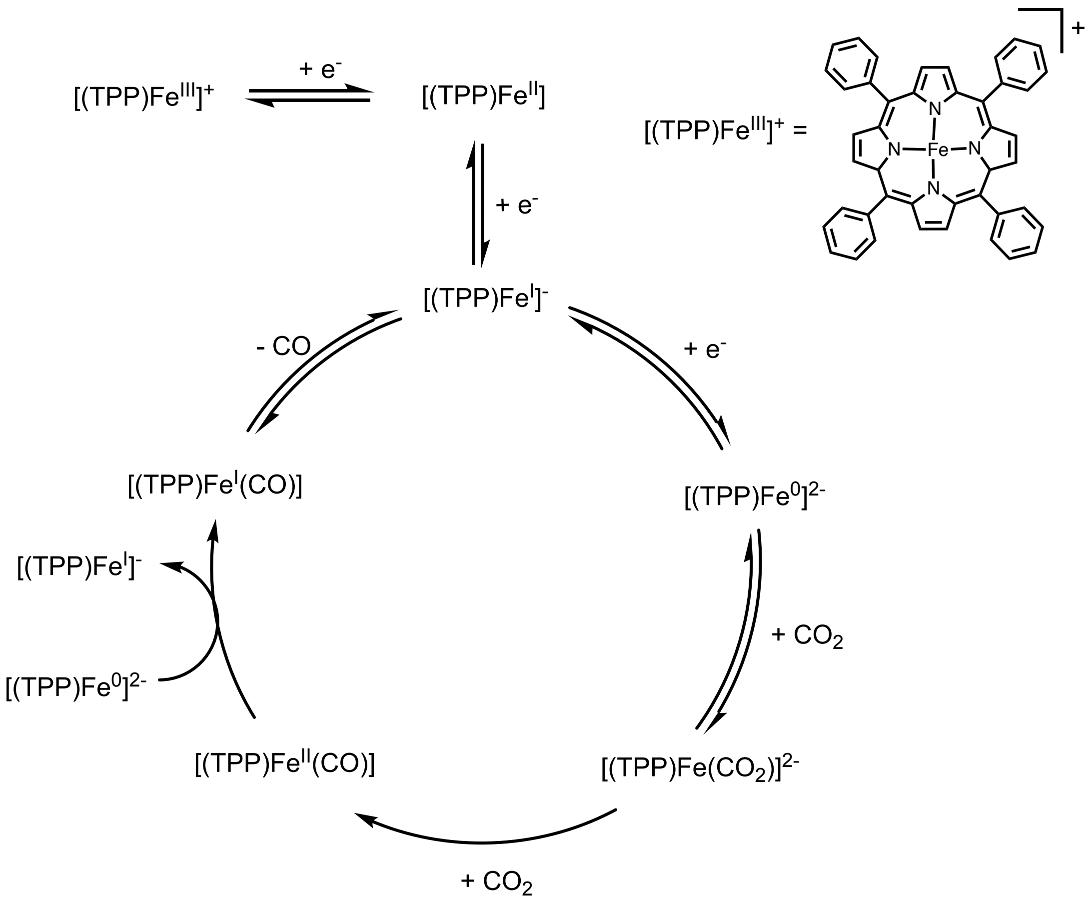

Figure A.1. Proposed Mechanism for Catalytic Electrochemical Reduction of CO_2 at FeTPPCl.

increased reactivity is hypothesized to be a result of hydrogen-bonding stabilizing the metal carboxylate intermediate.[1] Since this finding, others have investigated the role and effect of Lewis acid cations on catalysis.[8-14]

In the case of FeTPPCl, addition of Lewis acid cations increased the reactivity but also led to the formation of insoluble carbonates. Carbonate production inhibited catalysis by precipitating out of solution and blocking electrode surface area.

Improving the selectivity for formate production is one strategy to overcome deactivation by carbonate formation. It is hypothesized that formate production is a result of protonation of the bound Fe carboxylate species. Thus, generating a stable Fe carboxylate that is susceptible to protonation could switch catalyst product selectivity toward formate. To explore this hypothesis, the effect of $Al(OTf)_3$ on FeTPPCl and FeF20TPPCl (FeF20TPPCl = 5,10,15,20-tetrakis(pentafluorophenyl)-21H,23H-porphyrin iron chloride) reactivity with CO_2 to CO and formate was investigated using electrochemical techniques.

A.3. Results and Discussion

A.3.1. FeF20TPPCl Titration with $Mg(ClO_4)_2$ in DMF

The first aim of this investigation was to benchmark the effects of +2 Lewis acids using a fluorine substituted porphyrin FeF20TPPCl (FeF20TPPCl = 5,10,15,20-tetrakis(pentafluorophenyl)-21H,23H-porphyrin iron chloride) complex (Chart A.1) using cyclic voltammetry. Previous studies with unsubstituted FeTPPCl in the presence of +1 or +2 cations did not observe evidence of cation binding at a reduced Fe porphyrin species. Instead, cations in solution were hypothesized to stabilize CO_2 bound carboxylate species, resulting in an Fe carbonyl species to generate reduced CO_2 products.

Chart A.1. Structure of Fe porphyrin complexes FeTPPCl and FeF20TPPCl

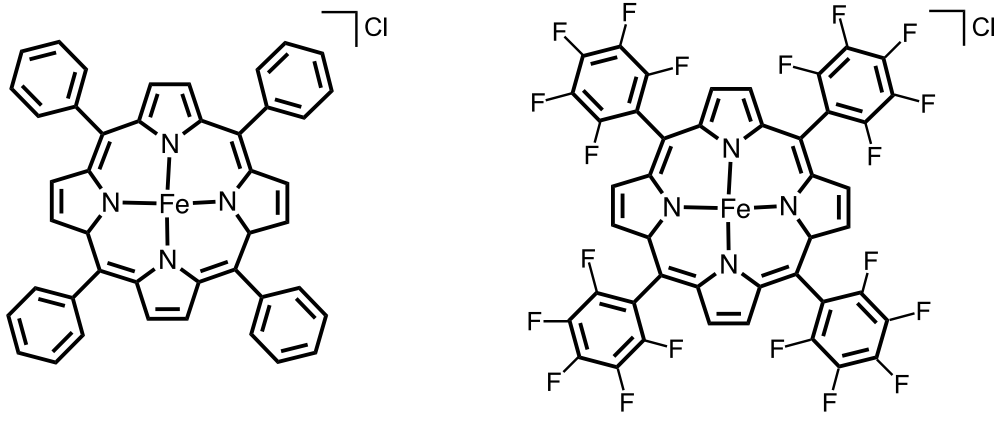

FeTPPCl

FeF20TPPCl

Cyclic voltammetry of the FeF20TPPCl at 0.1 V/s scan rate (Figure A.2; black trace) exhibits three reversible electrochemical events corresponding to the Fe(III/II), Fe(II/I), and Fe(I/0) couples. Addition of $Mg(ClO_4)_2$ causes small changes at the Fe(III/II) and Fe(I/0) couples (Figure A.2; Red to Blue trace). Ligand substitution reactions of DMF solvent with Cl anion at the Fe(III/II) couple of the FeF20TPPCl complex have previously been observed.[15] This exchange results in a clear anodic shift at the Fe(III/II) for both the cathodic and anodic waves. In the case of FeF20TPPCl in the presence of $Mg(ClO_4)_2$ does not result in clear peak shift. Instead, a broad return peak for the Fe(II/II) couple is observed . At the Fe (I/0) couple, a decrease in current is observed for the reductive scan. This small change in reductive current on the forward scan suggests a weak interaction between the reduced Fe species in solution with the Mg(+2) cations. Overall, interactions of the reduced FeTPPCl species and $Mg(ClO_4)_2$ in solution only weakly effect the cyclic voltammetry response such that all three redox events remain

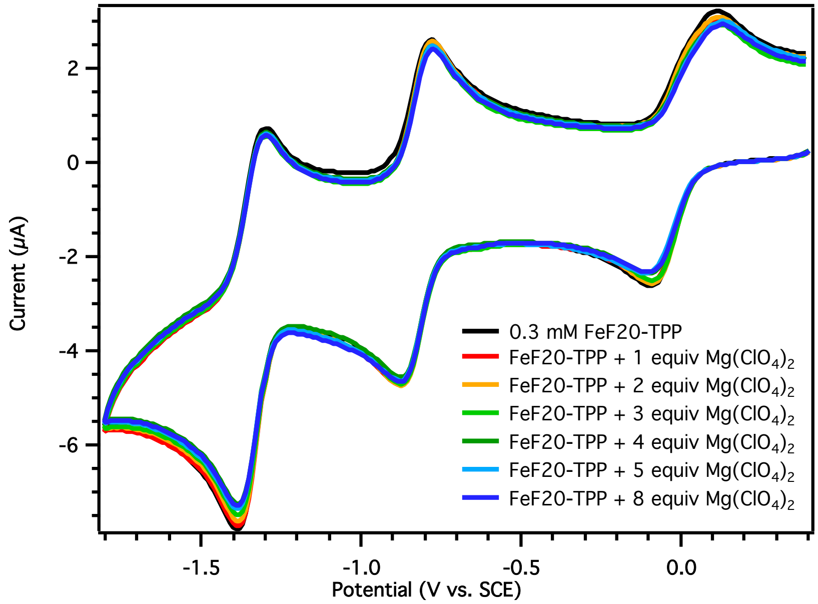

Figure A.2. Cyclic voltammograms of FeF20TPPCl (0.3 mM) in the presence of $Mg(ClO_4)_2$ in DMF (0.1 M NBu_4PF_6) under N_2 at a glassy carbon electrode at a scan rate of electrochemically reversible, which is in agreement with previous reports using FeTPPCl.

A.3.2. FeF20TPPCl with $Mg(ClO_4)_2$ under CO_2 in DMF

Upon saturating the DMF solution with CO_2, the cathodic peak of the Fe(I/0) couple loses reversibility and there is an increase in current indicating catalysis (Figure A.3). The catalytic reaction under these conditions is expected to be due to CO_2 reduction to generate CO and $MgCO_3$, where residual water in the solvent is acting as a proton source.[2] The peak shape of the catalytic wave is broad, indicating that catalysis is limited by substrate diffusion at 0.1 V/s scan rate.[16]

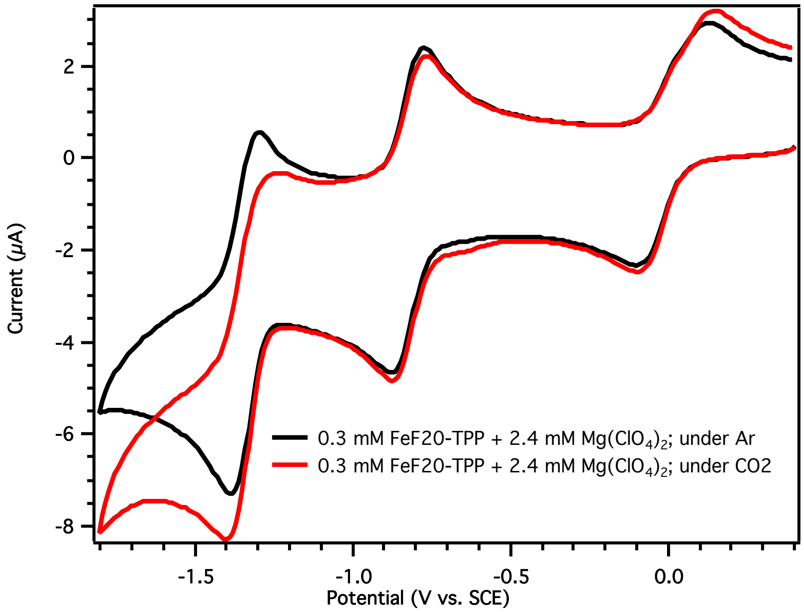

Figure A.3. Cyclic voltammograms of FeF20TPPCl (0.3 mM) in the presence of $Mg(ClO_4)_2$ in DMF (0.1 M NBu_4PF_6) under CO_2 at a glassy carbon electrode at a scan rate of 0.1 V/s.

Table A.1. Comparison of Peak Potential and current under Ar and CO_2 for FeF20TPPCl

Fe(I/0)	I_{pc} (μA)	E_{pc} (V vs SCE)	E_{pa} (V vs SCE)
under Ar	3.63	-1.39	-1.30
under CO_2	4.51	-1.40	---

For an irreversible chemical step following an electron transfer step, a peak shift toward more anodic potentials is expected. However, the cathodic peak potential (E_{pa}) for FeF20TPPCl under Ar or CO_2 are similar with ~10mV difference toward more cathodic potentials under CO_2 (Table A.1).

A.3.3. FeF20TPPCl with $Mg(ClO_4)_2$ under CO_2 with H_2O in DMF

Titration of small amounts of water to CO_2 saturated solutions results in an increase in current and an S-shaped catalytic wave at the Fe(0/I) couple (Figure A.4). The peak potential of the Fe(I/0) reduction shifts toward more anodic potentials with increasing equivalents of water.

Scan rate dependence studies of FeF20TPPCl under CO_2 and in the presence of excess $Mg(ClO_4)_2$ and H_2O exhibit a current plateau with increasing scan rate (Figure A.5). The forward catalytic peak also shows a shift toward more positive potentials with increasing scan rate. At fast scan rates (> 0.5 V/s) the return peak starts to gain reversibility, suggesting that the rate of the chemical step is on the same order of the CV time scale. This catalytic response is in agreement with previous reports using FeTPPCl under similar conditions.[2]

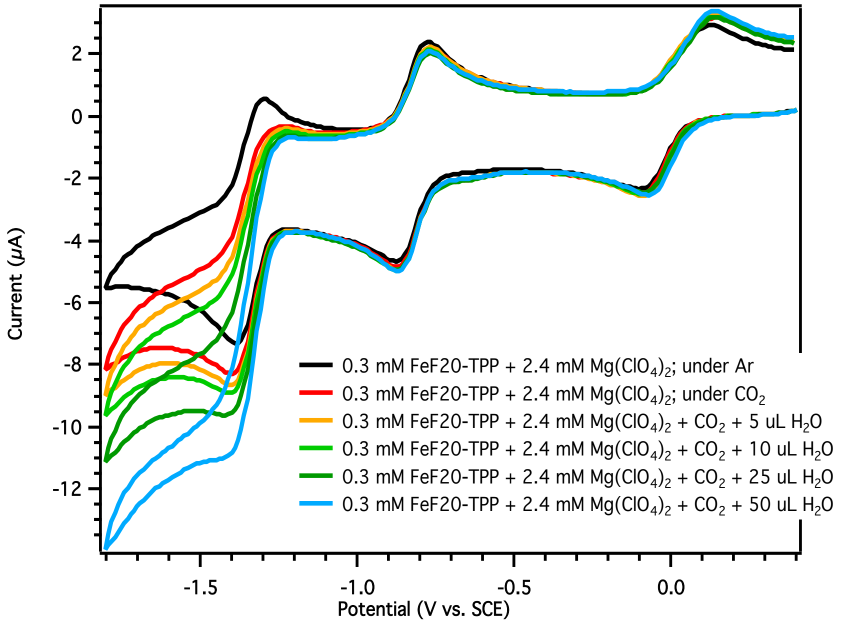

Figure A.4. Cyclic voltammograms of FeF20TPPCl (0.3 mM) in the presence of $Mg(ClO_4)_2$ (2.4 mM) and H_2O in DMF (0.1 M NBu_4PF_6) under CO_2 at a glassy carbon electrode at a scan rate of 0.1 V/s.

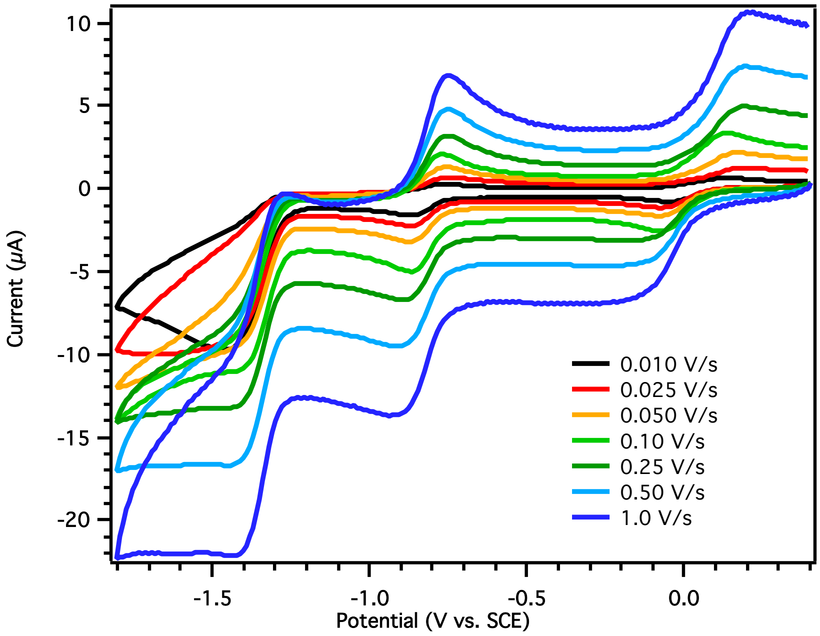

Figure A.5. Cyclic voltammograms of FeF20TPPCl (0.3 mM) in the presence of $Mg(ClO_4)_2$ (2.4 mM) and H_2O in DMF (0.1 M NBu_4PF_6) under CO_2 at a glassy carbon electrode at a scan rates 0.1 -1 V/s.

A.3.4. FeF20TPPCl and FeTPPCl Titration with Al(OTf)$_3$ in DMF

The influence of Al(OTf)$_3$ cations on the reactivity of Fe porphyrin CO$_2$ reduction catalysts were investigated. Previous work found that as higher charged cations were used, a greater % of formate was generated as a result of CO$_2$ reduction. However, the co-production of carbonate species was observed to lead to catalyst activity deactivation.[2] It is hypothesized that incorporating higher charged cations could lead to increased formate production to overcome catalyst deactivation via carbonate formation. In this study, the redox activity of both FeTPPCl and FeF20TPPCl complexes in the presence of Al(OTf)$_3$ were compared.

Before addition of Al(OTf)$_3$, both FeTPPCl and FeF20TPPCl exhibit a broad shoulder at the oxidative potential for the Fe(III/II) couple (Figure A.6 and Figure A.7; black trace). This

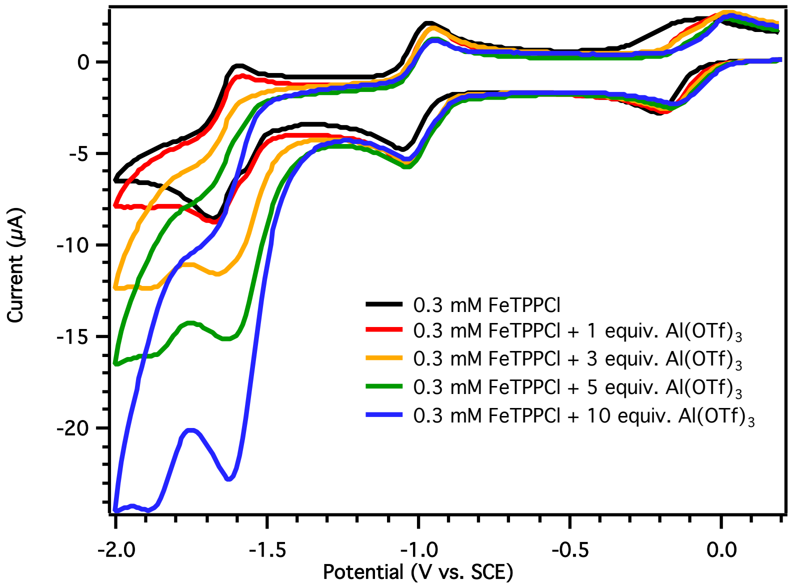

Figure A.6. Cyclic voltammograms of FeTPPCl (0.3 mM) in the presence of Al(OTf)$_3$ in DMF (0.1 M NBu$_4$PF$_6$) under Ar at a glassy carbon electrode at a scan rate of 0.1 V/s.

shoulder peak is attributed to the oxidation of two species in solution resulting from ligand exchange between Cl anion and DMF solvent.

Increasing concentrations of $Al(OTf)_3$ results in a gradual anodic shift of the shoulder oxidative peak at the Fe(III/II) couple resulting in a single oxidation event for at the Fe(III/II) couple. This shift suggests an interaction between the $Al(OTf)_3$ and the reduced FeCl porphyrin complex resulting in the formation of an uncharacterized anion exchange product, presumably Fe porphyrin with triflate anion.[15] Addition of $Al(OTf)_3$ also results in changes at the Fe(I/0) couple for both FeTPPCl and FeF20TPPCl complexes (Figure A.6 and Figure 7; red to blue traces).

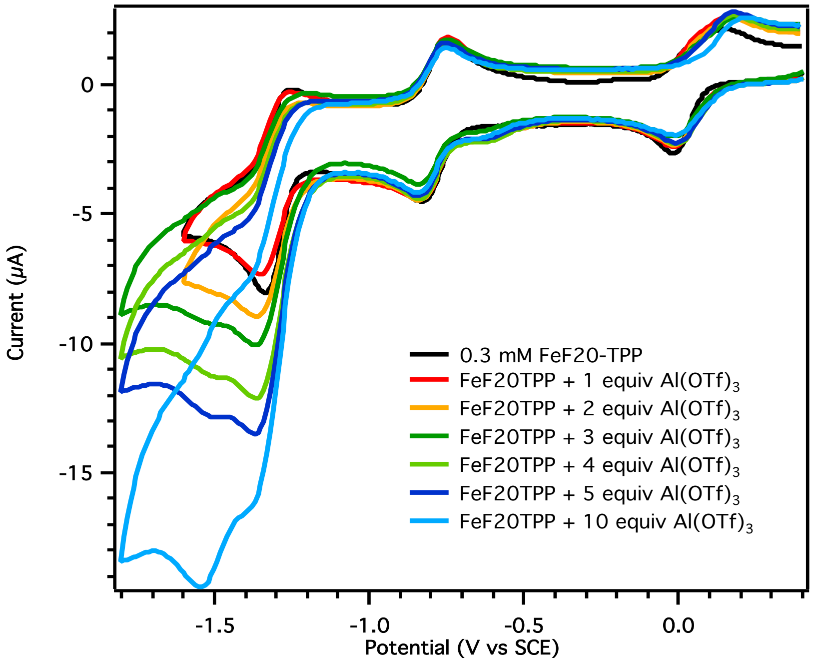

Figure A.7. Cyclic voltammograms of FeF20TPPCl (0.3 mM) in the presence of $Al(OTf)_3$ in DMF (0.1 M NBu_4PF_6) under Ar at a glassy carbon electrode at a scan rate of 0.1 V/s.

Most notably is an observed loss of reversibility and increase in current with increasing $Al(OTf)_3$ under Ar. The loss of reversibility at the Fe(I/0) couple is suspected to result from a chemical step following electron transfer involving the reduced Fe(0) species and $Al(OTf)_3$ to generate a new unidentified species denoted as Fe’. The formation of a new species is also supported by the appearance of a new redox feature ~170 mV negative of the Fe(0/I) couple. Scan rate dependence studies of the new redox feature indicate that the new species is diffusion limited and not absorbed on the surface (Figure A.8).

A current increase is observed with increasing Al(OTf)3 concentration. Products of this catalytic reaction were not investigated. It is hypothesized that the increase in current could indicate catalytic H_2 production from residual H_2O in the DMF solvent.

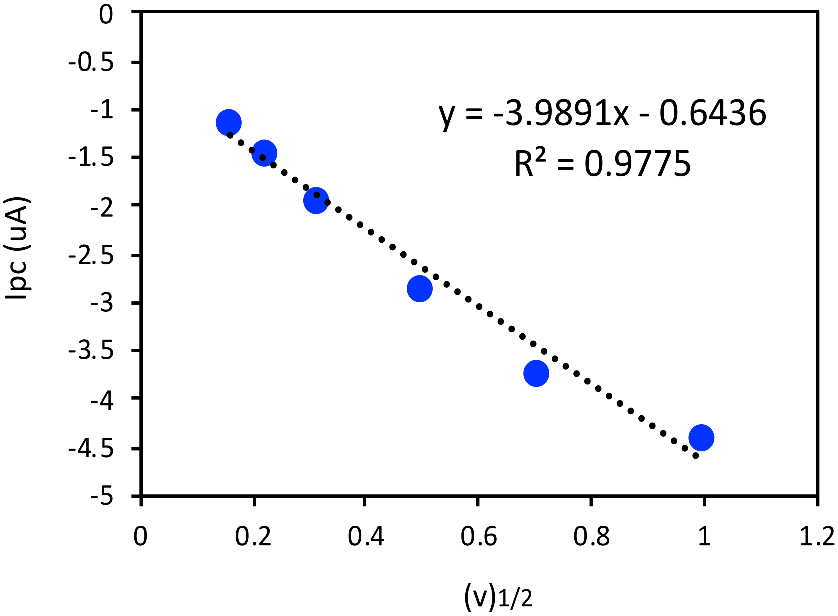

Figure A.8. Plot of peak cathodic current (I_{pc}) vs the square root of the scan rate for FeF20TPPCl unidentified Fe’ reduction in DMF.

A.3.5. FeTPPCl with Al(OTf)3 under CO_2 with H_2O in DMF

An increase in current is observed for FeTPPCl in the presence of both Al(OTf)3 and CO_2 at -1.6 V vs SCE (Figure A.9; red trace). The increased current occurs at a reduction potential that coincides with the Fe(I/0) couple. The peak shape indicates a substrate diffusion limited process for the scan rates surveyed. The new Fe' species that results upon forming the reduced Fe center in the presence of Al(+3) cations is not observed under CO_2. The loss of the Fe' redox feature suggests that, if Al(+3) cation binds to form a new Fe prophyrin species, binding of CO_2 is faster than Al(+3) cations in solution. Upon addition of H_2O, a larger current is passed at the Fe(I/0) couple indicating catalysis (Figure A.9; green trace).

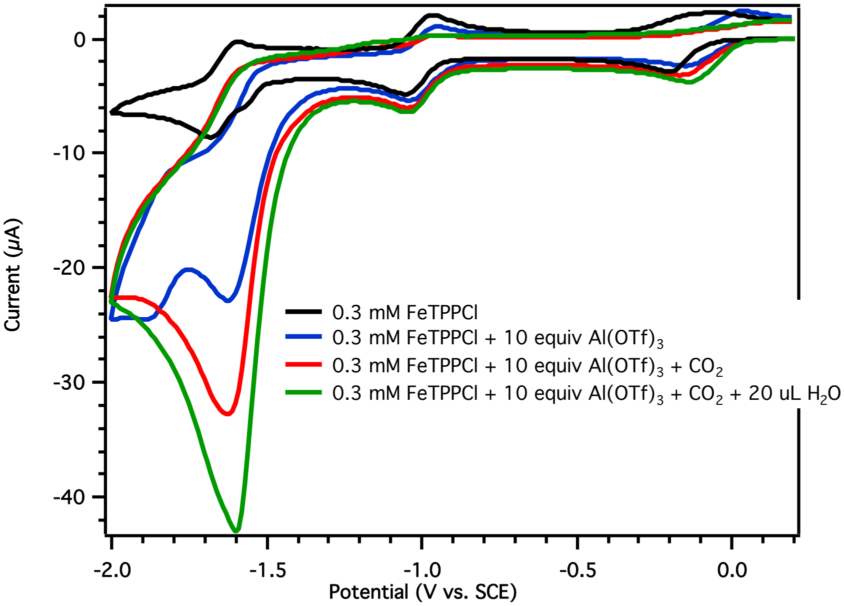

Figure A.9. Cyclic voltammograms of FeTPPCl (0.3 mM) in the presence of (a) $Al(OTf)_3$ in DMF (0.1 M NBu_4PF_6) under Ar (b) under CO_2 (c) with water at a glassy carbon electrode at a scan rate of 0.1 V/s.

A.3.6. FeF20TPPCl with $Al(OTf)_3$ under CO_2 with H_2O or phenol in DMF

Upon addition of CO_2 to a solution of FeF20TPPCl and $Al(OTf)_3$, an increased in current at -1.4 V vs. SCE is observed with a plateau shape (Figure A.10;red trace). Similar to the results reported for FeTPPCl, the presence of CO_2 in solution results in the loss of the previously observed redox feature Fe’ (formed at the Fe(I/0) couple in the presence of $Al(OTf)_3$). This suggests that reactivity at the reduced Fe porphyrin species with CO_2 is faster than with $Al(OTf)_3$.

When water is added to a solution containing FeF20TPPCl and $Al(OTf)_3$ under CO_2, a large catalytic current with a positive shift in the onset potential is observed (Figure A.10; blue trace).

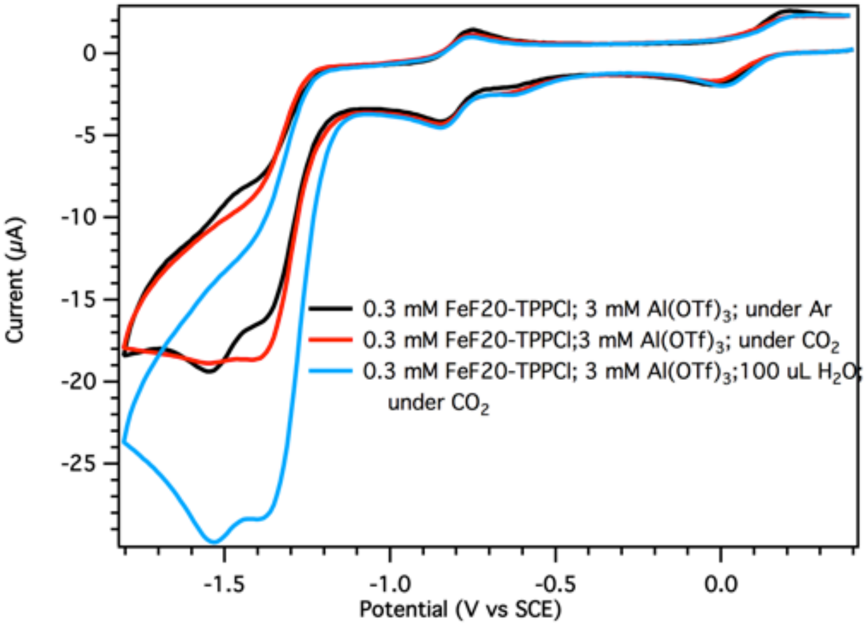

Figure A.10. Cyclic voltammograms of FeF20TPPCl (0.3 mM) in the presence of (a) $Al(OTf)_3$ in DMF (0.1 M NBu_4PF_6) under Ar (b) under CO_2 (c) with water at a glassy carbon electrode at a scan rate of 0.1 V/s.

Interestingly, in the presence of water as a proton source the previously observed redox feature attributed to unidentified Fe’species is observed. Products of this catalytic current have not been independently investigated by controlled potential electrolysis.

A large catalytic current at the Fe(I/0) couple for FeF20TPPCl in the presence of phenol and $Al(OTf)_3$ is observed (Figure A.11; green trace). Although products of this catalytic current have not been independently investigated, it is hypothesized that the catalytic reaction is due to H_2 production. Also, the previously observed redox feature attributed to an unidentified Fe’ species is observed.

When a solution of FeF20TPPCl, phenol and $Al(OTf)_3$ is saturated with CO_2 the cyclic voltammetry response becomes more complicated. A new pre-wave at -0.65 V vs SCE is observed before the Fe(II/I) couple. This could indicate the formation of a new species in solution associated with a single reduced Fe porphyrin species and CO_2. The increased current is observed at the Fe(II/I) and Fe(I/0) couples and is attributed to catalysis.

A.3.7. $Al(OTf)_3$ under CO_2 with H_2O in DMF

The reactivity of the $Al(OTf)_3$ with CO_2 and water was investigated (Figure A.12). $Al(OTf)_3$ is regarded to be a redox inactive species. Cyclic voltammograms with increasing $Al(OTf)_3$ concentrations does not show distinct redox features, only a broad feature that increases in current under 1 atm of CO_2 and water at -1.70 V vs SCE.

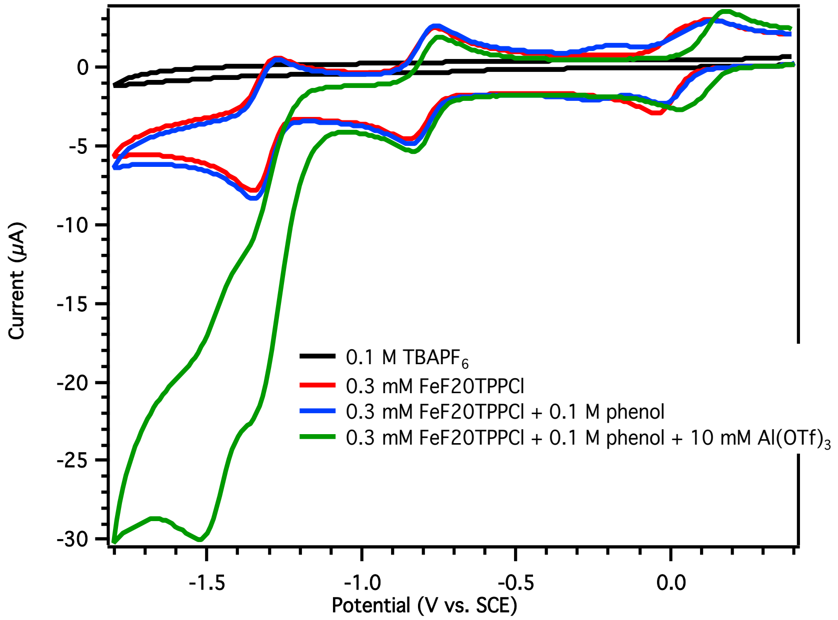

Figure A.11. Cyclic voltammograms of FeTPPCl (0.3 mM) in the presence of (a) Al(OTf)$_3$ in DMF (0.1 M NBu$_4$PF$_6$) under Ar (b) under CO$_2$ (c) with phenol at a glassy carbon electrode at a scan rate of 0.1 V/s.

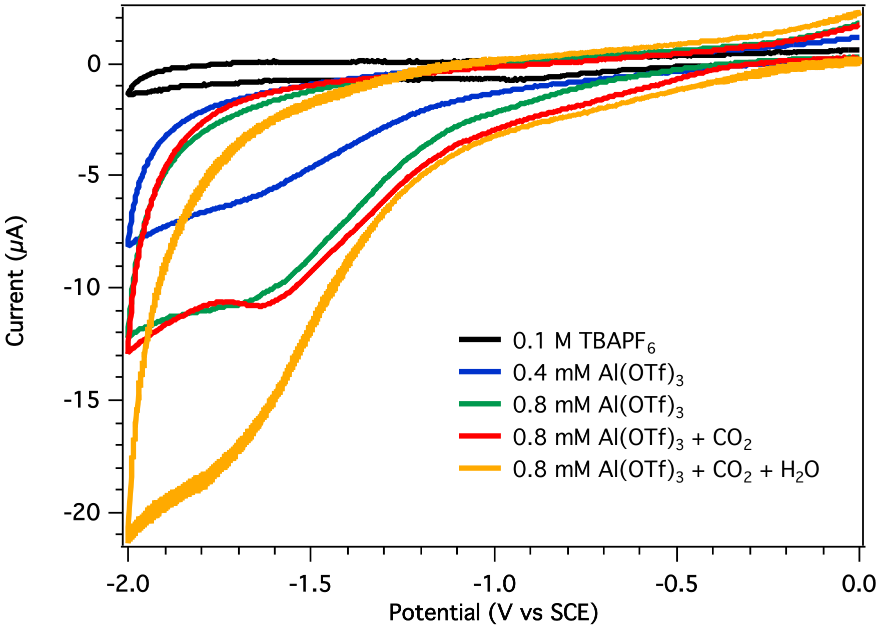

Figure A.12. Cyclic voltammograms of a) Al(OTf)$_3$ in DMF (0.1 M NBu$_4$PF$_6$) under Ar or (b) under CO$_2$ (c) with water at a glassy carbon electrode at a scan rate of 0.1 V/s.

A.4. Conclusions

The results suggest that highly charged Lewis acid cations like $Al(OTf)_3$ can interact with reduced Fe species in solution. However, the resulting product is currently unknown. Although the products were not investigated, it seems that H_2 production may be a competing pathway in the presence of $Al(OTf)_3$ and a proton source. Future controlled potential electrolysis experiments are necessary to investigate product distribution in the headspace and in solution.

A.5. Experimental Details

Materials

FeTPPCl and FeF20TPPCl were purchased from Sigma Aldrich and used without further purification. Anhydrous *N,N*-Dimethylformamide (DMF) from a fresh sure seal bottle was used without additional drying methods for electrochemistry experiments.

Electrochemistry

Cyclic voltammetry experiments were conducted in glass 4-port electrochemical cell under Argon gas. Experiments were conducted using 0.1 M TBAPF6 and dry DMF solvent. Solvent was sparged with Ar before each scan and kept under a blanket of Ar during scans. A glassy carbon disk working electrode, a Pt wire counter, and SCE reference electrode were used. The glassy carbon disk electrode polished with diamond paste and rinsed between each scan. Uncompenstaed resistance measurements were taken before each scan and applied.

CO_2 Addition

Argon and CO_2 gases are passed through a $CaSO_4$ drying column before sparging into solution. Electrolyte and Lewis acid salts are dried under vacuum for at least 1 hour to remove moisture from sample before preparing electrochemical solutions. Working electrode is polished in between scans, rinsed with DI water and acetone, then dried before being placed back into electrochemical solutions.

A.6. References

1. Bhugun, I.; Lexa, D.; Savéant, J.-M., Catalysis of the Electrochemical Reduction of Carbon Dioxide by Iron(0) Porphyrins: Synergystic Effect of Weak Brönsted Acids. *J. Am. Chem. Soc.* **1996,** *118* (7), 1769-1776.

2. Bhugun, I.; Lexa, D.; Savéant, J.-M., Catalysis of the Electrochemical Reduction of Carbon Dioxide by Iron(0) Porphyrins. Synergistic Effect of Lewis Acid Cations. *J. Phys. Chem.* **1996,** *100* (51), 19981-19985.

3. Bhugun, I.; Lexa, D.; Saveant, J.-M., Ultraefficient selective homogeneous catalysis of the electrochemical reduction of carbon dioxide by an iron(0) porphyrin associated with a weak Broensted acid cocatalyst. *J. Am. Chem. Soc.* **1994,** *116* (11), 5015-5016.

4. Francke, R.; Schille, B.; Roemelt, M., Homogeneously Catalyzed Electroreduction of Carbon Dioxide—Methods, Mechanisms, and Catalysts. *Chem. Rev.* **2018,** *118* (9), 4631-4701.

5. Costentin, C.; Robert, M.; Savéant, J.-M.; Tard, C., Breaking Bonds with Electrons and Protons. Models and Examples. *Acc. Chem. Res.* **2014,** *47* (1), 271-280.

6. Azcarate, I.; Costentin, C.; Robert, M.; Savéant, J.-M., Through-Space Charge Interaction Substituent Effects in Molecular Catalysis Leading to the Design of the Most Efficient Catalyst of CO2-to-CO Electrochemical Conversion. *J. Am. Chem. Soc.* **2016,** *138* (51), 16639-16644.

7. Hammouche, M.; Lexa, D.; Momenteau, M.; Saveant, J. M., Chemical catalysis of electrochemical reactions. Homogeneous catalysis of the electrochemical reduction of carbon dioxide by iron("0") porphyrins. Role of the addition of magnesium cations. *J. Am. Chem. Soc.* **1991,** *113* (22), 8455-8466.

8. Bernskoetter, W. H.; Hazari, N., Reversible Hydrogenation of Carbon Dioxide to Formic Acid and Methanol: Lewis Acid Enhancement of Base Metal Catalysts. *Acc Chem Res* **2017,** *50* (4), 1049-1058.

9. Buss, J. A.; VanderVelde, D. G.; Agapie, T., Lewis Acid Enhancement of Proton Induced CO_2 Cleavage: Bond Weakening and Ligand Residence Time Effects. *J. Am. Chem. Soc.* **2018,** *140* (32), 10121-10125.

10. Bielinski, E. A.; Lagaditis, P. O.; Zhang, Y.; Mercado, B. Q.; W√ºrtele, C.; Bernskoetter, W. H.; Hazari, N.; Schneider, S., Lewis Acid-Assisted Formic Acid Dehydrogenation Using a Pincer-Supported Iron Catalyst. *J. Am. Chem. Soc.* **2014,** *136* (29), 10234-10237.

11. Zhang, Y.; MacIntosh, A. D.; Wong, J. L.; Bielinski, E. A.; Williard, P. G.; Mercado, B. Q.; Hazari, N.; Bernskoetter, W. H., Iron catalyzed CO_2 hydrogenation to formate enhanced by Lewis acid co-catalysts. *Chem. Sci.* **2015,** *6* (7), 4291-4299.

12. Gambarotta, S.; Arena, F.; Floriani, C.; Zanazzi, P. F., Carbon dioxide fixation: bifunctional complexes containing acidic and basic sites working as reversible carriers. *J. Am. Chem. Soc.* **1982,** *104* (19), 5082-5092.

13. Park, Y. J.; Ziller, J. W.; Borovik, A. S., The Effects of Redox-Inactive Metal Ions on the Activation of Dioxygen: Isolation and Characterization of a Heterobimetallic Complex Containing a MnIII–(μ-OH)–CaII Core. *J. Am. Chem. Soc.* **2011,** *133* (24), 9258-9261.

14. Park, Y. J.; Cook, S. A.; Sickerman, N. S.; Sano, Y.; Ziller, J. W.; Borovik, A. S., Heterobimetallic Complexes with M-(OH)-M Cores (M = Fe, Mn, Ga; M = Ca, Sr, and Ba): Structural, Kinetic, and Redox Properties. *Chem Sci* **2013,** *4* (2), 717-726.

15. Gueutin, C.; Lexa, D.; Momenteau, M.; Saveant, J. M.; Xu, F., Molecular environment effects in redox and coordination chemistry. Protection against solvation, local solvation, and

steric hindrance to ligation in the electrochemistry of basket-handle iron porphyrins. *Inorg. Chem.* **1986,** *25* (23), 4294-4307.

16. Savéant, J.-M., Molecular Catalysis of Electrochemical Reactions. Mechanistic Aspects. *Chem. Rev.* **2008,** *108* (7), 2348-2378.